SYNTHESIS AND CHARACTERIZATION OF ENGINEERED PARTICULATES WITH CONTROLLED SURFACE ARCHITECTURE

By

JAMES MICHAEL FITZ GERALD

A DISSERTATION PRESENTED TO THE GRADUATE SCHOOL
OF THE UNIVERSITY OF FLORIDA IN PARTIAL FULFILLMENT
OF THE REQUIREMENTS FOR THE DEGREE OF
DOCTOR OF PHILOSOPHY

UNIVERSITY OF FLORIDA

1998

Copyright 1998
by
JAMES MICHAEL FITZ-GERALD

I would like to dedicate this work to the memory of my brother, Bobby

ACKNOWLEDGMENTS

I would like to acknowledge the many individuals that have made this adventure possible. I would first like to thank my advisor, Dr. Rajiv Singh, for giving me support, encouragement and direction over the last 4 years of my graduate education. Dr. Singh's mentoring, both as a friend and a professional during this time period has impacted my life significantly, at and away from the University setting. I would like to thank Dr. Brij Moudgil not only for serving me a committee member but also for his guidance and support through the Engineering Research Center for Particle Science and Technology. I would like to thank Dr. Joseph Simmons, Dr. Robert DeHoff and Dr. David Tanner for serving as my dissertation committee members as well as for their timely guidance through numerous discussions.

I would also like to thank the several people who have donated their personal time and equipment to assist me with this research. I would like to thank the Physics Department's Engineering Analysis Team (EAT) run by Robert Fowler and his support staff for their assistance and "helpful comments" during the continuous fabrication of my research equipment. I would also like to thank the staff at MAIC for their support and assistance in sample characterization. Special thanks go

to Brent Gila and Wishy for TEM sample preparation and analysis as well as for teaching me the "continuous roll of stored images" theory.

I would like to thank some good friends and their families: Rajiv Bandais, Talal Chohan, Mark Figgy, Don Gilbert, Dong Gu Lee, Mike Meuse, Peter Miller, Dean Paxton, Philip Rack, Pius Talton, Paul Veradt, and John Viateila for making my graduate experience at the University rewarding, challenging and humorous at times.

I would also like to thank the following for their contributions of friendship and support: Molli, Spanks, Bubba, Troy, Steven Ivory, Figgy, Laurie Alosa, Kelly Harden, Alan Ossi, Ann, Sophie, Mary, Rhonda, Erik, Byron, Sharon, Yakov Rabinovich, Kevin, Rob, Uday, Kyu, Marc, Srini, Anew and many others which I have not listed.

I would like to thank the Department of Materials Science faculty, staff and administration for their support. Thanks to Jackie Huisey and Debbie Malis for their administrative support and sane discussions.

Special thanks to my wonderful wife Dana for her constant support and encouragement during the last few years. I would like to thank my mother and father and my sister Mary for their love and support during my extended years of education. I would also like to lovingly thank the family of John and Diane Marcinka as well for their support of Dana and I over the last four years.

TABLE OF CONTENTS

	page
ACKNOWLEDGMENTS	iv
LIST OF TABLES	viii
ABSTRACT	ix
CHAPTERS	
1 LITERATURE REVIEW	1
Introduction	1
Background	2
Excimer Laser Basics	6
Beam-Solid Interactions	10
Atomistic Analysis	22
Effect of Background-Gas Synergy	32
Nano Particle Formation	33
2 EXPERIMENTAL PROCEDURES	36
Experimental Setup	36
Experimental Descriptions	39
Samples	41
Experimental Characterization Techniques	48
Optical Spectroscopy	48
Wire Probe Measurements	48
Photodiode Measurements	49
Fast CCD Camera Measurements	49
Laser Ablation Depth Measurements	52
Auger Electron Spectroscopy	54
Micro Probe Analysis	54
X-ray Photo Electron Spectroscopy	55
Scanning Electron Microscopy	55
Transmission Electron Microscopy	56
Scanning Transmission Electron Microscopy	57

3. EXPERIMENTAL RESULTS ... 60

Silver Target Ablation Measurements ... 60
Charge Coupled Device Camera (CCD) Measurements ... 65
Optical Spectroscopy ... 73
Wire Probe Measurements ... 78
Powder Synthesized Samples ... 80
Scanning Electron Microscopy ... 80
X-ray Photo Electron Spectroscopy ... 88
Deposition on Mesh TEM Grids ... 90
Summary of Experimental Results ... 97

4 DISCUSSION ... 98

Introduction ... 98
Optical Spectra ... 98
Plume Expansion Characteristics ... 109
Nano Particle Formation ... 122
Structural Analysis ... 136
Structural Imaging ... 141
Crystalline Structure ... 148
Nano Particle Adhesion ... 154

5 CONCLUSIONS ... 162

APPENDICES

A NANO PARTICLE CALCULATIONS ... 166

B X-RAY PHOTO ELECTRON SPECTROSCOPY ... 176

C GAS PHASE COLLISION CALCULATIONS ... 179

D LASER INTERACTIONS WITH MATERIALS CALCULATIONS ... 214

LIST OF REFERENCES ... 219

BIOGRAPHICAL SKETCH ... 223

LIST OF TABLES

Table		Page
2.1	Deposition on Particulate Materials	44
2.2	Deposition on Mesh Grids	45
3.1	Results From Laser Ablation Calculations	63
3.2	Summary of Calculations	64
3.3	References and Observed Atomic Line Emissions	77

Abstract of Dissertation Presented to the Graduate School of the University of Florida in Partial Fulfillment of the Requirements for the Degree of Doctor of Philosophy

SYNTHESIS AND CHARACTERIZATION OF ENGINEERED PARTICULATES WITH CONTROLLED SURFACE ARCHITECTURE

By

James Michael Fitz-Gerald

August, 1998

Chairperson: Rajiv K. Singh
Major Department: Materials Science and Engineering

A state - of - the - art technique using pulsed excimer laser deposition to synthesize nano metric coatings on particulate materials has been investigated. The novelty of the technique that separates it from other dry coating methods arises from the fact that the nano particles are synthesized and deposited onto the core particulate material simultaneously, reducing deleterious agglomeration problems associated with dry powder coating systems. By attaching atomic to nano-sized particles either in discrete or continuous form onto the surfaces of the core particles, that is, *nano-functionalization of the particulate surface*, materials and products with significantly enhanced properties can be obtained.

In-situ analysis by high speed, time gated CCD camera

imaging, time gated wire probe velocity measurements, and optical spectroscopy were performed in conjunction with analytical techniques. Analytical techniques utilized were scanning electron microscopy (SEM), wavelength dispersive x ray mapping (WDX), Auger electron spectroscopy (AES), transmission electron microscopy (TEM), scanning transmission electron microscopy with z contrast (STEMZ), and x-ray photoelectron spectroscopy (XPS), to examine the structural, chemical, and morphological characteristics of the nanometric coatings.

Qualitative surface uniformity measurements by WDX and XPS mapping techniques showed a high degree of coating uniformity on the core particulate. Structural TEM and STEMZ imaging showed both continuous and discrete polycrystalline, multiply twinned nano particle coatings ranging from 5-40 nm in thickness. Further AES depth profiling verified the coating thicknesses to be ≈25 nm.

CHAPTER 1
LITERATURE REVIEW

Introduction

Wide ranges of advanced technologies based on existing and emerging products employ micron to submicron sized (0.1-10 microns) particulate precursors for synthesis and fabrication. Examples of these technologies are high temperature metal-ceramic composites used in aircrafts, cutting tools, lithium-ion rechargeable batteries, superconductors, field emission flat-panel displays. Although there has been significant emphasis given to control of the particle characteristics (shape, size, surface chemistry, adsorption, etc.), almost no attention has been paid to designing the desirable properties at the particulate level, which can ultimately lead to enhanced properties of the product. By attaching atomic to nano-sized inorganic, multi-elemental particles either in discrete or continuous form onto the surface of the core particles, that is, *nano-functionalization of the particulate surface*, materials and products with significantly enhanced properties can be obtained.

Background

The field of particle science has undergone significant transformations over the last five years in particle processing and coatings. Some new challenges that we are facing are in nano-structures, which is regarded to be the key to the next generation of high performance materials and coatings [Kea95]. A few of the areas of interest for nano structured materials are processing control (sintering), catalytic properties (reactivity) and light emitting materials (phosphore). Currently one of the biggest challenges is the creation of nano-coated materials with complex stoichiometry and controlled surface architecture. Nano coated materials are defined here to be materials with external surface coatings that are about 1-50 nm in thickness. Research concerning nano-structured materials, both in bulk materials and coatings, have been investigated [Kea95] [Ler91] [Wan95]. In work being performed by Kear et al., significant investigation has been done in the area of nano-particle synthesis and nano-structured coatings.

Three methods are generally used in this work to synthesize nano particles [Kea95]. The aqueous solution reaction (ASR) method has been developed to synthesize nano-steel powders [Kea95]. The synthesis involves three steps: (1) preparation of aqueous solution of mixed metal (Fe, Cr, Mo and V) chlorides using deionized and de-oxygenated water, (2)

reductive decompositions of the starting solution with sodium trialkyal-borohydride to obtain a colloidal solution of the metallic constituents, and (3) after filtering, washing and drying, gas phase carburization under controlled carbon and oxygen activity conditions to form the desired nano-dispersion of a carbide phase in a metallic matrix

Inert gas condensation (IGC) is another process that is in use today for synthesizing nano-structured *powders* [Kea95] In IGC processing, an evaporative source is used to generate the powder particles These particles are then convectively transported to and collected on a cold substrate The nano particles develop in a thermalizing zone just above the evaporative source, due to the interactions between the hot vapor species and the colder inert gas atoms.

Another process that is currently under development for creating nano-powders is the chemical vapor condensation (CVC) process In this new process the original evaporative heating source is replaced by a hot-wall tubular reactor, which decomposes the precursor/carrier gas to form a continuous stream of nano-particles exiting from the reactor tube. These particles exhibited average particle sizes of 6-10 nm as determined from TEM observations [Kea95]

The same powders produced by the above techniques have been applied in the area of thermal spraying of nano-structured coatings Thermal spraying is a widely used industrial process for applying protective coatings to

material surfaces. An attractive feature of the process is its ability to produce coatings ranging in thickness from 25 microns to several millimeters. Historically, thermal spray deposition of metal, ceramic and composite coatings was developed for applications in aircraft gas turbine engines. In thermal spraying, powders are introduced into a combustion flame or plasma arc spray gun, where they are rapidly accelerated by the high velocity gas stream exiting from the gun nozzle. During the short residence time in the flame or plasma, the particles are rapidly heated to form a spray of partially or completely melted droplets. The large impact forces created as these particles arrive at the substrate surface promotes strong particle-substrate adhesion and the formation of a dense coating. However, problems arise from the inability to reproducibly control coating composition, structure and grain morphology. Also, the presence of residual porosity within the coating and the technical difficulties associated with delivering powder at a uniform rate to the thermal spray gun remain.

Research in nano-particle production by laser processing has been done [Mul95] [Koy92] [Ser94] [Yos96]. A focused CO_2 laser operating in continuous output mode is used as a heating source to excite a solid target into an oxide vapor [Mul95]. Oxides produced from the solid target then recondenses in the atmosphere above the sample. Due to the very narrow region at high temperature created by the laser, the nuclei migrate

quickly to the cooler regions of the reaction chamber and the growth is stopped. Newly formed nano particles are then transported by a carrier gas stream caused by a pump at the end of the apparatus. One of the limitations of this particle creation system is the photon absorption coefficient of the CO_2 laser. For many materials such as oxides and metals, the absorption coefficient is low ($<10^3$/cm) leading to undesirable processing characteristics. Low absorption leads to significant bulk heating effects of the target material, and there is little control over stoichiometry from multi-elemental targets. In related work done by Yoshida et al. and Koyama et al., nano-sized silicon and II-VI semiconductor particles have been produced by using a ND:YAG laser to ablate solid wafer targets in a constant pressure environment onto silicon substrates. While these techniques are viable for the production of nano-particles, there currently does not exist a method to both synthesize and coat nano-particles onto core particles. Other difficulties that are currently observed are control over stoichiometry of multi-component coatings, uniformity and thickness. The following two sections some important aspect of beam-solid interaction and current research related to nano-particle formation will be illustrated.

Excimer Laser Basics

Excimer lasers are a family of gas lasers that emit powerful ultraviolet (UV) pulses lasting from a few nanoseconds to hundreds of nanoseconds. The usual active medium is a gas mixture containing a rare gas and a halogen, which combine to form a short-lived rare gas halide molecule. The term excimer originated as a contraction of "excited dimer," a molecule that consists of two identical atoms and exists only in an excited state, such as He_2 or Xe_2. Excimer is now used to describe any diatomic molecule (and sometimes tri-atomic types) in which the atoms are bound in the excited state but not in the ground state. That property makes them good laser candidates because it automatically depopulates the lower level of the laser transition. The most important excimer media are the rare-gas halides: argon fluoride (ArF), krypton fluoride (KrF), xenon fluoride (XeF), and xenon chloride (XeCl), which emit at wavelengths of 193, 248, 308, and 350 nm, respectively. These molecules are formed by passing an electric discharge through a suitable gas mixture to excite atomic transitions. The gas systems above operate so similarly that many can be made to lase in the same device. Molecular fluorine (F_2) can lase at 157 nm in devices and thus is called and excimer laser, although the molecule is not an excimer even in a lesser contextual definition (F_2 also emits about 3% of its energy on a secondary red line).

In a discharge driven excimer laser, discharge pulses are directed perpendicular to the laser-beam axis through the gas in a sealed tube. In an electron-beam pumped laser, the electrons are more likely to be directed along the beam axis. Normally, a reservoir outside the excitation region holds extra laser gas, and the gas may be circulated through the laser for operation at high powers or high repetition rates as shown in Figure 1.1 (a). The laser gas deteriorates during use, and the halogens are so reactive that the gas even degrades when the laser is not being used. New gas must flow into the active zone between shots. Halogen may be added periodically to extend gas lifetimes, some lasers have computer controls that automatically sense when to add the gas. Laser cavities are designed to be sealed and repeatedly refilled, often with different laser gas mixtures. Each fill lasts thousands to millions of shots, depending on gas type and operating conditions. Longer gas lifetimes are possible with gas reprocessing to remove impurities. After the gas is spent, the cavity must be emptied and refilled, with purging and pacification required when changing between different gas mixtures. The laser cavity, optics, and electrodes must be designed to resist corrosion by halogens in the laser gas. Passive components typically are coated with Teflon, and electrodes are made of halogen-resistant materials such as solid nickel or brass.

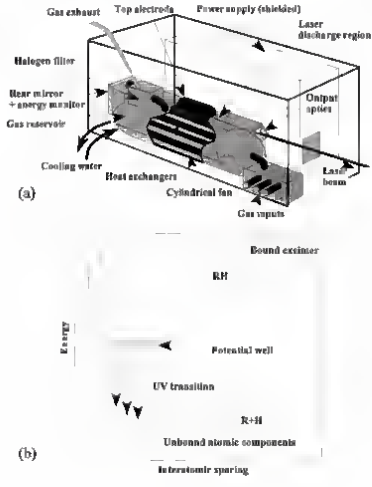

Figure 1 1 Schematic diagram of (a) a pulsed excimer laser and its components, and (b) illustrating the excited state excimer transitions

Total gas pressures in rare-gas halide excimer lasers are usually less than five atmospheres, with 90% to 99% buffer gases such as helium or neon to medists energy transfer The rare gas that combines to form the excimer is present in lower concentrations, typicaiiy 1% 9% Haiogen donor levels are usuaiiy 0 1%-0 2%; the donor may be a diatomic halogen such as molecuiar fiuorine or a haiogen containing molecuie such as hydrogen chloride

Energy is deposited in the laser gas by an electric discharge, microwave excitation, or electron beam Up to 5% of the energy in an electric discharge can be converted into laser energy, and overali waii-plug efficiency can reach 2 5% Electron pumping can achieve higher pumping efficiency, but the electron beam generators are inefficient, so overall laser system efficiency is lower Microwave excitation is used in small waveguide lasers to avoid arc formation and other discharge in homogeneities, allowing uniform excitation of a small voiume of high-pressure laser gas Preiiminary preionization pulses are often used to produce free halogen atoms The main excitation pulse stimulates rare-gas atoms to react with the halogen, forming excited diatomic molecules, their excited state is often shown by adding asterisk to the chemical formula KrF The two atoms attract when molecules are electricaliy excited, but they repel or are weakiy bound in the ground state as shown in Figure i i (b) This behavior causes the molecuie to break up when it drops to the ground

state, automatically depopulating the lower laser level and helping to insure a population inversion as long as excited molecules are present
This process contributes to the high gain on excimer transitions

Beam Solid Interactions

The ever emerging field of lasers and their applications has been felt in a wide variety of technologies that are used today. This analysis is presented in an attempt to explain the physics of laser interactions that are relevant to the area of pulsed laser ablation with respect to particle coatings. The coupling of the laser beam with the surface of the target material will have significant effects on the formation and the microstructure of the subsequently deposited material. The microscopic and macroscopic mechanisms of laser beam-solid surface interaction have been investigated extensively since pulsed, high power, lasers became available in the 1960s [Mai60] [Pat64] [Rot84] [Sas88] [Sin88] [Sch90] [Kas90] [Geo91] Figure 1.2 shows the different regimes of laser interactions and illustrates the importance with respect to mechanisms of atomic behavior

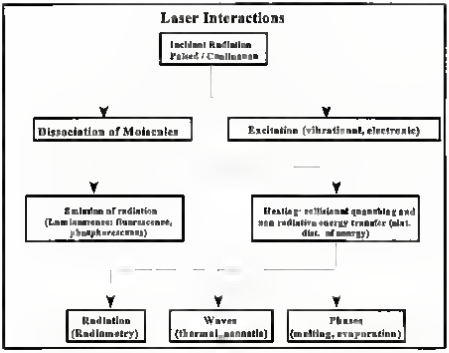

Figure 1 2 Schematic illustrating the different regimes of beam solid interactions with materials.

The results have shown the feasibility of using lasers as a tool for materials processing. This technique recently has marked significant progress in its application to many other fields of basic research and materials technologies. Examples of this are production of micro clusters, growth of thin films, annealing, etching, or chemical modification of surface layers in the fabrication of microelectronic devices [Kas90] [Sin91b] [Zhe92]. Some of the main factors that control the nature of the evaporation process are the optical properties (absorption coefficient, reflectivity), power density of the laser pulse and thermophysical properties of the material including thermal conductivity, heat capacity. Based on the laser target interactions, two separate heating regimes, depending on the thermal diffusion distance and the absorption coefficient of the target, have been identified: (i) the surface heating regime in which the laser energy is deposited near the target surface, and (ii) the volume heating regime in which a volume of the solid material is heated by the laser pulse. In both of these regimes, vaporization of the target can proceed either by planar surface etching or by volume etching in which solid material may be ejected from the target surface. The thermophysical and the optical properties of the target and the laser parameters determine the specific nature of the ablation regime. One of the most relevant subjects to address in the macro view of laser interactions is in the area of heating. How effectively does the laser radiation couple

into the material? The heating effects of pulsed nano-second laser irradiation can be understood by solving the basic one-dimensional heat flow equation with appropriate boundary conditions

The thermal effects of pulsed nano second laser-irradiation of materials is determined by several laser parameters. Some of these parameters are the temporal power densities, I(t), pulse duration, t_p, wavelength, λ, optical properties, reflectivity, R, absorption coefficient, α, and the thermal properties of the material, thermal conductivity, K, latent heat per unit volume, L_v, specific heat per unit volume, C_v, ablation temperature, T_v, etc.) The thermal diffusivity $D=K/C_v$ defines the thermal diffusion length $(2Dt_p)^{1/2}$ which determines the spread of the temperature profile during the laser pulse. The temperature in the target, T(x t), during laser irradiation is controlled by the heat flow equation 1

$$C_v(T)\frac{\partial T(x,t)}{\partial t}=\frac{\partial}{\partial x}\left[K(T)\frac{\partial T(x,t)}{\partial x}\right]+(1-R)I_0(x,t)\alpha e^{-\alpha x} \quad 1$$

with the appropriate boundary conditions that take into account the formation and movement of the solid-liquid (or liquid-vapor) interface [Sim94]. Here x refers to the direction in the plane perpendicular to the target, t refers to the time, and I_0 is the incident laser intensity. The

second term on the right-hand side of the equation is called the heat generation term due to the absorption of the incident laser beam by the target. If the surface of the material is highly absorbing ($\alpha \geq 10^6$ cm^{-1}) to the incident laser beam, the heat generation term can be removed from the above equation and applied to the front surface boundary condition. Depending on the nature of heating and thermophysical properties of the materials, two separate regimes can be distinguished [Sin94]. The two regimes are shown schematically in Figure 1.3:

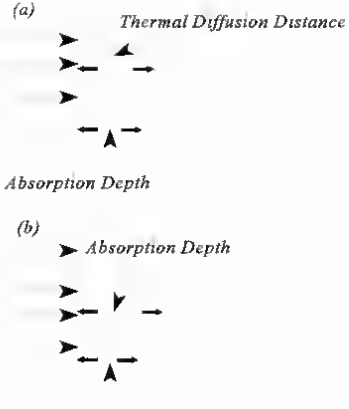

Figure 1 3 Laser heating regimes, (a) surface heating regime in which the optical absorption depth is much smaller than the thermal diffusion distance, $\alpha(2Dt_p)^{1/2} \gg 1$ and (b) the volume heating regime in which the optical absorption depth is much greater than the thermal diffusion distance $\alpha(2Dt_p)^{1/2} \ll 1$ [Sinn88]

In the first case the laser energy is absorbed in the surface layer, and the thermal diffusivity controls the heating and ablation characteristics. During ablation of the target, a planar vaporization interface may initiate from the surface and propagate into the bulk of the target. However, at higher power densities, subsurface heating effects may become important which may lead to explosive removal of material from the target, and thus lead to nonlinear ablation effects [Sin94].

In the volume heating regime, the thermal conductivity plays an insignificant role in controlling the laser target interactions, and the ablation depth is determined mainly by the optical absorption depth given by the inverse of the absorption coefficient. In this regime, internal heating sub-surface effects may predominate leading to removal of particles from the target, and these particles may shield the target from the incoming laser beam.

Within the surface heating and ablation regimes, the laser energy is deposited near the target surface and ablation proceeds with a planar movement of the vaporization interface from the surface of the target [Sin94].

The absorption coefficient is one of the controlling properties of a material that will dictate how the material will absorb at a given wavelength. Metals such as Cu, Ni, and semiconductors such as Si possess high absorption coefficients (10^6 cm^{-1}) for excimer laser beams. Since the optical

properties of all materials are not readily available for elevated temperatures, measurements are usually based on a constant reflectivity value for the vaporizing surface. It has generally been observed that the reflectivities of metals and semiconductors for excimer laser wavelengths are low; however, their values increase upon melting [Sin91a].

The maximum absorption depth determined from energy balance considerations is given by equation 2

$$\Delta X_f = \frac{(1-R)(E-E_{th})}{(C_p \Delta T + L_f)} \qquad 2$$

where E_{th} corresponds to the threshold energy required for ablation. This equation shows that the depth of the evaporated material should vary linearly with energy density above the threshold energy density required for material removal. However, experimental results have exhibited a nonlinear dependence of evaporation depth with energy density especially at energy densities much higher than the ablation threshold [Sin94]. This nonlinear dependence of ablation depth with energy density even for targets with high absorption coefficients may result in a change in the ablation characteristics of the target at higher energy densities. The increase in the number of solid particles ejected from the target surface at higher energy densities provides strong

evidence of the breakdown of the planar ablation regime [Sin94] The nonlinear ablation effects at higher energy densities for strongly absorbing targets may be a result of non planar surface ablation In the case of planar surface ablation when the vaporization interface moves rapidly into the target, the surface is constantly being cooled due to the latent heat of vaporization However, the absorption of the laser beam in the target is characterized by a finite absorption depth in the material The sub-surface layers are heated directly by the laser beam where the heat dissipation mechanism is the thermal conduction loss in the target. As the energy density is increased, the sub-surface temperatures may vastly exceed the surface temperature that corresponds to the ablation point of the material Effects of this internal heating may lead to explosive removal of material from the target in form of particles In turn these particles may shield the laser beam from the target, thus leading to nonlinear ablation characteristics Therefore superheating increases with energy density, and thus with increasing energy density stronger sub-surface superheating of the target results which may lead to explosive removal of material in the form of small particles (chunk emission) [Sin94] Furthermore, particle shielding can decrease the ablation depth of the target giving rise to a nonlinear dependence of ablation depth with energy density It should be recognized that the sub-surface superheating is more for small values of

absorption coefficient and thus it may be the predominant mechanism for material removal from the target in the volume heating and ablation regime. It should also be understood that if the thermal conductivity of the target is poor, the detailed heat flow equation need not be solved because the nature of the deposition of the laser energy on the target controls the ablation process. The power density of the laser at any point inside the target at a distance, x, from the surface can be expressed by the exponential relationship given by equation 3.

$$I(x,t) = (1-R)I_o e^{-\alpha x} \qquad 3$$

where I_o is the power density of the laser beam at the surface. Since the thermal conduction effects in this regime are negligible, any point in the material will start to evaporate once it has reached its vaporization temperature. If planar surface ablation takes place, the surface recedes inside the target and thus the position of the surface is changing with time. Thus, the total energy deposited at any point inside the target is given by integrating the above equation and taking into account the movement of the vaporization interface during the process.

The total energy deposited at any point x in the material is given by equation 4

$$E_{tot}(x) = (1-R)\, I_o \int_0^{tp} e^{-\alpha(x - St)}\, dt \qquad 4$$

where S is the velocity of the vaporizing interface and tp is the laser pulse duration. This velocity can be approximated as $\Delta X_o/tp$. The integration of the above equation gives

$$E_{tot} = (1-R) E \alpha \exp\left[-\alpha x \left[1 - \frac{1}{\alpha x} \ln\left[\frac{e^{\alpha \Delta x} - 1}{\alpha \Delta x}\right]\right]\right] \qquad 5$$

This equation shows that the deposition of laser energy at any point x in the target is dependent on the value of the x_o α and the vaporization velocity, S. When the total energy deposited inside the target is equal to the threshold value for ablation, E_{th}, the distance x represents the evaporated thickness, Δx. Since heat losses due to conduction effects are negligible, the threshold energy for ablation is given by the energy required to increase the temperature of the target material α^{-1} thick to its ablation temperature, including the latent heat of melting and ablation. Thus, $E_{th} = A/\alpha$, where A is the total heat content per unit volume of the vaporizing material. Substituting this value into the equation, the

evaporated thickness during planar vaporization in the volume heating regime is given by equation 6

$$\Delta x \left[1 - \frac{1}{\alpha \Delta x} \ln \left[\frac{e^{\alpha \Delta x} - 1}{\alpha x} \right] \right] - \frac{1}{\alpha} \ln \left[\frac{E}{E_{sb}} \right] \qquad 6$$

This equation shows that for planar surface ablation in the volume heating regime, the evaporation thickness should exhibit and approximate linear dependence with energy density. However, experimentally the ablation thickness exhibits a sub-linear dependence with energy density [Poa82]. As noted above, planar surface ablation can very easily breakdown in the volume heating regime. In this regime, the absorption coefficients of the target for the incident laser beam are small which will lead to strong sub-surface heating effects during ablation. The sub - surface superheating effects lead to volume ablation of the target in the form of solid particles that shield the target from the incident laser beam. This volume ablation starts in the early stages of laser irradiation itself, and may be the predominant factor controlling the ablation characteristics in the volume heating regime.

Atomistic Analysis

Despite the vast varieties of applications of lasers in beam-solid processing, our physical understanding of its microscopic process is limited to a narrow range of irradiation conditions and target materials. The process for desorption of particles from the irradiated surface may be classified into three consecutive steps of transformation: (1) excitation of a solid target by laser beam; (2) desorption of particles from the target surface (transition from condensed matter to vapor); and (3) expansion of vapors into the vacuum. The dominant process for step (1) is the electron excitation in metals and insulators having energy gaps smaller than the photon energy of the laser beam. Energy absorbed in the electronic system is transferred to the lattice in a time typically less than 1×10^{-12} second, during which the thermal equilibrium is established in the solid [Kas90]. Then, the surface atoms evaporate into a vacuum as a thermal process at the temperature of the surface heated by the laser irradiation. This so-called thermal model of laser desorption, which may be applied to the case of low power laser excitations where the irradiated surface does not change its structure and composition significantly before atoms are ejected from their lattice sites. Although it has been investigated [Oka93] the ablation process is atomic vacancy initiated.

According to Okano et al., the vacancies on the surfaces

can be the nuclei of the evolution of vacancy clusters, by emitting the nearest neighbor atoms, which are bonded more weakly compared with those at perfect lattice sites. Once the vacancies on the top layer of surfaces become the source of vacancy clusters, those in the second layer start to be revealed on the surface, and consequently the evolution of vacancy clusters in the second layer starts. Thus, the mechanism of vacancy initiated ablation can explain both the lateral and vertical development of laser ablation. It has been assumed by Okano et al. that the emission of weakly bonded atoms (WBAs) is induced by a multiple cascade process and that the yield fluence near the ablation threshold can be much stronger than the power function required for breaking the bonds of WBAs.

For higher levels of excitation, a high density of atoms may desorb from the irradiated surface creating or adding to the plasma plume. This plasma can be formed in the early part of a laser pulse and continue to absorb the latter part of the same pulse through the inverse bremsstrahlung process while it expands into the vacuum in step 3. This process of excitation has been investigated extensively in relation to the inertial confinement of laser-produced plasma in fusion studies [Sin94] [Bre91]. The inverse bremsstrahlung process causes desorbed species to be excited to the state of high kinetic energy with considerable degree of ionization, to agree with many experimental observations at very high levels of laser fluence

[Joh89] There must be a lower limit in laser intensity and pulse duration above which the inverse bremsstrahlung process becomes significant. Simple estimates by Archbold et al., show that for a 100 nano second pulse and atoms with an ionization energy of 8eV, the initial temperature of plasma before expansion must be above 5000°C in order for the plasma to absorb a significant amount of energy during its expansion. This minimum value of temperature increases with decreasing pulse width and increasing ionization energy of the target atom. This estimate indicates that there may be a range of laser fluence that is too high to apply the model of thermal evaporation processes. This range may also be too low to apply that of the inverse bremsstrahlung process since boiling points of most of the elements and compounds are below 5000°C. It is questionable whether the thermal model can be applied to cases when the surface temperature exceeds the boiling point of the target material. There are many experimental observations in this range of laser fluence where desorbed atoms exhibit those values of kinetic energy and an ion density much higher than the corresponding quantities predicted by the thermal model [Sin94]. One may note in the above discussion that neither of the two models of laser desorption takes explicit account of step (2), during which atoms are actually ejected out from the surface. This is a region where an explanation from Okano et al. may be relevant at such an intermediate state. The dominant step to absorb

laser energy is in step (1) for the lower excitation region, and it is in step (3) for the higher excitation region. In such cases, the contribution from a step (2) may be neglected to a good approximation in calculating the kinetic energy and degree of ionization of desorbed particles. This may be the reason that simple theoretical models agree well with experiments in these two ranges of excitation although these models do not quantify the most fundamental part of the desorption process (step 2).

In the intermediate region of excitation, the final state of desorbed atoms may depend critically on the transient process of step (2), during which a significant part of the laser energy is absorbed. It is necessary, therefore, to identify the process of transformation of surface atoms from their condensed phase into vapor. Specific experimentation performed by Kasuya and Nishina describe a system that resolves the desorption process in time, space, and wavelength in a one shot measurement. The results suggest that the surface atoms leave the target in various sizes of clusters that subsequently decompose into atoms and their ions in a time scale longer than 10 nano seconds. Therefore, they continue to absorb the latter part of a laser pulse. This absorption process can account for the high ion yield and translational energies observed by many previous investigators [Poa82] [Arc64] [Fur81]. It should be emphasized that this mechanism of energy transfer from a laser beam to the cluster

system has never been conceived nor proposed by those workers who have presented either the thermal model for lower excitation [Poa82] [Sin88] or the inverse bremsstrahlung process for much higher levels of excitation [Kim94] [Sin91a]

The optical in-situ system used by Kasuya et al and Nishina et al and others [Sch90] [Cha93] records the transient process of light emission from the plume of desorbed atoms from the solid target by projecting its light intensity in a coordinate system of (1) distance in millimeters in any two choices of the x, y and z directions, (2) time, t, in nanoseconds, and (3) wavelength, λ, ranging from 200 to 800 nano meters The streak camera displays a cross-sectional intensity distribution of any of the two choices of the coordinates.

The results of these measurements and others [Kas89a] [Kas89b] show the following characteristics of the intensity pattern: (1) the maximum intensity of light emission from the plume takes place in an area of a few tenths of a millimeter off the surface toward the z-direction and at a time a few nano seconds after the tail end of the 10 nano second laser pulse, and (2) the surface atoms expand in the vacuum into two different components. These two components are in marked contrast with each other in respective characteristics described as follows: (2a) one moves faster with wider distribution of velocity both in magnitudes and directions The other moves slower with a narrower distribution, (2b) the

area of maximum intensity corresponds to the slower component, and the outer area of weaker intensity the faster component, and (2c) the light emission from the faster component begins immediately after the end of the tail end of the laser pulse and the slower component is delayed by a few nano seconds. This delay is more significant for silicon, where the maximum emission takes place at the end of the laser pulse. Characteristics (2a-c) show that the plume expands into the vacuum in a way much more complicated than one would expect from the time integrated pattern

The velocity of the faster component exceeds 10^6 cm/S. On the other hand, a weakness in the intensity of visible line emission from the faster component suggests that the desorbed atoms carry lower energy in their internal electronic system than in their translational energy. This fact implies that the desorbed atoms are not excited by the inverse bremsstrahlung process, which is contradicted by Singh et al based on a range of experiments. Otherwise, the process would excite the system in both degrees of freedom in energy in comparable magnitudes. This result is consistent with another experimental fact that the faster component expands isotropically instead of travel in the direction of the incident laser beam, which [Kasuya et al] was tilted at 45° off-normal to the sample surface. If the faster component absorbed laser energy during its expansion, it would exhibit its maximum emission intensity in the time and space domains

of the maximum laser intensity.

The apparent difference between the internal energy and expansion energy of desorbed atoms may be explained if one assumes a transient process of a desorption and subsequent expansion. The process is analogous to a rapid release of compressed gas into a vacuum. Energy stored in the compressed gas is then converted into translational energy of expansion. The free expansion, for example, of a compressed gas into a vacuum in one direction yields its asymptotic expansion velocity $V_{\infty} = 2V_s / (\gamma-1)$, where V_s is the velocity of sound in the initial gas and γ is the adiabatic component. This value can be higher than the thermal velocity by a factor of 3.3 for monatomic gases. This asymptotic velocity, however, is still significantly less than the observed high velocity of the laser plume expansion ($\approx 10^6$ cm/s). Gurevich et al. treated desorbed atoms as a collection of partially ionized gas in a state of plasma. They take into account the Coulomb attraction between ions and fast-moving electrons and show that ions may be accelerated to a velocity comparable to the thermal velocity of electrons during their expansion [Gur66].

The slower velocity component is characterized by its delay of emitting visible light with respect to the laser pulse. In addition, the luminous plume emission progresses back toward the incident direction of the laser beam rather than point toward the normal surface as the laser beam is tilted from the normal toward the tangential.

These characteristics suggest that this component of desorbed particles absorb beam energy as they move (expand) away from the sample surface so that the intensity of the luminescence is higher in the beam area of higher laser intensity. The delay of luminescence has been observed by others under irradiation at higher intensities (over 10GW/cm^2) or for longer laser pulses (over 10 ns). In these cases, desorbed particles (atoms) are excited by the inverse bremsstrahlung process into multiple charged ions. Then light emission takes place initially from ions of highest charge multiplicity and subsequently from those of lower ones down to neutral atoms at later times as they recombine with electrons during the process of relaxation and expansion.

Kasuya et al analyzed the process of laser ablation by space/time resolved spectrometry with a streak camera system combined with a optical monochromator. For an intermediate level of laser energy fluence, the streak patterns in the x-y, z-t, and z-λ planes show many peculiar features overlooked in previous investigations. These features can be explained in terms of desorption of surface atoms in the form of clusters, but not in the expansion of a plasma of vaporized mono atoms or small molecules into the vacuum. The desorption of surface atoms in a cluster form may be regarded as a transient intermediate step of transition for surface atoms in a solid to atomic vapor. This process, with thermal models of surface excitation and the inverse bremsstrahlung process of post

desorbed excitation, provides a unified picture of a laser desorption in the entire region from low to extremely high intensity of excitation.

The results by previous investigators clearly show that, for the production of atomic and molecular species only during laser ablation, the energy densities have to be optimized to values just above the ablation threshold and the absorption coefficient of the incident laser beam has to be maximized with absorption coefficient values in the range of 10^6 cm^{-1}. Another important effect which needs to be considered is the plasma absorption of the incident laser beam. The absorption of laser energy by the plasma plays an integral role during the pulsed laser process as discussed previously by both Kasuya et al. and Singh et al.. A high temperature highly ionized plasma is formed when the laser activated material absorbs the laser beam. The fraction of the laser energy absorbed by the plasma is a strong function of a number of laser parameters, including laser wavelength, electron density, plasma dimensions and plasma temperature. Depending on these factors, the degree of plasma absorption can vary from 0% to nearly 100% of the incident laser energy. This plasma absorption can affect the target ablation characteristics in each of the above-mentioned regimes. A quantitative estimation of the energy absorbed by the plasma is very difficult due to the numerous complicated absorption processes occurring within the plasma within the plasma as

discussed previously by Kasuya et al. Okano et al. analysed the regime from the atomic layer removal regime in which layers of atoms are removed based on a weakly bonded atom formulation (WBA). Although Okano's model does not provide an understanding of the plasma interaction as the atomic layers leave the surface of the material, it does present an atomic viewpoint of the process in a fundamental fashion.

Based on the optical and the thermophysical properties reported above, two separate heating regimes have been identified: (i) the surface heating regime in which the laser energy is deposited at the surface and the thermal diffusivity of the material controls the ablation characteristics, and (ii) the volume heating regime in which the absorption depth is much larger than the thermal diffusion distance [Sin88]. In this case, the thermal diffusivity plays an insignificant role in the ablation characteristics. In the surface heating and planar ablation regime, the ablation depth should vary linearly with energy density. However, at higher energy densities, sub-surface superheating may result, which may lead to removal of material in the form of small particles from the target and non-planar movement of the vaporization interface.

This effect is more prevalent in the both heating regimes where absorption coefficient and thermal diffusivity are small. In this case, the high sub-surface superheating will lead to the removal of particles (chunk emission) in the initial stages of the laser pulse. The particles would in

turn shield the laser beam from the target, which would lead to an exponential dependence of ablation depth with energy density

Effect of Background-Gas Synergy

The unique ability of PLD to operate over a wide pressure range, including pressure up to 1 torr, requires an examination of the effect of energetic fluxes with the ambient gas. Two of the most important effects are the gas energetic flux chemistry and the gas-energetic flux collisions

Experiments on the PLD plume [Oti89] show that the kinetic energy, internal excitation and ionization state of the metallic species in the plasma cause enhanced oxidation of the metal in the passage through an oxygen background gas. This has been suggested to explain, at least in part, why the correct oxidation state of Cu is maintained for in situ deposition of $YBa_2Cu_3O_{7-x}$ superconductors. Therefore, the reduction of the activation energy for chemical reactions in the gas phase by kinetic energy and internal excitation, is another benefit of energetic fluxes. It can also help explain why ablated materials that contain species with vapor pressures that differ by as much as 10^6, deposit congruently in the film. The average energy of atoms in a PLD plume is on the order of 10 eV [Geo89] [Geo91] [Geo92] [Geo93]. The average energy is degraded by collisions with the ambient gas for pressures above 10 mTorr, and is nearly completely

thermalized in pressures of 300 mTorr used in the deposition of some films. Therefore, in PLD, the energy of the deposition flux may be controlled by means of the backfilled gas. Even more singular, however, is the directionality of the PLD plume. In all other techniques, at pressures above a few mTorr the flux is scattered by collisions (small mean free path) so that the deposition rate drops precipitously as the source-substrate distance increases or the pressure increases. In PLD, however, the plume is transported through high pressures to long distances due to a quasi-free jet expansion governed by hydrodynamics [Sin91] [Sin94]. The pulsed nature of the plume imparts forward momentum to the background gas, transporting the gas along so the plume and the gas drift to the substrate. So the high energy and extreme forward direction of the plume allow operation in high pressures of background gas.

Nano Particle Formation

The use of an ambient gas during pulsed laser ablation deposition can be characterized as either passive or active. Passive use of an ambient gas is mainly to compensate for some loss of a constituent element such as oxygen or nitrogen in ceramics. For example, deposited oxide ceramics tend to be deficient in oxygen when the ablation experiment is done in a high vacuum. Therefore, in-situ processing of oxide superconductors typically requires 10 300 mTorr of background

oxygen in the chamber during processing When this background gas is admitted during the laser ablation process, the mean nano particle size changes as the ambient gas pressure varies For example, by incorporating an ambient gas during laser ablation ultrafine nano particles can be fabricated with diameters ranging from a few nanometers to tens of nanometers The production of ultrafine powders of various metals (Fe,Ni, and Ti) and alloys (Ni-Ti, Fe-Ti, and Cu-Ni) in argon and helium atmospheres have been investigated [Mat86] [Chr94] and have shown distributions of nano particle sizes ranging from 1-70 nm with a pressure range of 1-200 torr The mechanisms for the formation of nano particles and (their pressure dependence due to an increase in the inert gas pressure) are most likely related to the increased collisions between the ejected species and the ambient gas as the ambient gas pressure increases At a pressure on the order of 1 mTorr, the mean free path is approximately 5cm The mean free path of the ejected species becomes 0 05 cm at a pressure of 100 mTorr When a laser ablation deposition experiment is done in a high vacuum, there are virtually no collisions between the ejected species before they reach the substrate When the ambient gas pressure increases, however, the vapor species can undergo enough collisions that nucleation and growth of these nano-particles can occur before their arrival at the substrate The fact that the nano particle size increases as the ambient gas pressure increases strongly suggests that the

ultrafine nano particles are formed from the vapor species instead of liquid droplets. Therefore, longer residence times (higher ambient gas pressures) yield larger nano particle sizes. The specific effects of target-to-substrate distance and ambient gas pressure are interrelated. Due to the increased collisions between the laser-induced plume and the background gas, the plume dimension decreases as the background gas pressure increases. It has been shown [Dys88] that E/P_a is the scaling parameter for plume range, where E is the laser-pulse energy and P_a is the background gas pressure. The length of the plume (L) is proportional to the scaling parameter, as $L \propto (E/P_a)^{1/3\gamma}$, where γ is the ratio of the specific heats (C_p / C_v) of the elements in the plume. When the target - substrate distance is much smaller than L, there is a marked difference in particulate size and density. As the target - substrate distance increases, the proportion of the smaller particulates decrease and a few larger particles appear to suggest a merged transition during flight [Nis91].

CHAPTER 2
EXPERIMENTAL PROCEDURES

Experimental Setup

A modified pulsed laser deposition technique was used to deposit nano particle coatings on particulate materials This technique is distinguished by its ability to make very thin, uniformly distributed and discrete coatings in particulate systems so that the properties of the core particles can be suitably modified An example of a composite particulate material is shown in Fig 2 1 Figure 2 1 shows that the surface of the core particle is modified by the attachment of the secondary nano-particles By controlling the operating conditions a wide range of engineered particulates can be synthesized The surface architecture of the coatings can range from discrete coatings as shown in Figure 2 1 (a) to continuous coatings shown in Figure 2 1 (b) Figure 2 2 shows a schematic diagram of the system used to fabricate the particulate coatings An excimer laser irradiates the target material through the ultraviolet transparent quartz window. The laser plume that is directed perpendicular to the target material is directed onto a desired surface

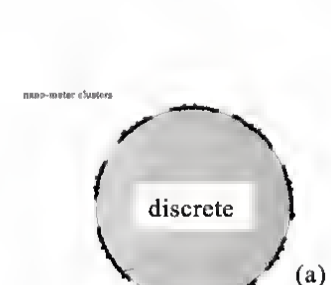

Figure 2-1 Schematic illustrations showing the concept of a nano functionalized particulate material. Depending upon the synthesis parameter, discrete (a) and continuous (b) coatings can be synthesized

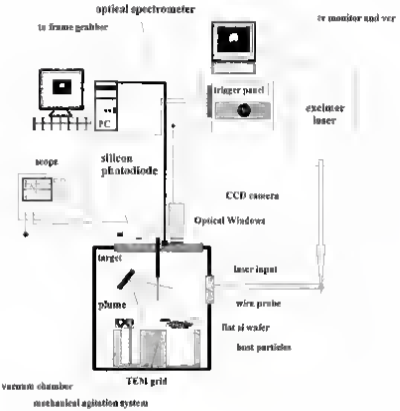

Figure 2.2 Experimental pulsed laser deposition setup In-situ characterization by CCD imaging, optical spectroscopy, wire probe, photo diode measurements are shown The laser triggering system allows for time input through the many techniques when couple with a multi channel digitizing oscilloscops

Deposition onto two different types of surfaces were prepared using the geometry shown in Figure 2.2. The corresponding deposition parameters are listed in Tables 2.1, 2.2 and 2.3.

Experimental Descriptions

A Lambda Physik model LPX 305i pulsed excimer laser was utilized as an energy source to create a plume of excited species during processing. The output of the excimer laser has an operating wavelength of 248 nm when operated with a krypton-fluoride gas mixture. The time duration of the output laser pulse is 25 ns with a rectangular shape and gaussian distribution. A computer laser interface allows control of the incident beam energy as well the laser repetition rate that can be varied from 1-50 HZ continuous. The computer interface can also accommodate both a triggering and a synch output pulse, both with a TTL pulse protocol. Due to the time regime that the processes being described occur (≤ 100μs), having a time-triggering relationship with a laser input and output is critical for in-situ measurements. To insure proper energy during deposition, the laser output energy was calibrated and recorded by a Gentec laser energy meter with a SUN series reading head model# ED 500 before each deposition. As shown in Figure 2.2, the pulsed laser beam irradiates the solid silver sputtering target through the ultraviolet transparent quartz window. The laser generated plume is directed onto a fluidized bed of core particulate substrate materials. Depositions onto two different surfaces were prepared using

the geometry shown in Figure 2. As stated above, except for the core particle suspension system, this technique resembles a standard PLD system. Powder samples that are listed in Table 2.1 were placed into an aluminum crucible as shown in Figure 2.3. The crucible was then locked into the mechanical agitation system and the solid target system was lowered into placed. The mechanical agitation is a critical element in synthesis of engineered particulate coatings. Problems associated with agitating powders ranging in size from 0.5-1000 μm in a vacuum are numerous. Mechanical agitation of the core Al_2O_3 particles will be achieved by a vibrational technique as shown in Figure 2.3 with the intent to control the motion of the core particles during exposure to the laser induced flux of nano-clusters. The mechanical vibration will originate from a high speed motor with a designed off-axis weight attached. By controlling the speed of the off-axis weight, the magnitude of the vibrational displacement can be modified. Due to the vibrational displacements, isolation of the motor is required using a system of springs and damping materials. Four main parameters describe the fluidization system: the speeds (rpm) of the attached motor, off-axis rotating weight, spring stiffness of the clamp springs and the size of the core particles. The speed of the motor was control by an Instek 0-18 volt dc power supply model # PS-18300. Figure 2.4 shows the speed of the offset weight as a function of input voltage. The rotating mass is made out of

stainless steel with a series of tapped holes throughout the disk. The tapped holes allow for the addition or subtraction of smaller masses for adjustment of vibrational imbalances. During powder processing the mechanical agitation system was operated in a continuous fashion at room temperature. The system was then pumped down to 20 mTorr and backfilled with the required gases as required. A baratron pressure transducer model #127AA with a range from 1 mTorr - 2 Torr and a power supply readout model PDR-C-1C were used in the experiments. The pressure was adjusted for each gas used with a MKS model # 247C mass flow controller with a 4-channel readout.

Samples

The parameters governing the depositions onto the three surfaces are listed in Tables 2.1 and 2.2. Table 2.1 lists the processing parameters for coating 18 micron Al_2O_3 core particles. These parameters will now be discussed. Column 1 on the left side describes the material systems investigated, one example is Ag/Al_2O_3, which denotes an Ag nano particle coating on Al_2O_3 core particles. Column two is the sample identification, an example is P2A, P2 refers to a sample processed in a backfilled atmosphere of 200 mTorr and A refers to helium as the backfill gas. The gas pressures are denoted by a 2 or a 6 meaning 200 or 600 mTorr respectively and the gas types are arranged with the following key:

- helium = A
- neon = B
- argon = C
- krypton = D
- oxygen = E

Column 3 lists the size of the powder samples as measured by the scanning electron microscope. Electron micrographs of the surface morphology and sizes of the Al_2O_3 core particles will be shown in detail in Chapter 3. Column 4 lists the amount of the core particles processed for each sample. Core particle samples weighed using a mass balance by the Denver Instruments Company model A 200DS. Column 5 denotes the processing time for each sample in minutes. Column six lists the operating voltages for the two DC motors operated during processing. The first number in column 6 refers to the input voltage for the target rotation motor, and the second refers to the input voltage to the mechanical agitation motor. Noting here that the speed of the mechanical agitation system controls the rate at which the Al_2O_3 core particles are exposed to the laser induced is important plume therefore controlling coating uniformity and thickness. Column 7 list the laser energies used during the deposition and the laser repetition rate. For the Al_2O_3 powder samples the repetition rate was maintained at 10 hz, which means that each powder sample was exposed to the laser induced plume 9000 times during deposition. Column 8 lists the system pressure maintained during the deposition. Because of many similarities between Tables 2.1 and 2.2, only the differences will be listed for Table 2.2. The mesh grids

were processed in the same format as the powder samples with the following exceptions being noted The mechanical agitation system was disabled and a flat 3" silicon wafer was placed over the aluminum crucible on which the mesh grids were placed during deposition Table 2-2 lists the parameters for deposition onto mesh grids Column 2 lists the sample identification, for example G2A refers to a mesh grid processed in a helium atmosphere, backfilled to 200 mTorr Column 3 lists the number of laser pulses applied to each mesh grid

Table 2.1 Deposition on Particulate Materials

1	2	3	4	5	6	7	8
Material System	XP #	Size (μm)	Mass (gm)	Time (min)	Motor (volts)	Energy (J/cm²) Rate (hz)	Pressure (mTorr)
Ag/Al_2O_3	82A	10	4	15	1 26 4 79	2 25 10	200 Ne
Ag/Al_2O_3	P6A	10	4	15	1 26,4 79	2 25 10	600 Ne
Ag/Al_2O_3	P2B	10	4	15	1 26 4 79	2 25 10	200 Ne
Ag/Al_2O_3	P6B	10	4	15	1 26 4 79	2 25 10	600 Ne
Ag/Al_2O_3	P2C	10	4	15	1 28 4 39	2 25 10	200 Ar
Ag/Al_2O_3	P6C	10	4	15	1 25 4 80	2 25 10	600 Ar
Ag/Al_2O_3	P2D	10	4	15	1 28,4 39	2 25 10	200 Kr
Ag/Al_2O_3	P6D	10	4	15	1 25 4 80	2 25,10	600 Kr
Ag/SiO_2	82C Si	110	11	45	1 14 4 6	2 3 20	200 Ar

Table 2 2 Deposition on Mesh Grids

1	2	3	4	6	6
Material System	ID#	Pulses	Meter (volts)	Energy (J/cm²) Rate (hz)	Pressure
Ag/TEM Grid	G2A	100P	1.26	2.25. 1	200 Ne
Ag/TEM Grid	G6A	100P	1.26	2.26. 1	600 Ne
Ag/TEM Grid	G2B	100P	1.26	2 25. 1	200 Ne
Ag/TEM Grid	G6B	100P	1 26	2 25. 1	600 Ne
Ag/TEM Grid	G2C	100P	1.26	2 26 1	200 Ar
Ag/TEM Grid	G6C	100P	1 26	2 26, 1	600 Ar
Ag/TEM Grid	G2D	100P	1 26	2 25 1	200 Kr
Ag/TEM Grid	G6D	100P	1 26	2 26. 1	600 Kr
Ag/TEM Grid	G2e	100P	1 26	2 25. 1	200 O_2
Ag/TEM Grid	G6E	100P	1 26	2 26. 1	600 O_2

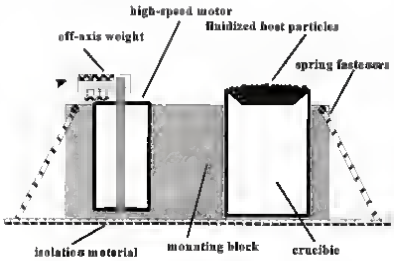

Figure 2.3 Experimental core particle mechanical agitation apparatus. The apparatus uses a high speed motor with a designed imbalance to create an off axis vibration which is transmitted to the core particles during deposition. Isolation of the mechanical vibration is by a system of springs and rubber damping materials.

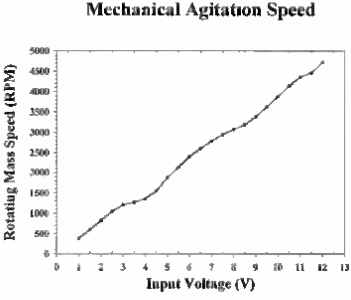

Figure 2 4 Measured speed of the rotating mass as a function of input voltage

Experimental Characterization Techniques

Several in-situ measurement techniques were used to analyze the system during processing. To fully characterize the proposed particulate coatings, a number of characterization techniques were be used. The properties of the proposed coatings that will be examined are uniformity, composition, thickness and structure. Techniques that were used are listed with respect to whether the technique is an in-situ measurement or it is made analytically.

Optical Spectroscopy

In-situ optical spectroscopy was performed in-situ during experiments to both qualify the laser-induced plume and to examine the effects of different inert gases in the system during processing. An Ocean Optics model # S1000 miniature fiber optic spectrometer that has a range from 350 850 nm with a resolution of 1 nm was used to perform this. The fiber optic probe was mounted as shown in Figure 2.2

Wire Probe Measurements

In-situ wire probe measurements were obtained to determine the speed of the ionized species as a function of backfill gases and pressures during processing. A Tektronix model TDS 520A two channel digitizing oscilloscope operating at 500 MHZ with a sampling rate of 500 MS/s was used with a

triggered output from the laser to look at timed response from the wire probe during processing

Photodiode Measurements

A Newport model # 818-BB-21 battery biased silicon PIN detector with a time resolution of 2 ns, and an optical range from 300 nm-1.1 μm was used in-situ with a triggered laser output and the oscilloscope to record the optical emission from the plume during experiments

Fast CCD Camera Measurements

A Pulnix model TM-9701 progressive scan full-frame shutter camera with a 2/3" progressive scanning interline transfer CCD imager 768 (H) x 484(V) with a custom built external triggering circuit was used to obtain in-situ video measurements The camera was fitted with a Navitar zoom lense model 52174 with a zoom focal length from 18-108 mm, manual iris control This type of lense allows imaging from a distance of 6" - 12", with an optimum resolution 30 μm. This large zoom distance is valuable since it allows monitoring outside the chamber through a viewport The camera was triggered with respect to the laser pulse by an external double initialization pulse as shown in Figure 2.5 This design allows both time resolved measurements and continuous video measurements The output from the camera can be obtained in two forms: continuous or triggered. Both outputs can be recorded by a tv-vcr in real time as shown in Figure

2-2- The output can also be grabbed into a computer for further processing. A Pulsar PCI frame grabber baseboard with integrated display up to 1600 x 1200 and 4 Mb of onboard WRAM was used to capture images in situ during processing. With this configuration the following processes can be analyzed in-situ:

- Continuous plume monitoring
- Time resolved plume imaging
- Continuous particle fluidization monitoring
- Time resolved fluidization

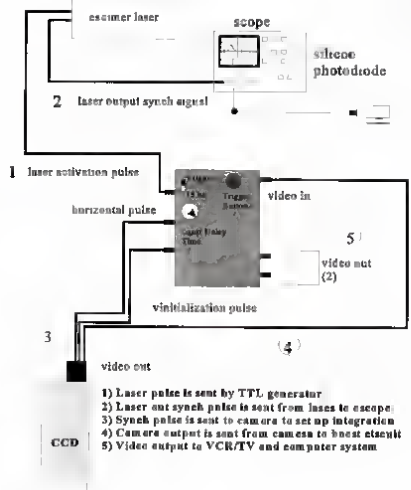

Figure 2.5 Test triggering circuit schematic for in-situ wire probe, CCD camera, and photo diode measurements.

Laser Ablation Depth Measurements

Laser ablation depth measurements from solid target surfaces were conducted to obtain quantitative information with respect to deposition/removal rates from a solid silver sputtering target. This information was then used to estimate nano particle formation and laser induced plume densities. Figure 2.2 shows the experimental setup used to perform this experiment, during the laser irradiation the ablation target was stationary. The ablation target was irradiated with the required number of pulses and then rotated to a new position, proving a new target surface. Laser pulse amounts were chosen to be 300, 1000, and 1500. The system was backfilled at 200 mTorr as described above and a laser repetition rate of 1 Hz was used. The laser irradiated surface areas were then measured by a Dek Tak profilometer as shown in Figure 2.6. Profilometer measurements were made perpendicular to the axes as shown.

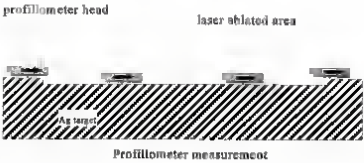

Figure 2-6. Schematic of profilometer ablation depth measurement

Auger Electron Spectroscopy

Auger electron spectroscopy (AES) was conducted to analyze the properties of the laser deposited coatings on both alumina particles and flat silicon wafers. A model Perkin-Elmer PHI 660 scanning Auger Multiprobe was used. This instrument uses a focused electron beam to stimulate the excitation of auger electrons from the top 3-4 atomic layers of the material surface. The kinetic energy of these electrons is characteristic of the atom from which they originated and enables the detection of all elements except He and H. By taking advantage of this shallow depth information, the distribution of the atomic species also can be measured in the third dimension by using an ion gun to remove successive layers of the material. Sample preparation for AES analysis was short. Powder samples were prepared for AES by pressing the powder onto indium foil. The samples were then put into a high vacuum load lock and analyzed.

Micro Probe Analysis

A Jeol EPMA Superprobe model 733 with EDS capability was used to obtain wavelength dispersive x-ray (WDX) surface maps of the laser deposited Ag coatings on the surfaces of alumina particles. This instrument incorporates up to 4 spectrometers that can obtain both qualitative and quantitative information from thin films with respect to known standards. Samples were prepared by applying a thin layer of carbon paint onto an

aluminum sample mount Particles were then introduced onto the surface of the mount and retained by the curing carbon paint Sample mounts then underwent a carbon evaporation process (in the case of non-conductive samples) prior to characterization

X ray Photo Electron Spectroscopy

This analytical technique was used to analyse the relative changes in surface coverage of Ag on the core particles of alumina with respect to various background gases and pressures. The instrument used was a Kratos analytical surface analyzer model XSAM 800. This technique uses single wavelength x-rays to stimulate the excitations from the top 3-4 atomic layers of the surface. Samples were prepared by applying a thin layer of carbon tape onto a stainless steel sample mount An amount (0.5 gm) of the powder sample to be analyzed was placed on the mount, after removing the excess the sample was ready for analysis. Samples were prepared by applying a thin layer of carbon paint onto a stainless steel sample mount Particles were then introduced onto the surface of the mount and retained by the curing carbon paint

Scanning Electron Microscopy

A Joel model 6400 EDS scanning electron microscope (SEM) was used to obtain information on the surface morphology, size and shape before and after processing on the alumina powder and silicon wafer samples. Powder samples were prepared by

applying a thin layer of carbon paint onto a graphite sample mount. Particles were then be introduced onto the surface of the mount and retained by the curing carbon paint. The first silicon wafer samples were prepared by applying a thin layer of carbon paint onto an aluminum sample mount. The first wafer samples were then be introduced onto the surface of the mount and retained by the curing carbon paint. Sample mounts then underwent a carbon evaporation process (in the case of non-conductive samples) prior to characterization.

Transmission Electron Microscopy

A Jeol 400FX HREM high resolution and analytical transmission electron microscope (TEM) with a PGTIMIX EDS system was used to examine the coating thickness and nano-particle structure at magnifications up to 800,000X. Because not all samples required high-resolution, lower magnification samples (up to 200,000X) were examined by a Jeol 200CX analytical transmission electron microscope.

Samples were prepared by three methods. The first method will employ deposition of nano-clusters directly onto a carbon-formvar mesh grid as previously discussed in Table 2-1. This grid was then mounted in the TEM for characterization. This sample preparation technique yields information on the nano particles with respect to size and structure directly from the flux prior to core particle coating. A second method was to mix the core particulate materials in an epoxy matrix.

Sample disks were then be punched out of the particle-epoxy matrix and ion milled to the required thickness for characterization. This method was used to obtain structural information with respect to the nano particles on the core particles in thickness, structure. The third method of sample preparation was to take the coated core particulate samples and crush the powder with a morter & pestle. The finer particles were then suspended in an ethanol solution. A mesh grid was then placed into the solution and removed, retaining some of the composite, finer particles for analysis.

Scanning Transmission Electron Microscopy

One of the difficulties associated with conventional TEM is identifying between sample thickness variations and diffraction artifacts. In these kinds of particulate materials, the interface structure between the core particle and the nano particle play a crucial role in controlling their properties. Scanning transmission electron microscopy (STEM) was performed to gain information concerning the crystal structure and the interface between the nano particles and the core particle substrate. The STEM has a higher probe resolution (1.3 -2 2 Å), combined with the ability to perform Z-contrast imaging in addition to having a conventional TEM head mounted in the same system. This is important for data interpretation such that both STEM and conventional TEM images can be taken simultaneously for exact comparison. The

scanning transmission electron microscope (STEM) is designed to form a small electron probe scanned across a thin specimen as shown in Figure 2.7. A model VG HB603U with a 300 kV accelerating voltage and a Scherzer resolution of 2.2Å was used to perform the analysis. With a crystalline specimen aligned parallel to the beam, the probe preferentially channels along the atomic columns, one by one as it is scanned across the specimen. A Z-contrast image results from mapping the intensity of the electrons scattered through relatively large angles, using an annular detector. Because of the large size of the detector, phase contrast effects between different Bragg reflections are integrated to give an image based on total scattered inteneity. As high angle scattering becomes predominantly from the atomic nuclei, bright features in the image correspond directly to columns of atoms, with the brightness determined by their relative atomic number. Unlike conventional high resolution electron microscopy (HREM), this technique allows the positions of atomic columns to be determined directly and uniquely from the image to a high accuracy, without the need for extensive simulation of model structures. This technique provides incoherent images of the atomic structure of materials and bypasses some of the phase problems associated with HREM.

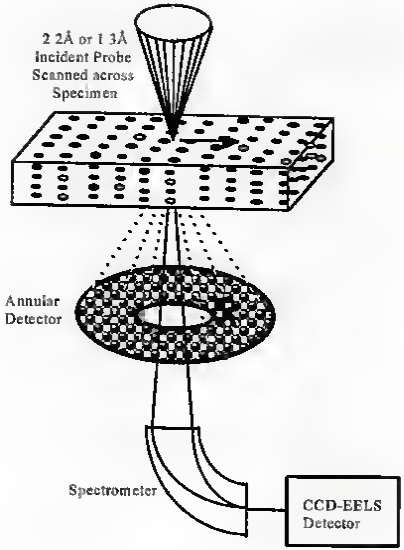

Figure 2.7 Schematic showing Z-contrast imaging and atomic resolution combined with electron energy loss spectroscopy (EELS) on a scanning transmission electron microscope

CHAPTER 3
EXPERIMENTAL RESULTS

In this Chapter the results from target ablation, CCD camera imaging, optical spectroscopy and wire probe measurements will be presented followed by results from powder synthesized and mesh TEM grid experiments.

Silver Target Ablation Measurements

To properly develop an understanding for the materials being deposited during pulsed laser deposition (PLD), it is important to develop information with respect to material removal rates per pulse and effective atomic flux densities. Figure 3.1 shows the Ag sputtering target following ablation under the same condition described for sample P2C in Chapter 2. Figure 3.2 presents the results of the profilometer measurements recorded over the laser ablation areas. These measurements were used to estimate the quantity of Ag atoms removed per pulse and the number of nano-particles that could be formed as shown in Table 3.1. A partial listing of the nano particle calculations is shown in Table 3.2. All calculations are in Appendix A.

Figure 3.1 Geometry characteristics of an Ag sputtering target post excimer laser ablation

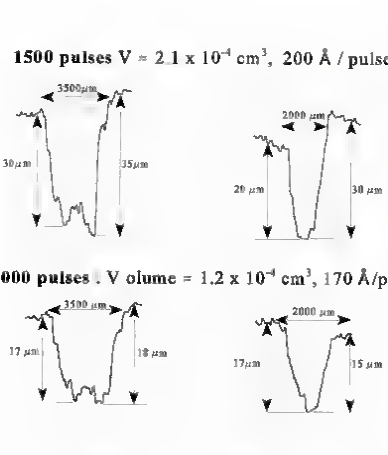

Figure 3.2 Profilometer measurements taken from the laser ablated areas shown in Figure 3.1.

Table 3 1 Results From Laser Ablation Calculations

# pulses	Volume (cm^3)	a_0 (Å)	Depth (Å)/pulse	Ag atoms per pulse	Number of nano particles/pulse
300	$5 10^{-9}$	4 08	200	$5 49 10^{15}$	$2 55 10^{13}$
1000	$1 2 10^{-4}$	4 08	170	$3 95 10^{15}$	$1 83 10^{12}$
1500	$2 1 10^{-4}$	4 08	230	$4 62 10^{15}$	$2 14 10^{12}$

Table 3 2 Summary of Calculations

Nano particle = NP	Core particle = CP
Radius NP = 2 5x10^{-7} cm	Radius CP = 9x10^{-4} cm
a_o NP = 4 08x10^{-8} cm	a_o CP = 4 08x10^{-8} cm
Density Ag = 10 5 gm/cm^3	Density Al_2O_3 = 3 96 gm/cm^3
Volume NP =6 545x10^{-20} cm^3	Volume CP = 3 054x10^{-9} cm^3
Surf area NP = 7 854x10^{-12} cm^2	Surf area CP = 1 018x10^{-8}cm^2
S/V ratio NP = 1 2x10^{8} cm^{-1}	S/V ratio CP = 3 33x10^{3} cm^{-1}
Mass NP = 6 872x10^{-19} gm	Mass CP = 1 203x10^{-8} gm
Surf area NP/gm = 1 1x10^{6}cm^2/gm	Surf area CP/gm = 841 75 cm^2/gm
# NP/gm = 1 455x10^{18} /gm	# CP/gm = 8 27x10^{7} /gm
# Ag atoms/NP = 3 855x10^{2} #/NP	
# of NP for complete surf coverage on a CP = 5 18x10^{7} NP	

Charge Coupled Device Camera (CCD) Measurements

As described in Chapter 2, the CCD camera was used visually to observe the nano-particle deposition technique in real-time. This provides both a powerful visual tool for understanding and presenting the technique. Figures 3.3 (a)-(f) show the effect of pressure on the size of the laser plume with an incident laser energy of 2.3 J/cm^2. As discussed previously in Chapter 1, backfilled gas pressures affect the mean free path and apparent volume expansion characteristics of the laser-induced plume, which are clearly shown by comparing Figures 3.3 (a) and (f). These CCD images were recorded without time gating the CCD camera. Instead the images were grabbed to a frame grabber board while the laser was operating at a 30-Hz repetition rate. Operating the laser at this frequency removes frequent errors that are typically associated with convention video recording speed, which is 30 frames/sec. The effects of the pressure changes on the nano-particle formations were found significant and will be presented by TEM analysis in a later section.

Figure 3.4 shows a typical deposition sequence during deposition as observed from CCD imaging system. Significant changes in contrast due to the nano particle coatings can clearly be observed in the images. The imaging of powder during processing in Figure 3.4 was performed on larger 500 μm Al_2O_3 powder to maximize the resolution capabilities of the

zoom lenaa uaed. Figure 3.4(a) ahowa the powder before depoaition, while Figurea 3.4 (b) and (c) represent images taken during and after depoaition reapectively.

The CCD imaging by time window triggering of the laser-induced plume waa recorded to develop an underatanding of the expanaion process with raapect to Ag ablation at a backfill preaaura of 200 mTorr. Figure 3.5-1 (a) (f) ahow a time-reaolved hiatory of the laser induced optical emiaaion during proceaaing. Each time image ia taken 15 μs apart for a total of 90 μaec. Figure 3.5-2 (a) - (f) ahow the expansion proceaa aa a function of intenaity with more detail. Falae grayacale aa a function of intanaity waa added with a 10 bin distribution further to ahow the ahifta in intenaity aa a function of time and diatance.

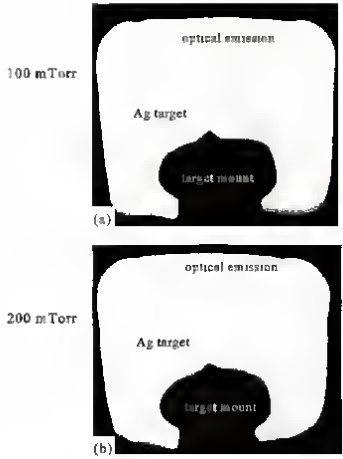

Figure 3 3 CCD camera imaging of the laser ablation plume- (a) 100 mTorr, and (b) 200 mTorr respectively

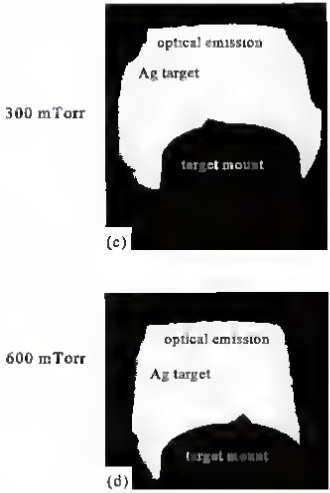

Figure 3.3 continued, CCD camera imaging of the laser ablation plume at (c)300 mTorr, (d) and 600 mTorr respectively

800 mTorr

1 Torr

Figure 3 3 continued, CCD camera imaging of the laser ablation plume at (e) 800 mTorr, and (f) 1 Torr respectively.

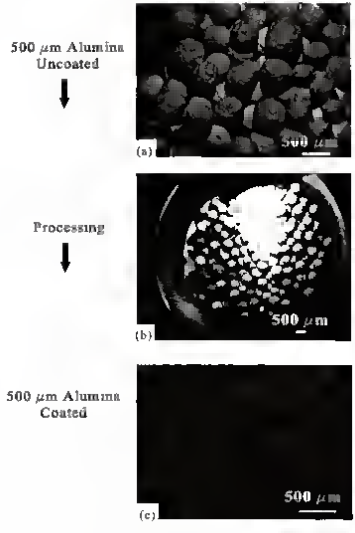

Figure 3 4 CCD images showing the nano particle coating process (a) before nano particle deposition. (b) during deposition, and (c) after nano particle deposition

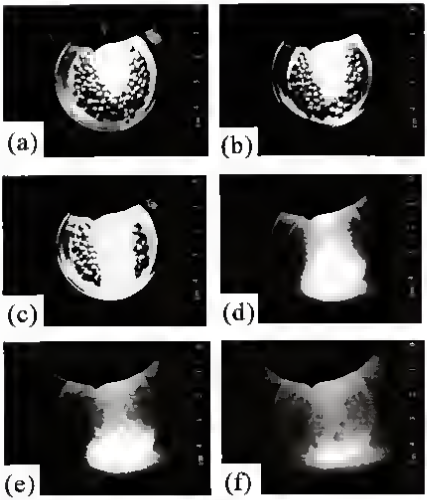

Figure 3.5.1 Time-gated CCD plume imaging taken during deposition.

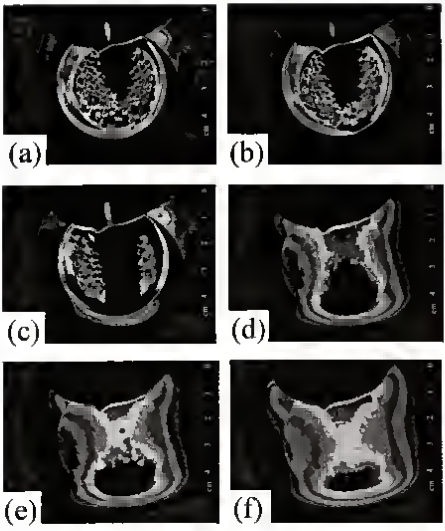

Figure 3.5.2 continued, Time-gated CCD plume imaging taken during deposition with 10 bin grayscale false color showing areas of higher intensity

Optical Spectroscopy

In-situ fiber optic spectroscopy was used to examine the optical emission spectra of the laser-induced plume. Figure 3.6 (a)-(c) show the optical emission spectra for 5 different backfill gases at 200, 600 and 900 mTorr respectively. It was expected that the heavier molecular weight gases would yield higher intensity spectra due to an increase in the collision frequency. In comparison to known atomic emission line standards [Lid95], six atomic lines for atomic Ag can be observed. Table 3.2 lists the reference and the observed atomic line emissions. Comparison of the data shows that the observed spectrum is in good agreement with the reference lines for neutral atomic silver emission.

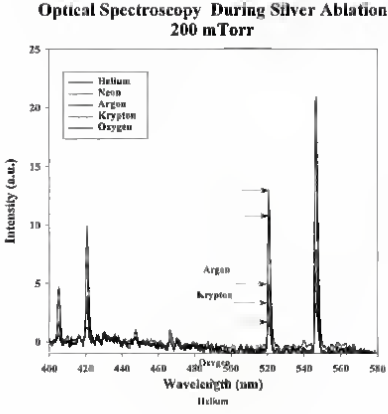

Figure 3 6 Multiple optical emission spectra obtained during continuous laser ablation of Ag in backfill gases of He, Ne, Ar, Kr, and O at (a) 200 mTorr chamber pressure

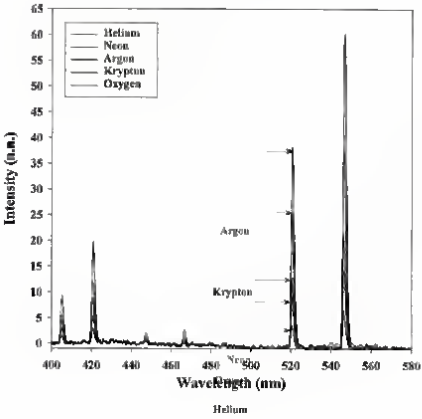

Figure 3 6 continued, Multiple optical emission spectra obtained during continuous laser ablation of Ag in backfill gases of He, Ne, Ar, Kr, and O_2 at (b) 600 mTorr chamber pressure

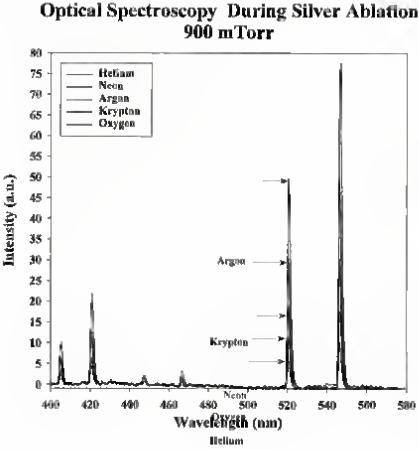

Figure 3.6 continued, Multiple optical emission spectra obtained during continuous laser ablation of Ag in backfill gases of He, Ne, Ar, Kr, and O_2 at (c) 900 mTorr chamber pressure.

Table 3.2 Reference and Observed Atomic Line Emissions

Observed (nm)	Reference (nm)
405.34	405.50
420.84	421.09
447.59	447.60
466.76	466.80
520.59	520.80
546.76	546.50

Wire Probe Measurements

In-situ wire probe measurements were conducted using time-resolved fast triggering methods as discussed previously in Chapter 2. Wire probe measurements were conducted to examine at the change in velocity of the charged Ag species during ablation into different backfill gases while varying the pressure. Figure 3.7 presents the measured velocities for positively charged Ag species as a function of backfill gas pressure into varying molecular weight gases. Average velocities in the range of 10^5-10^6 cm/s are in good agreement with similar ablation measurements of $YBa_2Cu_3O_{7-x}$ done in oxygen by Geohegan et al. From this it is also clear that the velocity of the Ag species is proportional to the molecular weight of the backfill gases. As expected from classical collision theory, the velocities of the silver ion species decreased as a function of backfill gas molecular weight and pressure respectively.

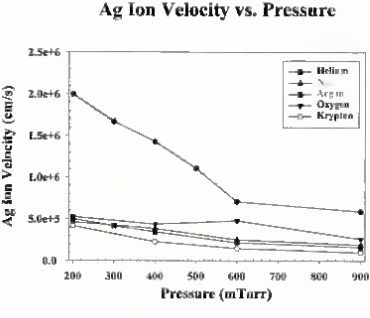

Figure 3 7 Time – triggered single pulse wire probe velocity measurements of Ag ions as a function of backfill gas and pressure.

Powder Synthesized Samples

As discussed previously in Chapter 2 nano-particle Ag coatings were deposited on two different particulate systems, Al_2O_3 and SiO_2 with measured diameters of 13 and 100 μm respectively Several characterization methods were employed to investigate the nano-particle formation and coating mechanisms, and the results of these methods will now be presented Due to the fact much of the characterization is redundant meaning, for example, with SEM microscopy nano-particle features and coating thicknesses are below the resolution of the microscope used, full presentation of SEM characterization of all coated samples is not necessary Therefore, representative data will be shown with respect to each characterization technique

Scanning Electron Microscopy

This technique was used to obtain to obtain size measurements and morphological characteristics of the uncoated samples in comparison to the coated samples It should be noted that the samples did change color significantly before and after processing from bright white to a light, lime green which is similar in color to commercially available Ag nano particles Figure 3 8 (a) and (b) show low magnification SEM images of uncoated Al_2O_3 powder (a) and coated sample P2C (b) Figures 3 8 (c) and (d) shows SEM images of uncoated Al_2O_3 powder Figure 3 8 (e) and (f) shows SEM images of Ag nano-particle

coated Al_2O_3 powder. In comparison of Figures 3.8 (a)-(f), it can be readily seen that no significant change in morphology is present due to the nano-particle synthesis. Since the nano-particles could not be imaged on the surface, energy dispersive x-ray (EDX) was also performed to detect the coating. Figure 3.9 shows an EDX spectra taken from the surface of a coated alumina particle, sample P2C. The EDX spectrum shows that Ag is present on the surface of the coated sample although no information with respect to coating thickness, coverage or phase can be obtained. Figures 3.10 (a)-(d) shows SEM images of sample P2CS1. In this system Ag nano-particles were deposited onto SiO_2 core particles 100 μm in diameter. The use of SiO_2 as a substrate was chosen due to the inherent roughness associated with the surface of Al_2O_3.

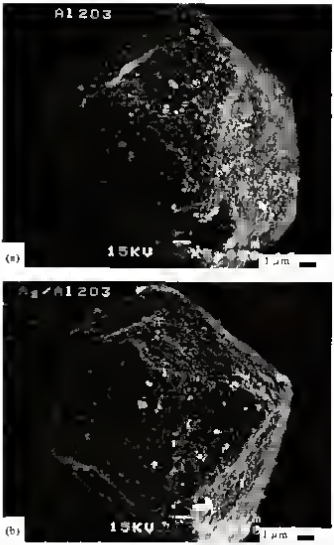

Figure 3.8 SEM micrograph images of uncoated (a) and nano particle coated (b) Al_2O_3 particulate samples at 5,000 X

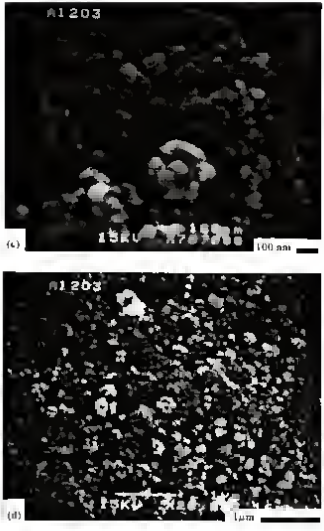

Figure 3 B continued, Higher magnification electron micrographs of the surface of uncoated Al_2O_3 particulates at 70,000 X (c) and 20,000 X (d).

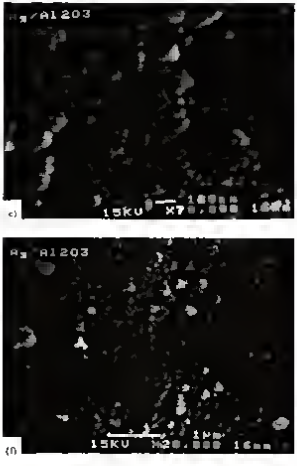

Figure 3 8 continued, Higher magnification electron micrographs of the surface of coated Al_2O_3 particulates at 70,000 X (e) and 20 000 X (f)

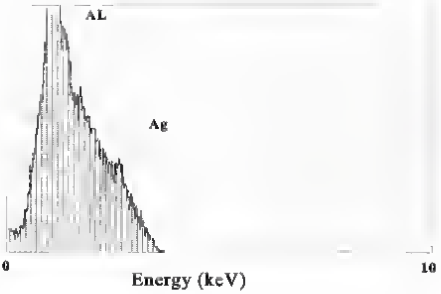

Figure 3.3 Energy dispersive x ray (EDS) spectra of an Al_2O_3 particle coated with Ag nano particles. Although the spectrum shows the presence of Ag, the amount and thickness cannot be determined

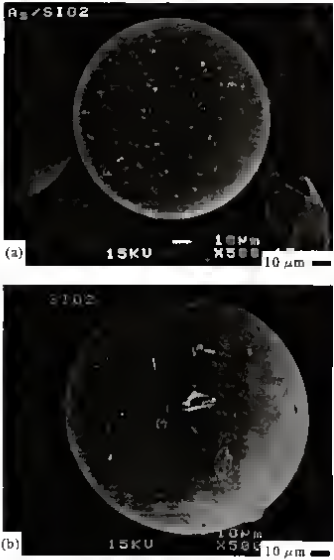

Figure 3 10 Low magnification electron micrographs of (a) Ag nano particles on SiO_2, and (b) uncoated SiO_2

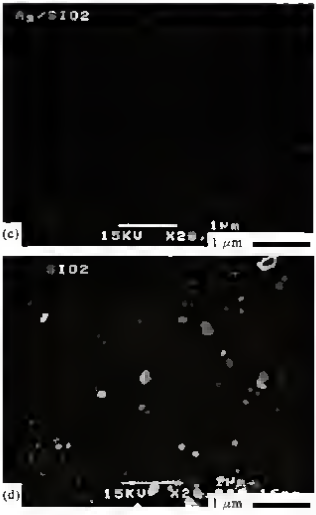

Figure 3.10 continued Higher magnification electron micrographs of (c) Ag nano particles on SiO_2, and (d) uncoated SiO_2

X-ray Photo Electron Spectroscopy

X-ray photo electron spectroscopy (XPS) was used to examine the relative surface coverage of Ag nano particles on Al_2O_3 core particles as a function of background gas molecular weight and pressure. Figure 3.11 shows the results of quantitative analysis of Ag surface coverage, relevant calculations based on the raw XPS data has been placed in Appendix B. Both the molecular weight and pressure of the backfilled gas appear to modify the deposition characteristics with respect to surface coverage in this system.

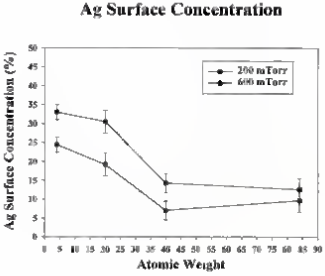
Ag Surface Concentration
Ag Surface Concentration (%)
200 mTorr
600 mTorr
0 5 10 15 20 25 30 35 40 45 50 55 60 65 70 75 80 85 90
Atomic Weight

Figure 3:11 Concentration of Ag coating measured by x-ray photo electron spectroscopy as a function of backfill gas atomic weight at 200 mTorr and 600 mTorr It is clear that the molecular weight and pressure of the backfill gasses can vary the efficiency of the deposition process

Deposition on Mesh TEM Grids

Deposition of Ag nano particles onto mesh TEM grids were performed to examine the effects of backfill gas molecular weight and pressure on nano particle formation. Figures 3.12 - 3.16 present the results of Ag nano particle depositions performed in backfills of helium, neon, argon, krypton and oxygen respectively. Each grid received 100 pulses during deposition at the respective pressure. Figure 3.17 shows a TEM diffraction pattern taken from the Ag nano particles on the grid, ring radius calculations show that the pattern suggests a polycrystalline Ag structure, in good agreement with high magnification TEM that will be discussed in Chapter 4.

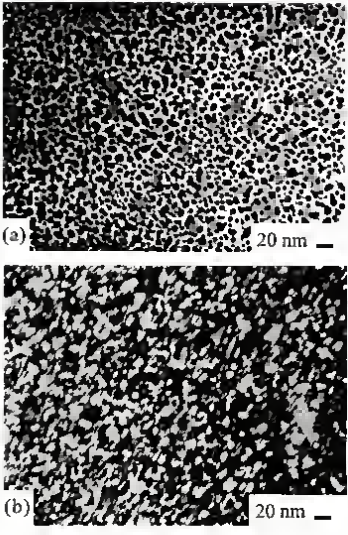

Figure 3.12 Transmission electron micrographs of Ag nano particles collected on carbon-formvar grids at (a) 200 mTorr and (b) 600 mTorr respectively. Deposition was carried out with helium as the backfill gas

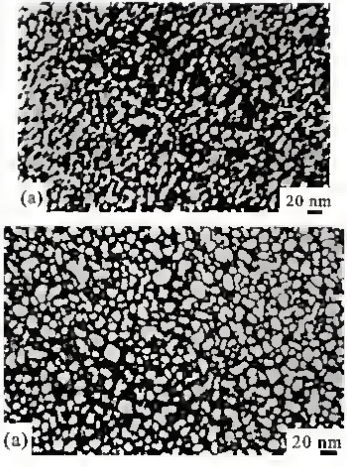

Figure 3.13 Transmission electron micrographs of Ag nano particles collected on carbon-formvar grids at (a) 200 mTorr and (b) 600 mTorr respectively. Deposition was carried out with neon as the backfill gas

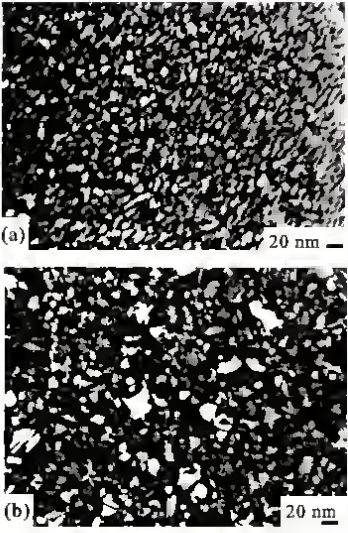

Figure 3.14 Transmission electron micrographs of Ag nano particles collected on carbon formvar grids at (a) 200 mTorr and (b) 600 mTorr respectively. Deposition was carried out with argon as the backfill gas

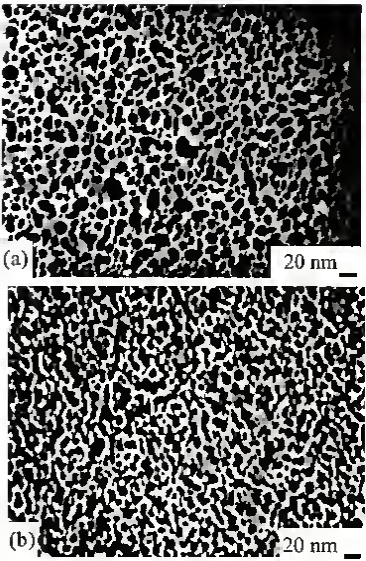

Figure 3 15 Transmission electron micrographs of Ag nano particles collected on carbon -formvar grids at (a) 200 mTorr and (b) 600 mTorr respectively Deposition was carried out with krypton as the backfill gas.

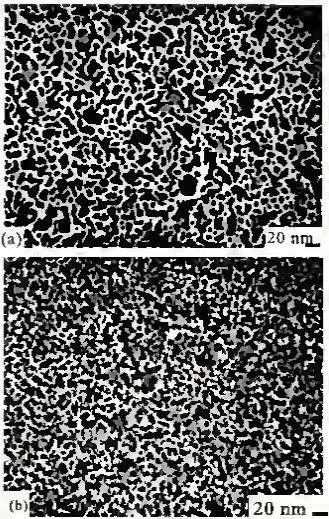

Figure 3.16 Transmission electron micrographs of Ag nano particles collected on carbon -formvar grids at (a) 200 mTorr and (b) 600 mTorr respectively Deposition was carried out with oxygen as the backfill gas

Figure 3.17 Selected area diffraction pattern taken from Ag nano particles deposited on carbon formvar grids showing ring patterns indicative of polycrystalline diffraction behavior

Summary of Experimental Results

In this Chapter the results of nano-particle coatings by pulsed laser ablation onto particulate materials have been presented Several in-situ and analytical techniques were used to observe and characterize the mechanisms of nano particle formation and nano particle coating behavior Many interesting observations from these techniques have shown that the molecular weight and pressure affect both the nano particle formation and core particulate growth mechanisms In the next Chapter discussions of mechanisms for nano particle formation and structural characteristics will be discussed

CHAPTER 4
DISCUSSION

Introduction

The previous chapter has shown that interaction of the laser-induced plume of excited species with an inert or reactive backfill gas controls the energetics of nano particle formation and deposition. Due to the non equilibrium behavior during laser coating ablation synthesis, several factors affect the nano particle formation mechanisms. This section will examine the formation of nano particles during laser ablation with respect to optical spectra, plume expansion characteristics, TEM mesh grids, and core particle structure results.

Optical Spectra

Differences in Ag optical emission intensity with respect to different backfill gases is not obvious from continuous optical spectra measurements presented in Figure 3.6 (a-c). To analyze the optical spectra further, integration of each spectrum was done for each pressure and backfill gas to investigate the relative differences in the amount of excited Ag species present. Each spectrum was then curve fit and the

areas under each of the atomic lines of interest was calculated. Figures 4.1 (a) - (c) correspond to the integration of spectra with respect to wavelengths at 200, 600 and 900 mTorr respectively. From Figures (a) - (c) the laser ablation clearly performed with a backfill gas of argon appears to yield a higher concentration of excited atomic Ag species in the experiments.

Consideration must also be given in the interpretation of this data to the spatial component with respect to the optical emission measurement. It is well known by many researchers that the effects of backfill gases vary both temporally and spatially [Chr94] [Geo98]. The difference in the optical spectra intensity will vary in intensity and location with respect to each gas/ laser ablated sample combination. It is generally expected that the optical emission from ablation into heavier backfill gases will have a higher intensity further from the ablated target due to energy loss through collisional processes [Cha53]. Therefore the observed optical front will move slower for ablation in argon or krypton than it will for ablation in helium or neon, carrying a higher intensity over a longer distance. It is expected from classical physics that the gas collision frequency increases as a function gas pressure and is highest for large atomic diameter, slow-moving gases.

Figures 4.2 (a-e) are calculated plots of the collision frequency as a function of temperature for constant pressures of 200 mTorr, 600 mTorr, 900 mTorr, 100 Torr, and 760 Torr respectively. High pressure calculations were included due to the initial nature of the plume expansion, which has been estimated by researchers [Geo91] [Dye93] [Sin91] to be on the order of hundreds of atmospheres, which results in calculated collision frequencies that are unrealistic for atomic collisions. It is clear from these Figures that the backfill gases will affect both the optical emission and plume expansion characteristics, with the most efficient energy transfer occurring from momentum exchange of gas and plume ablated species of equal mass. These calculated effects are clearly shown in the next section on plume expansion characteristics.

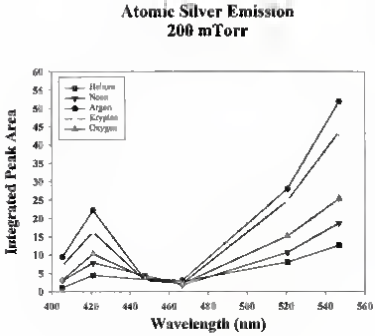

Figure 4 1 Integrated area from optical emiaaion apectra during Ag ablation (a) at 200 mTorr into diffarent backfill ganea aa ahown

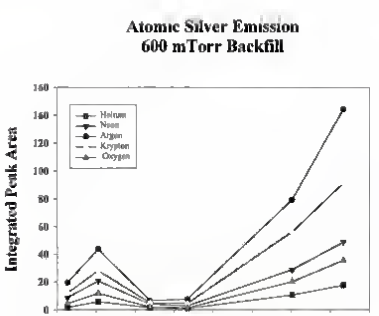

Figure 4.1 continued, Integrated area from optical emission spectra during Ag ablation, (b) at 600 mTorr into different backfill gases as shown.

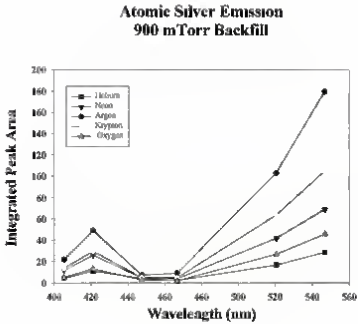

Figure 4 1 continued, Integrated area from optical emission spectra during Ag ablation, (c) at 900 mTorr into different backfill gases as shown

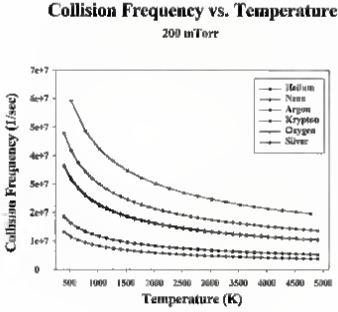

Figure 4 2 Calculated plots of the collision frequency as a function of temperature for a constant pressure, (a) 200 mTorr

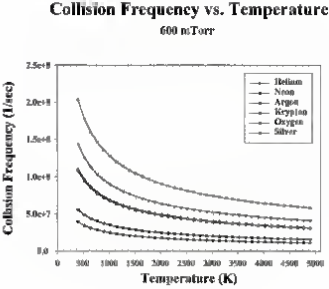

Figure 4.2 continued, Calculated plots of the collision frequency as a function of temperature for a constant pressure, (b) 600 mTorr

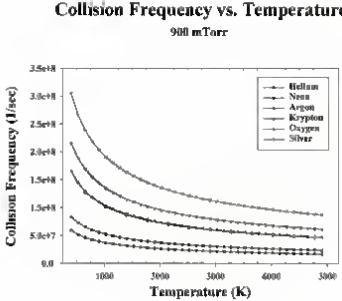

Figure 4.2 continued, Calculated plots of the collision frequency as a function of temperature for a constant pressure, (c) 900 mTorr.

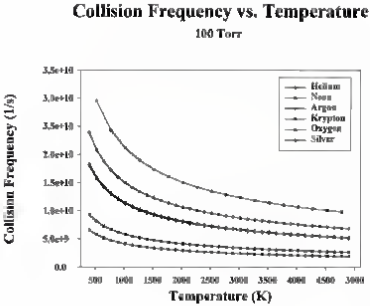

Figure 4.2 continued, Calculated plots of the collision frequency as a function of temperature for a constant pressure, (d) 100 Torr.

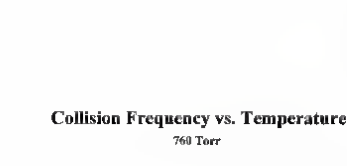

Figure 4.2 continued, Calculated plots of the collision frequency as a function of temperature for a constant pressure, (e) 760 Torr

Plume Expansion Characteristics

The coupling of the 25 nano second excimer laser pulse with a polycrystalline Ag produces an expanding plume of excited Ag species

Plume expansion behavior for Ag ablated in argon has been shown in Figure 3.5-1,2. Further investigations to be presented in this section clearly show the effects of background gas effects both spatially and temporally. Figures 4.3 - 4.7 show the Ag plume expansion in different atmospheres at 20 μsec time increments out to 267 μsec after the initial laser pulse. Please note that Figures 4.3-1, 4.4-1, 4.5-1, 4.6-1, and 4.7.1 are original CCD images obtained. These images have been altered identically as discussed for Figure 3.5-1,2 with grayscale intensity spectra separated into 10 bin regions. The modified Figures highlight the highest intensity portions of the laser ablation plume are shown in Figures 4.3-2, 4.4-2, 4.5-2, 4.6-2, and 4.7-2 for comparison and will be discussed in parallel. Figure 4.3-1,2 show the plume expansion at 30 mTorr purged with helium. From these images it is clear that the detectable optical plume emission has a duration of ≈ 87 μsec after which it becomes undetectable by the CCD imaging system used. These images show that there is little if any plume separation and "back splashing" during the expansion into the vacuum. The plume appears to expand uniformly radially without any hot zones or discontinuities.

Figure 4.4-1,2 show the plume expansion in a helium backfill gas at 200 mTorr. It is clear that the optical emission intensity of the plume has increased significantly due to added gas confinement of the plume and increased collision frequency. However, the expansion behavior in helium is clearly similar to that in a vacuum, an indication that the heavier Ag species are not significantly affected by collisions with the lighter helium atoms. The plume duration times were comparable, with the detectable emission in helium lasting ~10-20 μsec longer as there was a dim image obtained at time (f), 107 μsec, whereas in Figure 4.3-1,2 no emission was observed at time (f). Figures 4.5-1,2 and 4.6-1,2 show the plume expansion in an argon and krypton gas backfills at 200 mTorr. In sharp contrast to the plume expansion in helium, the optical plume emission in both argon and krypton backfills have higher optical emission intensities and the detected emission lasts beyond 300 μsec. Further observations of plume separation and splashing are clearly visible at times Figure 4.5-1,2 (h-k) and in Figure 4.6-1,2 (h-k). This is in comparison to the amount of plume emission observed away from the forward ablation component, which is clearly not visible in vacuum or helium at times > 100 μsec. It is observed in fact that the plume expansions in helium and vacuum appear to have a uniform emission intensity that decays uniformly as shown at times (e-f) in Figures 4.3-1,2 and 4.4-1,2 in contrast to times (h-i) of Figures 4.5-1,2 and 4.6-1,2

Therefore it appears that due to limited interaction with argon and krypton that the Ag plume emission persists for a period beyond 300 μsec that could be arising from spatial heating and temporal confinement of the ablated Ag species. From Fig. 4.5-1,2 and 4.6-1,2 it can be observed from times (h-l) that the brightest secondary emission remains at the same spatial location for ≈100 μsec, which may be approximated as pseudo semi-stationary confined plasma (SSCP) which is slowly interacting with the argon. In comparison with Fig. 4.3-1,2 and 4.4-1,2 this SSCP is not observed in a vacuum or gases of lower atomic mass. In these types of environments, attenuation of the forward radial plume component is not significant in comparison with the time scales observed. It is important further to examine the spatial and temporal behavior of the plume expansion so a plume history was recorded as a function of pressure while at a constant delay time of 147 μsec (or time h in Fig. 4.5-1,2). This means that all images were taken 147 μsec after the laser pulse. Figure 4.7-1,2 shows the expansion behavior from a 30 mTorr vacuum to a 1 Torr argon backfill at a constant delay time. The effects of the argon backfill gas on the optical emission intensity and spatial confinement become clearer. Detectable optical emission is not present from 30-60 mTorr, indicating the differences in plume emission lifetime due to collisional processes leading to spatial confinement as observed at higher pressures of 200 mTorr - 1 Torr respectively.

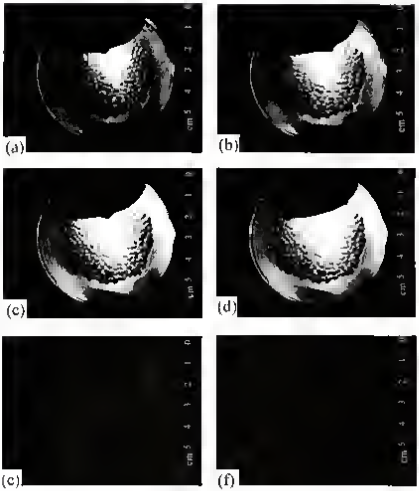

Figure 4.3-1 Time-gated CCD imaging of the optical expansion of the laser plume during Ag ablation at 30 mTorr

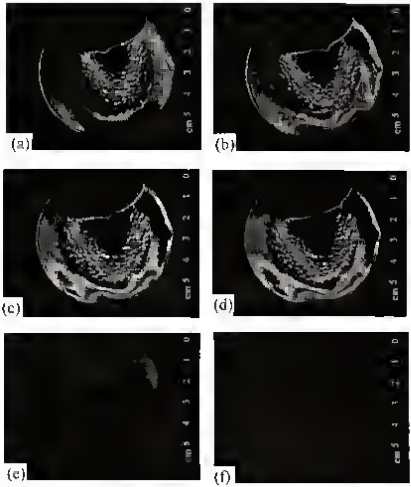

Figure 4.3-2 continued, Time gated CCD imaging of the optical expansion of the laser plume during Ag ablation at 30 mTorr with grayscale intensity spectrum.

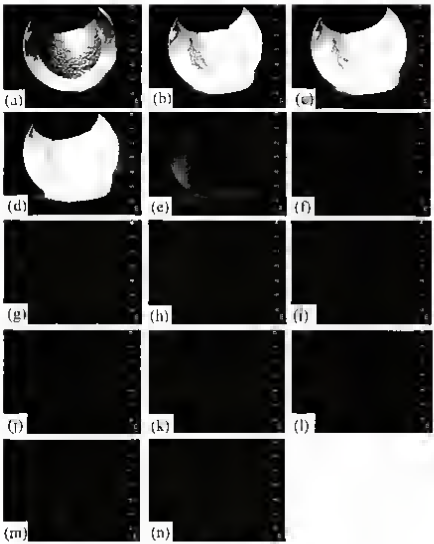

Figure 4.4-1 Time-gated CCD imaging of the optical expansion of the laser plume during Ag ablation into helium at 200 mTorr.

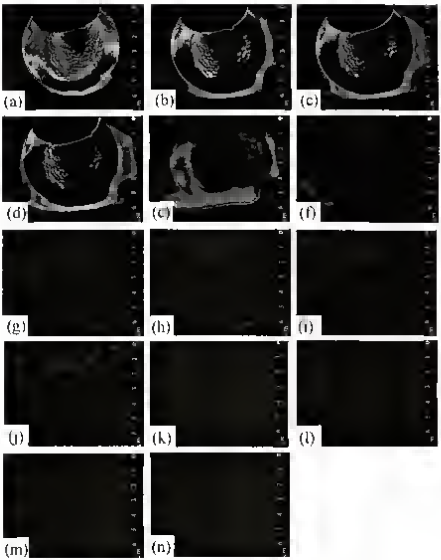

Figure 4 4-2 continued. Time-gated CCD imaging of the optical expansion of the laser plume during Ag ablation into helium at 200 mTorr with grayscale intensity spectrum.

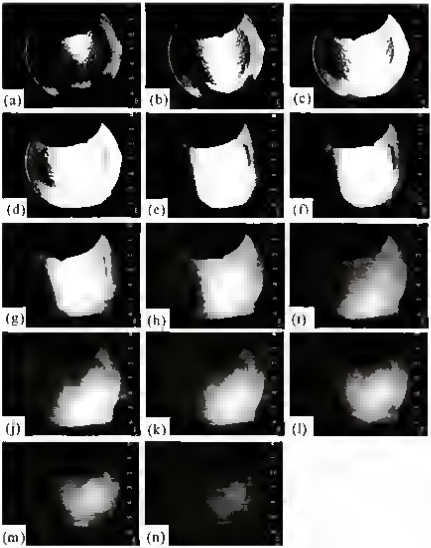

Figure 4.5-1 Time-gated CCD imaging of the optical expansion of the laser plume during Ag ablation into argon at 200 mTorr

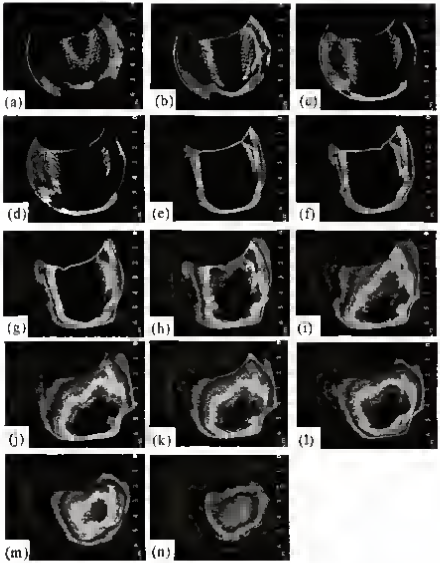

Figure 4.5 2 continued, Time-gated CCD imaging of the optical expansion of the laser plume during Ag ablation into argon at 200 mTorr with grayscale intensity spectrum.

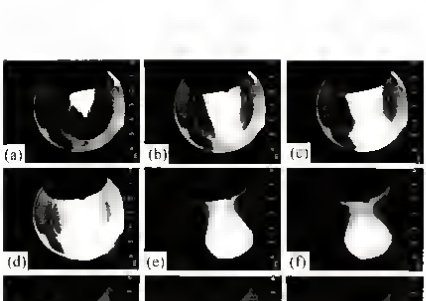

Figure 4.5-1 Time-gated CCD imaging of the optical expansion of the laser plume during Ag ablation into krypton at 200 mTorr. An important observation to note here is that the optical emission appears to have a higher optical emission intensity over a longer time period for ablation into argon than for krypton.

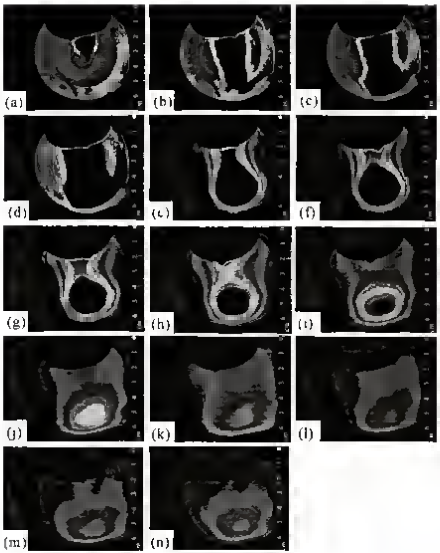

Figure 4-6-2 continued, Time-gated CCD imaging of the optical expansion of the laser plume during Ag ablation into krypton at 200 mTorr with grayscale intensity spectrum. An important observation to note here is that the volume confinement is more pronounced during ablation with a krypton backfill

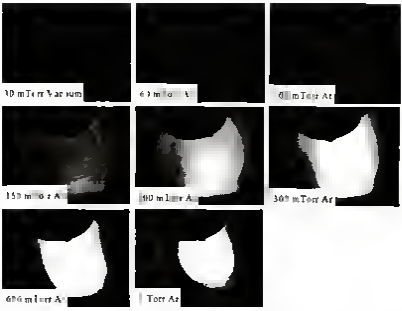

Figure 4.7-1 Time-gated CCD imaging of the optical intensity increase as a function of backfill gas pressure from 30 mTorr to 1 Torr. It is important to note that since all images were taken 147 μsec after the laser pulse, the images show the temporal effects of the backfilled gas on the duration and intensity of the optical emission

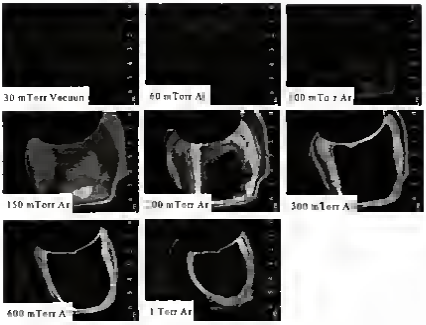

Figure 4 7-2 continued, Time-gated CCD imaging of the optical intensity increase as a function of backfill gas pressure from 30 mTorr to 1 Torr with grayscale intensity spectrum

Nano Particle Formation

It has been shown in the previous section that backfill gases can have significant temporal and spatial effects on the laser plume expansion history. These effects on the mechanism of nano particle formation will now be examined.

From the previous results in Chapter 3, both the nature of the background gas and pressure clearly have significant effects on nano particle size and ion velocities (Figure 3.7). It is clear that in comparison with both the particle sizes obtained by TEM (Figure 3.12-16) and the silver concentration obtained by XPS measurements (Figure 3.11), that the atomic mass and pressure of the backfill gases play an important role in the nano particle growth and deposition kinetics. If the depositions were performed in high or ultra high vacuum, the ablated silver would be atomic in nature and atomic thin films would form on the core particles, but due to the cos^{n} spreading, the containment of the plume would not be efficient and poor coating would result on the core particle substrate [Chr94]. These low deposition rate effects have been seen in conventional pulsed laser deposition of thin films by many researchers [Chr94] [Sin90] [Low96]. If a background gas is introduced during ablation, the deposition kinetics during deposition will be affected as shown in Figures 4.3-4.7. If the gas is of a lower molecular weight in comparison with the ablated species, it is suggested that a low degree of

collisional confinement will be obtained which will result in a narrower nano particle size distribution and a higher mean nano particle transport velocity. As the mass of the backfilled gas is increased the forward radial component of the plume will be slowed as shown in Figures 4.5-1,2. Helium slows the Ag species the least and krypton creates the largest amount of volume confinement as expected from mass considerations. The atomic mass ratios of Ag-backfill gases being discussed are Ag/He is 26.8:1 (107/4), Ag/O_2 is 6.68:1 (107/16), Ag/Ne is 5.35:1 (107/20), Ag/Ar is 2.74:1 (107/39) and Ag/Kr is 1.29:1 (107/83). Figure 4.8 shows the mean nano particle sizes measured from TEM grids as a function of backfill gas and pressure.

The idea of semi-stationary confined plasma (SSCP) will now be re-introduced with respect to nano particle formation mechanisms. As shown in Figures 4.5-1,2, the optical emission persists long after the initial laser pulse is delivered. The optical emission at times (h-n) appears to be stationary with an area of higher intensity in the lower right quadrant. It is proposed that this SSCP, which forms due to collision processes on the front leading radial edge of the plume. These dynamics create a growth volume that can be observed in both time space for up to 362 μsec, after which optical emission is not detectable. Three specific cases for Ag nano particle growth will now be presented, and an overview of the backfill gases used in this research will then be classified

into the three cases. Case 1 as shown in Figure 4.9 (a), represents ablation into a low molecular weight, inert gas. In comparison to a high molecular weight gas, the plume expands freely, nano particles are formed by collisional processes but they do not form multi nano particle agglomerates in flight. The plume does not take on the semi-stationary characteristics of the SSCF such that the SSCF has little or no effect on the nano particle formation over the time period observed. Nano particle size distribution during Ag ablation into a helium backfill is therefore expected to be of single mode. Case 2 as shown in 4.9 (b), represents ablation into a semi heavy molecular weight gas. The plume is visibly confined and the plume front may become stationary for several hundred μsec resulting in SSCF behavior. If the stationary front occurs, a bimodal size distribution of deposited nano particles is expected due to secondary and tertiary nano particle collisions within the growth volume [Geo98]. A significant loss in nano particle velocity is expected and not all particles will reach the core particle substrate. Case 3 as shown in Figure 4.9 (c), represents ablation into a heavy molecular weight gas. The plume is visibly confined and will become semi - stationary at some point in the expansion process, definite observation of the SSCF process is expected. A bimodal and possibly trimodal distribution of nano particles is suggested to form due to the SSCF growth volume. It is also expected that the bimodal and

trimodal nano particle agglomerates formed may fall from the plume during the stationary time period, therefore not reaching the particulate substrate or mesh TEM grid. Collection at the core substrate is not expected to yield a true size distribution due to multiple nano particle agglomeration processes.

Classification of some the experimental gases used will now be presented from observations made by CCD imaging and TEM size analysis. Helium, the lowest molecular weight gas is classified as a case 1. Helium does not attenuate the velocity of Ag ions significantly in comparison to vacuum measurements by other researchers [Geo93] [Chr94]. Optical plume expansion imaging (Fig. 4.4-1,2) showed that the plume is not significantly attenuated in comparison to vacuum imaging, and plume backscatter is not observed. The plume appears to expand through backfill gas to the core particle substrate with little attenuation. Figure 4-10 shows a single mode nano particle size distribution in helium as expected for case 1 growth behavior. Therefore it does not appear that the nano particles once formed in the plume region collide again to form larger particles on the order of 20-30 nm. The primary distribution is at 6 nm. Argon is termed a case 2 gas. From CCD imaging shown in Figures 4.5-1,2 the plume appears to have stationary and backscatter components associated with it indicating SSCP behavior. The plume is visibly confined appears to be stationary for several

microseconds A bimodal size distribution of deposited nano particles was observed as shown in Figures 4 11 4 12 and may be due to the SSCP growth process A significant loss in nano particle velocity is expected Krypton is a heavy gas and is termed a case 3 Ablation into krypton is the most efficient in terms of mass transfer, (ratio = 1 29) and as shown in Figure 4-6-1,2 increases the effects of the SSCP plume volume confinement and optical emission intensity A bimodal and possibly trimodal distribution of nano particles is expected to form, due to the SSCP growth process Nano particles were collected as shown in Figure 4 13, and a single mode distribution was measured It is expected that a single mode nano particle size distribution will be obtained when the nano particles are collected only from one reference location as discussed previously The distribution of larger nano particle agglomerates is thought to have fallen from the plume

The backfilled gas has been shown to have significant effects on the nano particle formation and deposition characteristics The expansion characteristics of the laser-induced plume of excited Ag species change significantly due to collisional confinement and mixing effects The long optical emission lifetime observations made by CCD imaging led to the concept of the semi stationary confined plasma (SSCP) process The effect of the SSCP with respect to the mechanism of nano particle growth behavior in the presence of an

attenuating backfill gas was introduced. The mechanism for nano particle growth and transport with respect to the SSCP can be isolated with respect to both spatial and temporal components as discussed in Figures 4.7.1,2. Keeping with the effects of the nano particle formation and deposition mechanisms presented above, the following section will examine the structural aspects of the Ag nano particle post deposition onto core particulate substrates of Al_2O_3 and SiO_2.

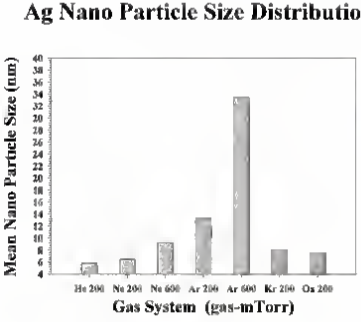

Figure 4.8 Nano particle size distributions collected from TEM grids

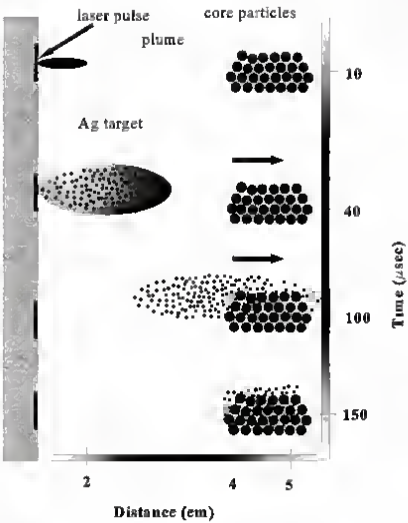

4 9 (a) Ablation into a low molecular weight, inert gas The plume expands freely in comparison to a high molecular weight backfill gas, nano particles are formed by collisional processes but they are not expected to form multi nano particle agglomerates in flight to the core particulates

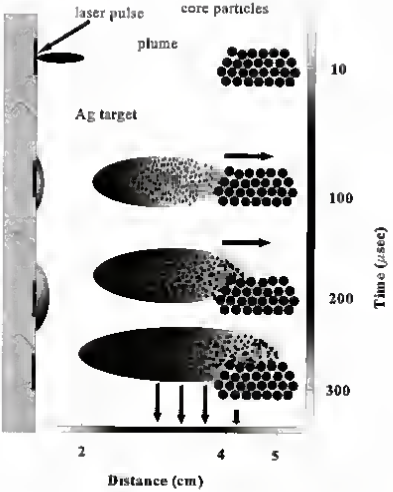

Figure 4 9 continued, (b) Ablation into a semi-heavy molecular weight backfill gas The plume is visibly confined and the plume front may become stationary for several hundred μsec resulting in SSCP behavior If the stationary front occurs, a bimodal size distribution of deposited nano particles is expected due to secondary and tertiary nano particle collisions within the growth volume A significant loss in nano particle velocity is expected and not all particles will reach the core particulate substrates

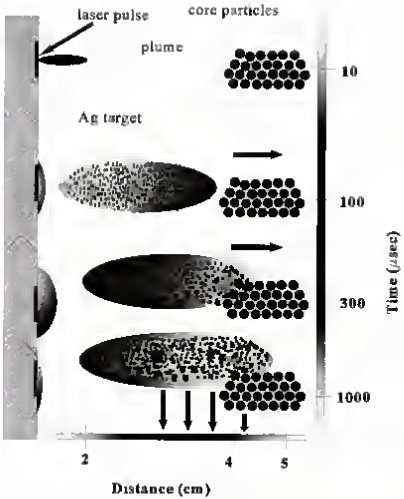

Figure 4 9 continued (c) Ablation into a heavy molecular weight backfill gas The plume is visibly confined and will become semi - stationary at some point in the expansion process, observation of the SSCP process is expected A bimodal and possibly trimodal distribution of nano particles is expected to form due to the SSCP growth volume It is also expected that the bimodal and trimodal nano particle agglomerates formed may fall from the plume during the stationary time period, therefore not reaching the particulate substrate

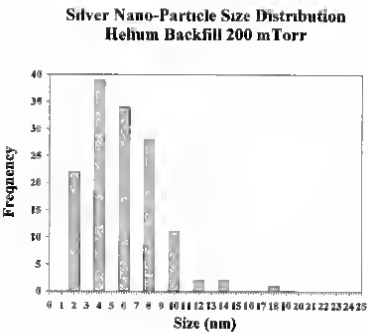

Figure 4.10 Nano particle size distribution in a backfill of helium gas at 200 mTorr. Therefore it does not appear that the nano particles once formed in the plume region collide again to form larger particles on the order of 20-30 nm, but the primary distribution is at 6 nm.

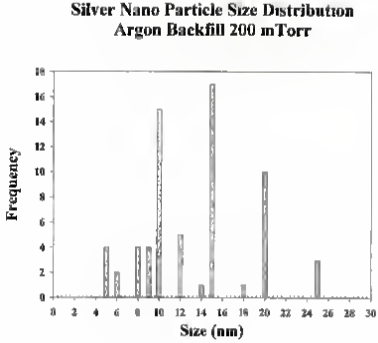

Figure 4.11 Nano particle size distribution during deposition into an argon backfill gas atmosphere at 200 mTorr

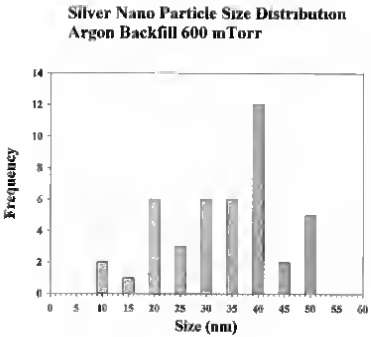

Figure 4 12 Nano particle size distribution during deposition into an argon backfill gas atmosphere at 600 mTorr

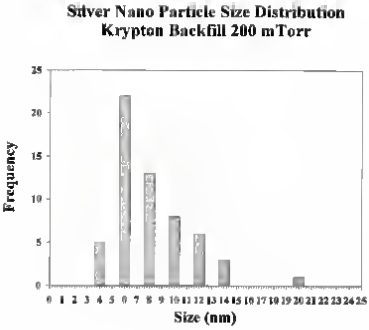
Silver Nano Particle Size Distribution
Krypton Backfill 200 mTorr
Frequency
25
20
15
10
5
0
0 1 2 3 4 5 6 7 8 9 10 11 12 13 14 15 16 17 18 19 20 21 22 23 24 25
Size (nm)

Figure 4.13 Nano particle size distribution during deposition into a krypton backfill gas atmosphere at 200 mTorr

Structural Analysis

In the previous sections the behavior of a laser induced plume intersctions with a backfill gas during ablation of a Ag sputtering target have been examined. The SSCP was proposed to explain the effects of nano particle formation and depositions kinetics. This section will examine the post deposition, structural characteristics of Ag nano particles deposited in an argon backfill onto particulate substrates of Al_2O_3 and SiO_2. Further results from TEM, WDX, AES and STEMZ will be presented in this Chapter, where they were deemed to be most relevant.

Three of the most critical aspects in the area of particulate coatings are the uniformity of the particulate coating, agglomeration of the nano particles, and coating adhesion properties. Due to their high surface area to volume ratios (S/V), nano particle agglomeration during synthesis, transport, handling and coating occurs in all current dry powder coating processes. These size and energetic effects control both the adhesion and the coating deposition stability. The novelty of the present synthesis technique is due to the fact that the nano particle formation and deposition onto core particulate substrate materials occur simultaneously eliminating the effects of self-agglomeration and nano powder handling. It has been found that these three aspects are therefore best fully characterized by both

ensemble and single particle characterization methods

Due to the timescale and temperature of the deposition process (100 μsec — seconds/ pulse, 300 K), combined with effects of a mechanically fluidized substrate as discussed in Chapter 2, uniform coatings are expected The coating concentration is expected to vary as a function of combined effects of the SSCP and time as discussed with respect to Figures 3.11, 4.3.4.7 An ensemble wavelength dispersive x-ray mapping was performed to examine the uniformity of the Ag nano particle coating by elemental mapping techniques Due to the high sensitivity of the technique (ppm), thin, discrete coatings and films can be imaged by elemental mapping techniques. Figure 4.14 shows the result of elemental mapping performed on sample P2C (Ag on Al_2O_3 at 200 mTorr in an argon backfill). Figure 4.14(a) shows a scanning electron micrograph of the Ag coated sample. An elemental Ag map of Figure 4.14(a) is shown in Figure 4.14(b). The elemental map qualitatively shows a clear 1:1 correlation between corresponding Al_2O_3 morphological particle features in 4.14(a) and the x-ray detected scans for Ag shown in 4.14(b) While elemental mapping cannot provide quantitative data on the coating thickness or size of the deposited Ag nano particles, it can show that there appears to be a uniform Ag coating on the surface of the Al_2O_3 particles

Surface depth profiling measurements were performed using AES on single particles prior to TEM to further examine the

coating thickness and discreteness. Figure 4.15 shows an AES depth profile spectra from an Al_2O_3 particle coated with Ag nano particles (sample P2C). There are many observations to be made from the spectra, the most significant is that the spectrum shows that the coating is not continuous over the surface of the Al_2O_3 core particle, which is expected. The Ag signal peaks at close to 100% at the beginning of the profile and then drops to ≈20% after 2 minutes of sputtering. The substrate materials of Al an O are shown to be present throughout the profile, indicating the nature of a discrete coating. The thickness of the coating was approximated to be between 15-30 nm at a sputtering time of 2 minutes at a sputtering rate of 150 Å/min. The significance of the coating indicates a that coating may be only 1-2 Ag nano particles in thickness.

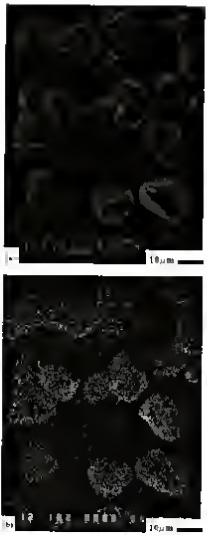

Figure 4.14(a) shows a scanning electron micrograph of the Ag coated sample. An elemental Ag map of Figure 4.14(a) is shown in Figure 4.14(b). The elemental map qualitatively shows a clear 1:1 correlation between corresponding Al_2O_3 morphological particle features in 4.14(a) and the x-ray detected scans for Ag shown in 4.14(b).

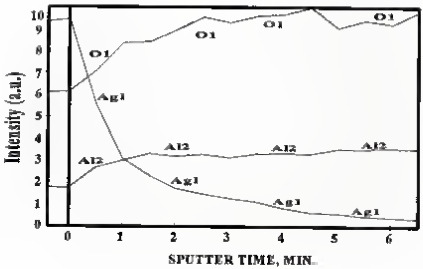

Figure 4 15 Shows s Auger depth profile spectrs from an Al_2O_3 particle coated with Ag nano particles (sample P2C) The spectrum shows that the coating is not continuous over the surface of the Al_2O_3 core particle which is expected The Ag signal peaks at close to 100% at the beginning of the profile and then drops to ≈20% after 2 minutes of sputtering The substrate materials of Al an O sre shown to be present throughout the profile, indicating the nature of s discrete coating The thickness of the coating wss approximated to be between 15-30 nm st s sputtering time of 2 minutes st s sputtering rste of 150 Å/min

Structural Imaging

Further examination with transmission electron microscopy (TEM) was used to obtain hi-resolution images and energy dispersive x-ray (EDX) of Ag nano particle coatings on the surfaces of core Al_2O_3 and SiO_2 surfaces. Figures 4.16 (a,b) show TEM images of Ag nano particle coatings on the surface of SiO_2 core particles (sample PZCS1). Figures 4.16 (c,d) show higher magnification TEM images of the Ag nano particle coating on SiO_2 core particles. From these micrographs the Ag nano particles appear to contain a high concentration of defects, and twin formation, which is characteristic of many FCC metals, in the structure. Figure 4.17 shows an EDX spectrum taken directly on the Ag nano particles at 200,000x. The spectrum further confirms the presence of Ag on the surface of the particle. The Cu and C peaks stem from the fact that the sample is mounted on a C-formvar thin film with a copper mesh support grid. These observations show the Ag nano particle coating is discrete, with a single layer of Ag nano particles around 10-20 nm in size forming the coating, which is in good agreement with AES depth profiling results showing a discrete, 15-30 nm thick coating.

Figures 4 16 gives more credibility to the argument that the Ag nano particles shown on the surfaces of the SiO_2 are formed during gas-collision processes as discussed previously, and not by multiple-pulse laser deposition [Chr94] It is important to note here that instead of a stationary substrate, which is common for most conventional deposition growth processes, the core particulate substrates are constantly agitated as described in Chapter 2 Essentially, there is a new substrate surface exposed to the plume continually during deposition, such that stationary substrate growth effects based on 1,2, and 3-d growth models are not applicable here The combined effects of the particle substrate agitation and the large residence time of the nano particles during deposition suggest that the nano particles point toward complete nano particle growth during flight and subsequent deposition onto the core particulate substrate from single laser pulses These results also agree well with nano particles collected on TEM grids as shown in Figures 3 12 3 16 This can be further understood by a schematic shown in Figure 4 18 The schematic shows what the simplified travel history of a core particle during a typical nano particle deposition may look like The four stages suggest the travel during fluidization of the core particle, noting that nano particle deposition onto the particle is suggested to only occur at stages I and IV

During which the core particle is exposed to the nano particle flux. It can also be inferred from this schematic that secondary agglomeration of nano particles onto existing nano particles that were previously attached to the substrate is probable, an example of this can be observed in Figure 4.16(c). Fig. 4.16(c) shows an agglomerate of 3-4 nano particles agglomerated onto one another. In this micrograph the nano particles, which are 10-12 nm in size, are agglomerated into a 30-40 nm nano particle.

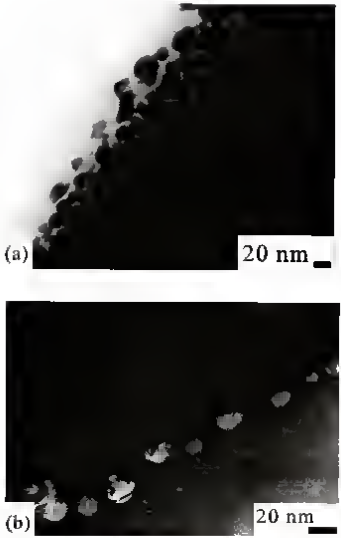

Figures 4 16 (a,b) show transmission electron microscopy (TEM) images of Ag nano particle coatings on the surface of SiO_2 core particles

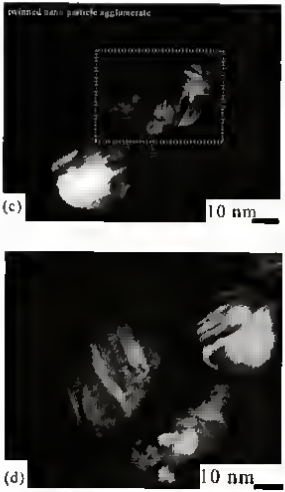

Figures 4 16 (c,d) show higher magnification TEM images of the Ag nano particle coating on SiO_2 core particles. From these micrographs the Ag nano particles appear to contain a high concentration of defects, twin formation, which is characteristic of many FCC metals

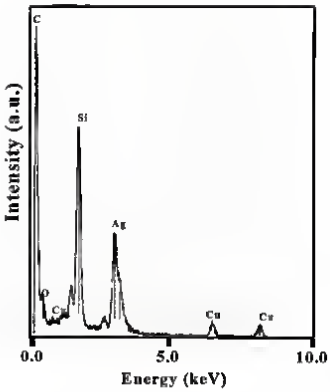

Figure 4.17 Shows a high resolution EDX spectrum taken from the Ag nano particles. The spectrum further confirms the presence of Ag on the surface of the particle

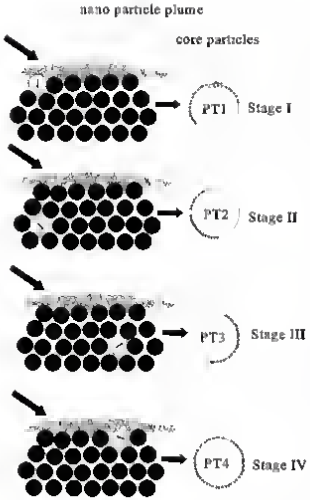

Figure 4 18 This schematic shows what the simplified travel history of a core particle during a typical nano particle deposition may look like The four stages suggest the travel during fluidization of the core particle, noting that nano particle deposition onto the particle is suggested to only occur at stages I and IV, during exposure to the nano particle flux

Crystalline Structure

The effects of pulsed laser deposition into various backfilled gases at different pressures have been discussed with respect to nano particle formation mechanisms. These processes also can influence further effects such as nano particle crystal structure and adhesion behavior. The effects on the kinetic energy on the Ag plume due to interaction with an argon backfill at 200 mTorr can be approximated as a function of the Ag vapor traveling into the backfilled gas. Within Δt = 20 μsec, collisions with the background gas rapidly decelerates the plume of Ag vapor from an initial velocity of ~2 cm/μsec (kinetic energy/atom = 50-100 eV) to ~ 0.01 cm/μsec (~ 0.0015 eV). This may also suggest that a large percentage of the primary Ag nano particles form in the first 20 μsec of the Ag plume expansion, with secondary agglomeration and growth as described by the SSCF process occurring at longer times on the order of hundreds of μsec.

The equilibrium crystal structure of Ag is generally regarded as face centered cubic (FCC) at room temperature [Sch95]. This structure has 4 atoms per unit cell with a coordination number equal to 12. The highest density planes that are the {111} family, are close packed in the <110> directions. Most pure metals form polycrystalline structures. The grains in these structures are small crystals that are on the order of 0.5 -50 μm in size. Metals are unlikely to form

amorphous structures because building blocks are so small (single atoms) that crystallisation is difficult to prevent. Due to the fact that cooling rates in excess of 10^{8} K/s are required for the formation of metallic glasses, the Ag nano particles formed during ablation with cooling rates of $\approx 10^{6}$ K/s are expected to be nanocrystalline due to their lower cooling rates. Scanning transmission electron microscopy (STEM) imaging has confirmed the formation nanocrystalline structures as predicted. Figure 4.19 shows (a) bright field and (b) dark field images of Ag nano particles on an Al_2O_3 core particle (sample P2C). From the dark field image, one can clearly see the bright Ag nano particles attached to the Al_2O_3 core particle substrate. Further high magnification imaging as shown in Figures 4.20, 4.21 show a bright field images of an Ag nano particle on an Al_2O_3 core particle substrate. It is clear from the image that the Ag nano particle has a multiply twinned structure that is commonly found in polycrystalline FCC metals. Figure 4.22 shows the atomic reconstruction of an Ag nano particle. From the image (b) the distances of AB, BC and BD are 0.53 nm, 0.36 nm, and 0.50 nm respectively, in good agreement with previous crystallographic atomic measurements [Lid95].

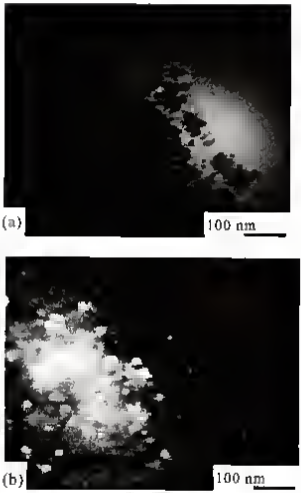

Figure 4 13 shows (a) bright field and (b) dark field images of Ag nano particles on an Al_2O_3 core particle substrate

Figure 4.20 Shows a bright field image of a Ag nano particle on an Al_2O_3 core particle substrate. It is clear from the image that the Ag nano particle has a multiply twinned structure that is commonly found in polycrystalline FCC metals.

Figure 4-21 Shows a bright field image of an Ag nano particle on an Al_2O_3 core particle substrate

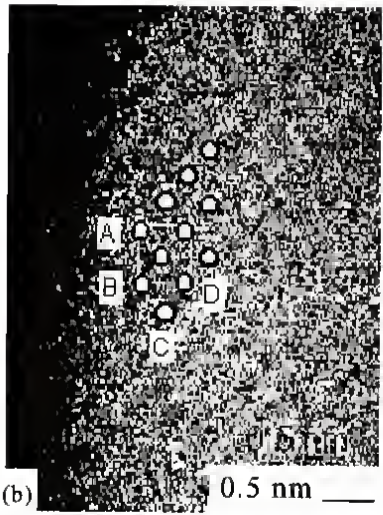

Figure 4.22 Shows the atomic reconstruction of an Ag nano particle (Figure 4.21). From the image (b) the distances of AB, BC, and BD are 0.53 nm, 0.36 nm, and 0.50 nm respectively

Nano Particle Adhesion

Of secondary importance with respect to nano particle formation is nano particle adhesion to the core particle substrate. It is worthwhile to point out a few of the factors that may contribute to particulate adhesion processes [Kru67]. The difficulties encountered in any "physics of adhesion" are due to two things: (1) chemical and nonchemical bond formation and their release at or outside the solid-solid interface; (2) establishment and release of a complex field of mechanical strains and stresses at and around that interface. Adhesion of a particle to a substrate surface involves the following essential steps: 1) at first, particle and substrate come into contact at one point by a contact area of atomic dimensions, 2) by long-range attraction forces between the two, the particle generally is subject to a moment of force so that several contacts are formed, at least between non perfectly smooth adherents, 3) by the interaction forces, the contact area at these contacts increases until the attractive forces and the forces resisting the further deformation at the interface are at equilibrium. An adhesive area of finite size is formed between the adherents. At adhesional equilibrium the attractive forces between the two adherents are balanced by repulsive forces resisting further deformation at their interface [Kru67] [Dah71] [Joh71]. These forces can, usually, not be measured. The attractive interaction forces between

different media include, at least in principal, all those types of interaction that contribute to the cohesion of solids such as metallic, covalent and ionic, i.e., primary, chemical bonds, and secondary van der Waals bonds. The energy of a primary bond is of the order of a few eV, that of a secondary bond about 0.1 eV. In addition there are interaction forces of intermediate energy such as hydrogen bonds, electronic charge transfer bonds and electrostatic double layer forces. A distinction of adhesive forces and their area of application can be classified into three cases. Case 1 represents long range attractive interactions that result from van der Waals forces, electrostatic forces. These forces act not only at the immediate adhesive area, but make important contributions to the overall adhesive force by being of appreciable magnitude also outside the actual adhesive area. Case 2 represents short range attractive interactions resulting from the various types of chemical bonds as mentioned above, and from intermediate bonds such as hydrogen bonds. Case 3 represents interfacial reactions that include sintering effects, diffusion, condensation, diffusive mixing, mutual dissolution and alloying at the interface. It appears that cases 1,3 are of primary importance concerning particle adhesion [Kru67] because they determine the size of the adhesive area whereas contributions from case 2 to the overall adhesive strength can result only if adhesive area of finite size has already been established by interactions of

cases 1,3. At room temperature or below, the interfacial reactions of case 3 are not likely to occur. As a first approximation of the majority of cases of particle - substrate adhesion, case 2 interactions are disregarded because except under extraordinary conditions of purity under, say, ultra high vacuum, primary chemical bonds at surfaces of the still separate adherents will become saturated by contaminating substances, therefore, no longer being available for chemical reactions with the other adherent. Since the experimental system used to synthesize the nano particulate samples was not maintained at a vacuum level even remotely close to an ultra high vacuum (200 mTorr backfill, 30 mTorr base pressure), case 2 contributions with respect to nano particle adhesion to the core particle substrate are not expected to be significant. Also, the probability of the occurrence of a pair of adherents capable of strong primary bond formation according to one or the other of the case 2 interactions is small compared with that of all possible types of potential adherents. This leads to speculation that the Ag nano particle adhesion is mainly due to long range van der Waals and electrostatic forces. Adhesion forces due to van der Waals and electrostatic components were calculated by Hamaker summation methods to be 1.85×10^{-4} Dynes, approximating a spherical Ag nano particle (5 nm in diameter) in contact with a flat surface (Al_2O_3). Due to the obvious difficulties associated with experimentally determining the adhesion strength of nano particles to flat

substrates, experimental comparisons were not obtained. However, because real particles are never completely rigid, and upon coming into contact they deform elastically under the influence of any externally applied loads as well as the attractive inter-surface forces that pull the two surfaces together as shown in Figure 4.23. The contact area was calculated using a theoretical treatment of the adhesion of elastic spheres by Johnson, Kendal, and Roberts et al., known as the JKR theory [Joh71]. Calculated contact area values of ~ 2-3 nm, were in good agreement with experimental measurements taken from Figure 4.16 (c,d).

Throughout all of the experiments deposition of nano particles in helium produced the highest Ag surface concentration that may be due to the premise that during deposition in the heavier gases the nano particles do not reach the core particle substrate in as high a concentration as they do in helium. This is based on the SSCP and agglomeration processes. In accord with this is the comparison with elastic collision data, it has been shown that there is a critical velocity above which particle capture will not occur [Dan71]. Figure 4.24 represents this curve with extrapolation down into the area of nano meter sized particles. This means that for maximum coating efficiency, the velocity of the nano particles in helium (suggest to have maximum velocity during deposition in a helium atmosphere, see Figure 3.7 for wore probe measurements) is below the critical

value for elastic scattering processes and so subsequently are the velocities of the nano particles created in the heavier backfill gases

With the previous discussion in mind, further attempts were made to investigate the nature of the interface between a Ag nano particle and the Al_2O_3 core particle substrate It was hoped that by tilting the sample, atomic resolution observations could be made where the Ag nano particle connects to the substrate Figure 4 25 shows the interface between a Ag nano particle and the core Al_2O_3 particle substrate In Figure 4 25 (a) dark field and (b) bright field images, clearly show the interface with a distinct facet structure, in addition to a sharp transition in lattice dimensions which suggest that there is little intermixing at the interface These observations combined with the deposition conditions, low processing temperature (300 K), and the prediction of nano particle formation in flight provide more support that the adhesion of the nano particles to the core particle substrates is largely due to molecular van der Waals origination as discussed previously

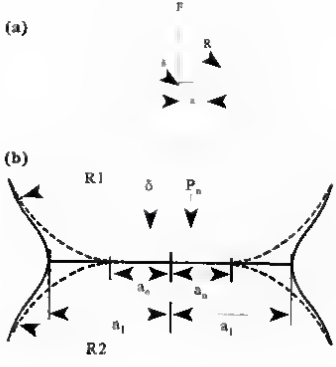

Figure 4 23 (a) Schematic representing the JKR model of adhesion in a particle surface system (b) the contact between two elastic solids both in the presence (contact radius a_1) and absence (contact radius a_o) of surface forces Shown also is the contact between two convex bodies of radii R_1 and R_2 under a normal load of P_n; where δ is the elastic displacement [Joh71]

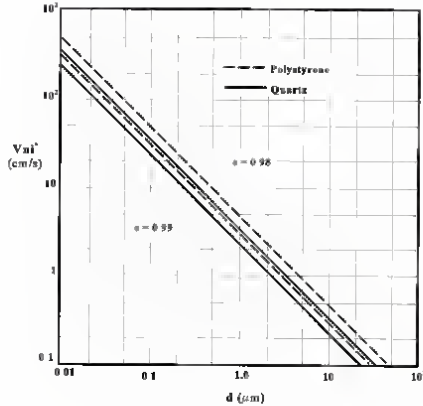

Figure 4 24 Particle capture limits for polystyrene and silica (quartz) spheres colliding with a rigid quartz surface, i e , the surface of a thick body Particle capture occurs when Vni is less than Vni* [Dah71]

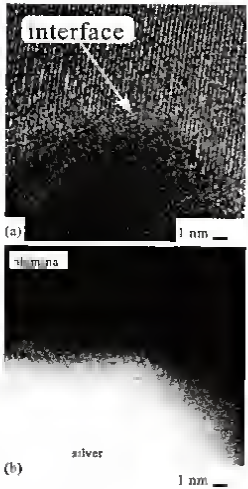

Figure 4.25 Further observations of the interface between the Ag nano particle and the core Al_2O_3 particulate substrate. The interface is clear by both (a) conventional TEM and (b) STEM imaging with z contrast (the bright area corresponds to Ag, the dark area represents the Al_2O_3 substrate)

CHAPTER 5
CONCLUSIONS

A novel new technique to synthesize nano metric coatings on particulate materials using pulsed laser deposition has been investigated. The most significant novelty aspect of the technique that separates it from other dry coating methods arises from the fact that the nano particles are synthesized and deposited onto the core particulate material simultaneously, eliminating deleterious problems associated with agglomeration and handling. By attaching atomic to nano-sized particles either in discrete or continuous form onto the surface of the core particles, i.e., *nano-functionalization of the particulate surface*, materials and products with significantly enhanced properties can be obtained.

In this research silver was used as a target material, while alumina and silica were used as core particle substrate materials. Deposition onto core particulate materials was performed in different gas atmospheres of He, Ne, Ar, Kr and O_2. In-situ analysis by high speed, time gated CCD camera imaging, time gated wire probe velocity measurements, and optical spectroscopy were performed in conjunction with

analytical techniques. Analytical techniques used were scanning electron microscopy (SEM), wavelength dispersive x-ray mapping (WDX), Auger electron spectroscopy (AES), transmission electron microscopy (TEM), scanning transmission electron microscopy with z contrast (STEMZ), and x-ray photoelectron spectroscopy (XPS) were utilized to examine the structural, chemical, and morphological characteristics of the nanostric coatings.

Samples processed in a helium atmosphere produced the highest coating concentration, while samples processed in krypton produced the lowest coating concentration. While the relative measurement of the silver surface concentration is an important measurement, the spatial uniformity of the deposited nano particles on the core particulate surfaces is more significant. Qualitative surface uniformity measurements by WDX mapping techniques showed a high degree of coating uniformity on the core particulate.

Structural TEM and STEMZ imaging showed both continuous and discrete poly-crystalline, multiply twinned nano particle coatings ranging from 5-40 nm in thickness. Further AES depth profiling verified the coating thicknesses to be ~ 25 nm, discrete in nature, meaning that the substrate was continuously detected during depth profiling.

Further investigation by CCD imaging showed critical trends of semi-stationary confined plasma (SSCP) over long time periods (300μsec) in the presence of the heavier

molecular weight backfill gases such as krypton and argon. Nano particles formed are expected to increase in size with respect to the SSCP process due to secondary and tertiary collisions arising from increased in plume confinement and sustained temperature over longer periods of time. Further explanation of the coating concentration can be observed from the SSCP model. As the SSCP becomes more pronounced with the heavier gases (argon, krypton), the nano particle sizes increase and the deposition distance and velocity decrease, ultimately leading to a lower concentration of nano particle species available at the core particulate surface for coating. Further characterisation by wire probe analysis confirmed the velocity profiles of the atomic species relative to the molecular weight of the backfilled gases.

The results from CCD imaging and TEM suggest that the nano particles are formed due to gas phase collisions in flight. Support for the claim of in flight nano particle formation arises from TEM imaging clearly showing spherical nano particles 3-40 nm in diameter attached to core particles of alumina and silica. Since the core particles are in constant agitation (100-150 hz), not stationary as in conventional deposition techniques, new core surfaces are continuously exposed to the nano particle flux. This provokes reasoning that the nano particles are formed by single pulses and deposited onto the core particle not by conventional 2-d, 3-d repetitive growth models [Chr94].

Nano particle size is suggested to vary with respect to gas pressure and molecular weight of the backfill gases in accord with the SSCP effects which confine the plasma and sustain the plume temperature and hence reactivity of the nano particles over a longer time period.

Further research utilizing this technique to solve current industrially viable manufacturing deficiencies has been successfully conducted. Application in the area of flat panel display materials provided a unique and successful method to increase the emission life of sulphide based phosphors materials due to cathodoluminescent degradation [Fit98] Application in the areas of exotic superconducting ($YBa_2Cu_3O_{7-\delta}$) and colossal magnetoresistive ($Pr_{0.65}Ba_{0.35}Ca_{0.3}MnO_3$) coatings on insulating particulate surfaces produced novel particulate materials with unique surface properties previously not synthesized by dry coating techniques [Kum98] [Ata98] [Raj98].

APPENDIX A
NANO PARTICLE CALCULATIONS

First order nano particle calculations were calculated with experimental data from ablation measurements by Mathcad

Nano Particle Coating CalCulations

Volume of Nano Particle

$aoNP := 4.08 \cdot 10^{-8}\,cm$

$volumeNP := \frac{4}{3} \cdot \pi \cdot rNP^3$

$volumeNP = 6.545 \cdot 10^{-20}\,cm^3$

Surface Area of Nano Particle

$rNP := 2.5 \cdot 10^{-7}\,cm$

$SAreaNP := 4 \cdot \pi \cdot rNP^2$

$SAreaNP = 7.854 \cdot 10^{-13}\,cm^2$

Cross Sectional Area

$CSAreaNP := \pi \cdot rNP^2$

$CSAreaNP = 1.963 \cdot 10^{-13}\,cm^2$

Calculation of Nano Particle Mass

$densityNP := 10.5\,\frac{gm}{cm^3}$

Nano Particle Mass

$massNP := volumeNP \cdot densityNP$

$massNP = 6.872 \cdot 10^{-19}\,gm$

Surface Area Per Gram

$SANPPG := \frac{1}{massNP} \cdot SAreaNP$

$SANPPG = 5.143 \cdot 10^{6}\,gm^{-1} \cdot cm^2$

Number of Silver Atoms Per Nano Particle

$NANP := \frac{volumeNP}{(aoNP)^3} \cdot 4$

$NNPPG := \frac{1}{massNP}$

$NANP = 3.855 \cdot 10^{5}$

Number of Nano Particles per Gram

$NNPPG = 1.455 \cdot 10^{18}\,gm^{-1}$

Mass of nano particle

$MNP := \frac{NANP \cdot 107.868\,\frac{gm}{mole}}{6.022 \cdot 10^{23} \cdot \frac{1}{mole}}$

$MNP = 6.905 \cdot 10^{-19}\,gm$

Host Particle Calculations for Volume and Area

Approximating 18 Micron Alumina Particles

Surface Area/Particle

160

rHP $9 \cdot 10^{-4}$ cm

SAHP $4 \cdot \pi \cdot rHP^2$

SAHP = $1.018 \cdot 10^{-5}$ cm^2

Volume/ Particle

VolumeHP $\frac{4}{3} \cdot \pi \cdot rHP^3$

rHP $3 \cdot 10^{-4}$ cm

VolumeHP = $3.054 \cdot 10^{-9}$ cm^3

Particle Mass

VolumeHP = $3.054 \cdot 10^{-9}$ cm^3

densityHP $3.96 \cdot \frac{gm}{cm^3}$

massHP VolumeHP densityHP

massHP = $1.209 \cdot 10^{-8}$ gm

Number of Core Alumina Particles per Gram

NHPPG $\frac{1}{massHP}$

NHPPG = $8.27 \cdot 10^{7}$ gm^{-1}

Core Particle Surface Area Per Gram

SAHPPG $\frac{1}{massHP} \cdot SAHP$

SAHPPG = 841.751 gm^{-1} cm^2

Surface Area To Volume Ratios

Alumina Particles Per Core Particle

SVHP $\frac{SAHP}{VolumeHP}$

SVHP = $3.333 \cdot 10^{3}$ cm^{-1}

Nano Particles Per Nano Particle

SVNP $\frac{SAreaNP}{volumeNP}$

SVNP = $1.2 \cdot 10^{7}$ cm^{-1}

Number of Nano-Particles for Complete Coverage on a Core Particle

$$NNPCC \quad \frac{SAHP}{CSAreaNP}$$

$NNPCC = 5.184 \cdot 10^{7}$

Ablation Depth Atomistic Calculations

1500 Pulses

Volume of 1500 pulse laser crator

$v1500 \quad 2.1 \cdot 10^{-4} \cdot cm^{3}$

$aoNP = 4.08 \cdot 10^{-8} \cdot cm$

Number of atoms per 1500 pulses

$$NNPAPI500vol \quad \frac{v1500}{aoNP^{3}} \cdot 4$$

$NNPAPI500vol = 1.237 \cdot 10^{19}$

Number of atoms ablated per pulse

$$P1500PNPA \quad \frac{NNPAPI500vol}{1500}$$

$P1500PNPA = 8.245 \cdot 10^{15}$

Number of nano particles per pulse

$$NNPI500P \quad \frac{P1500PNPA}{NANP}$$

$NNPI500P = 2.13904 \cdot 10^{12}$

1000 Pulses

Volume of 1000 pulse laser crator

$v1500 \quad 1.2 \cdot 10^{-4} \cdot cm^{3}$

$aoNP = 4.08 \cdot 10^{-8} \cdot cm$

Number of atoms ablated per 1000 pulses

$$NNPAPI000val \quad \frac{v1500}{aoNP^{3}} \cdot 4$$

$NNPAPI000val = 7.067 \cdot 10^{18}$

Number of atoms per pulse

$$P1000PNPA \quad \frac{NNPAP1000vol}{1000}$$

$P1000PNPA = 7.067 \cdot 10^{15}$

Number of nano particles per pulse

$$NNP1000P \quad \frac{P1000PNPA}{NANP}$$

$NNP1000P = 1.03346 \cdot 10^{2}$

300 Pulses

Volume of 300 pulse laser erator

$v300 = 5 \cdot 10^{-5}\ cm^3$

$acNP = 4.08 \cdot 10^{-8} cm$

Number of atoms per 300 pulses

$$NNPAP300vol \quad \frac{v300}{acNP^3} \cdot 4$$

$NNPAP300vol = 2.945 \cdot 10^{18}$

Number of atoms ablated per pulse

$$P300PNPA \quad \frac{NNPAP300vol}{300}$$

$P300PNPA = 9.816 \cdot 10^{15}$

Number of nano particles per pulse

$$NNP300P \quad \frac{P300PNPA}{NANP}$$

$NNP300P = 2.54648 \cdot 10^{12}$

Nano Particle Adhesion Calculations

Contact Area Calculations

Silver - Alumina - Silica Systems

Constants for Alumina, Silica and Silver Used in Calculations

Kalumina $:= 8 \cdot 10^{-13}$

Kalver $:= 4 \cdot 10^{-12}$

$$\text{Keffagal} := \frac{4}{3 \cdot \pi \cdot (\text{Kalumina} - \text{Kalver})}$$

Keffagal = $8.84 \cdot 10^{11}$

Nano Particle radius = Rnp

Rnp $:= 5 \cdot 10^{-9}$

Surface Energy = Wagal

gamagal $:= 500$

gamal $:= 600$
gamag $:= 1500$

Wagal := gamal + gamag - gamagal

Wagal = $1.6 \cdot 10^{3}$

$$\text{nAgAl} := \left(\frac{6 \cdot \pi \cdot \text{Wagal} \cdot \text{Rnp}^2}{\text{Keffagal}}\right)^{\frac{1}{3}}$$

nAgAl = $2.043 \cdot 10^{-8}$

Contact Area for Silver on Silica = aAgSi (nm)

$K_{silver} = 4 \cdot 10^{12}$

$K_{silica} = 4 \cdot 10^{7}$

$Keffagsi = \frac{4}{3 \cdot (K_{silica} - K_{silver})}$

$Keffagsi = 5.32 \cdot 10^{10}$

$Wagsi = 1600$

$aAgsi = \left(\frac{8 \cdot Wagsi \cdot Rnp^2}{Keffagsi} \right)^{\frac{1}{3}}$

$aAgsi = 2.422 \cdot 10^{-8}$

Adhesion Force Calculations for a 5 nm particle of silver, Adhesion Force between Silver nano particle and surface due to size effects = Fadhes1

Hamaker Constant = A

$Aag = 40 \cdot 10^{-13}$ erg

$Rnp1 = 2.5 \cdot 10^{-7}$ cm

H is atomic separation distance

$H = 3 \cdot 10^{-8}$ cm

$Fadhes1 = \frac{Aag \cdot Rnp1}{6 \cdot H^2}$

$Fadhes1 = 1.852 \cdot 10^{-4}$ dyne

Adhesion Force Calculations for a 10 nm particle of silver, Adhesion Force between Silver nano particle and surface due to size effects = Fadhes2

Number of Nano Particles per Gram = NNPPG

$NNPPG = 1.455 \cdot 10^{15} \cdot gm^{-1}$

Number of Silver Atoms Per Nano Particle = NANP

$NANP = 3.855 \cdot 10^{5}$

Mass of Nano Particle = MNP

$MNP = 6.905 \cdot 10^{-19} \cdot gm$

Core Particle Calculations

Surface area of host particle = SAHP

$SAHP = 1.018 \cdot 10^{-5} \cdot cm^{2}$

Volume of core particle

$VolomeHP = 3.054 \cdot 10^{-9} \cdot cm^{3}$

Mass of core particle = massHP

$massHP = 1.209 \cdot 10^{-8} \cdot gm$

Number of core Alumina Particles per Gram = NHPPG

$NHPPG = 8.27 \cdot 10^{7} \cdot gm^{-1}$

Core Particle Surface Area Per Gram = SAHPPG

$SAHPPG = 841.751 \cdot gm^{-1} \cdot cm^{2}$

Surface Area To Volume Ratios

Per Nano Particle = SVNP

$SVNP = 1.2 \cdot 10^{7} \cdot cm^{-1}$

Per Core Particle = SVHP

$SVHP = 3.333 \cdot 10^{3} \cdot cm^{-1}$

Number of Nano-Particles for Complete Coverage on a Core Particle = NNPCC

$$NNPCC \quad \frac{SAHP}{CSAreaNP}$$

$NNPCC = 5.184 \cdot 10^{7}$

Ablation Depth Atomistic Calculations

1500 Pulses

Volume of 1500 pulse laser crator = v1500

v1500 $2.1\ 10^{-4}\ cm^3$

Number of atoms per 1500 pulses = NNPAP1500vol

NNPAP1500vol = $1.237 \cdot 10^{19}$

Number of atoms ablated per pulse = P1500PNPA

P1500PNPA = $8.245 \cdot 10^{15}$

Number of nano particles per pulse = NNP1500P

NNP1000P = $2.13904 \cdot 10^{12}$

1000 Pulses

Volume of 1000 pulse laser crator = v1500

v1000 $1.2 \cdot 10^{-4}\ cm^3$

Number of atoms per 1000 pulses = NNPAP1000vol

NNPAP1000vol = $7.067 \cdot 10^{18}$

Number of atoms ablated per pulse = P1000PNPA

P1000PNPA = $7.067 \cdot 10^{15}$

Number of nano particles per pulse = NNP1000P

NNP1000P = $1.83346 \cdot 10^{12}$

300 Pulses

Volume of 300 pulse laser crator = v3ee

v300 $5\ 10^{-5}\ cm^3$

Number of atoms per 300 pulses = NNPAP300vol

NNPAP300vol = $2.945 \cdot 10^{18}$

Nomber of atoms ablated per pulse = P300PNPA

P300PNPA = $9.816 \cdot 10^{15}$

Number of nano particles per pulse = NNP300P

NNP300P = $2.54848 \cdot 10^{12}$

Aag $40 \cdot 10^{-13}$ erg

Rnp2 $5 \cdot 10^{-7}$ cm

H is atomic separation distance

H $3 \cdot 10^{-8}$ cm

$$Fadhes2 \quad \frac{Aag \cdot Rnp2}{6 \cdot H^2}$$

Fadhes2 = $3.704 \cdot 10^{-4}$ dyne

Particle Calulation Results

Given:

Radius af nano particle = rNP, Radius of host particle = rHP, Density of nano particle = densityNP
Density of core particle = densityHP
aoNP = lattice constant of the nano particle
aoHP = lattice constant of core particle

rNP = $2.5 \cdot 10^{-7}$ cm

rHP = $9 \cdot 10^{-6}$ cm

aoNP = $4.08 \cdot 10^{-8}$ cm

aoHP = $3.8 \cdot 10^{-8}$ cm

densityNP = $10.5 \cdot gm \cdot cm^{-3}$

densityHP = $3.96 \cdot gm \cdot cm^{-3}$

Volume of Nano Particle

volumeNP = $6.545 \cdot 10^{-20} \cdot cm^3$

Surface Area of Nano Particle = SAreaNP

SAreaNP = $7.854 \cdot 10^{-13} \cdot cm^2$

Cross Sectional Area = CSAreaNP

CSAreaNP = $1.963 \cdot 10^{-13} \cdot cm^2$

Nano Particle Mass = massNP

massNP = $6.872 \cdot 10^{-19} \cdot gm$

Surface Area of nano particles per gram = SANPPG

SANPPG = $1.143 \cdot 10^{6} \cdot gm^{-1} \cdot cm^2$

APPENDIX B
X-ray Photoelectron Spectroscopy Data

XPS Analysis of
Silver Coated Alumina

Atomic Weight Gas	Silver Data Atomic Percent		
4	P2A1	9	P6A1	4 4
	P2A2	9 7	P6A2	5.4
20	P2B1	7 32	P6B1	4 9
	P2B2	4 16	P6B2	4 4
39	P2C1	3 71	P6C1	1 9
	P2C2	3	P6C2	3 13
83	P2D1	2 8	P6D1	2.9
	P2D2	3 03	P6D2	2.15

Aluminum Data
Atomic Percent

P2A1	27	P6A1	19
P2A2	31	P6A2	34
P2B1	24	P6B1	24
P2B2	32.9	P6B2	35
P2C1	26	P6C1	27
P2C2	35 14	P6C2	34
P2D1	23	P6D1	29
P2D2	34 4	P6D2	34

Ratio s of Ag/Al

P2A1	33.3333333	P6A1	24 4444444
P2A2	21 5129032	P6A2	15 8823529
P2B1	30 5	P6B1	19 1666666
P2B2	12.7607361	P6B2	12.57142857
P2C1	14.2692307	P6C1	7 03703703
P2C2	8 53727945	P6C2	9.20588235
P2D1	12 6086956	P6D1	9 65517241
P2D2	8 80813953	P6D2	6.32352941

Area
Measurements
from XPS Data

	Silver	Aluminum	Oxygen	Totals	% Concentration Silver
p2a1	354180	80662	451634	886476	39.49040899305545
p2b1	277820	83388	480081	841287	33.02262078181085
p2c1	140981	87033	499115	727129	19.388719195631
p2d1	98199	88825	448910	636734	15.84628628624049
p5a1	121897	46367	387368	564662	21.58764620109
p5b1	168002	77221	482576	727799	23.083571150826
p6c1	71158	81023	454211	656392	10.84077507164O1
p6d1	118978	106193	511604	734775	15.92024769487261

Area
Measurements
from XPS Data

	Silver	Aluminum	Oxygen	Totals	% Concentration Silver
p2a2	375316	153048	641431	1169795	32.084066
p2b2	235925	164372	672300	1073597	22.066336
p2c2	180308	186444	692460	1059210	17.022686
p2d2	169814	181038	731113	1112025	17.069220
p5a2	317402	179217	687198	1183807	27.272735
p5b2	258039	180980	660070	1087089	23.738033
p6c2	179221	172696	671050	1022967	17.519724
p6d2	120655	169841	665491	955990	12.921261

APPENDIX C
Gas Phase Collision Calculation Data

Molecular Masses	gm/mole	Av# atoms/gm mole	Av# atoms/Kg-mole
Helium	4 003	6.02E+23	6 02E+26
Neon	20 179		
Argon	39 948	R (J/Kg*mole*K)	
Krypton	83 8	8 314	
Oxygen	31 998	Kb (J/K)	
Silver	107 868	1.38E-23	

Molecular Diameters	Angstrom	nanometer	meter
Helium	2 18	0.218	2 18E-10
Neon	2.59	0 259	2.59E-10
Argon	3.64	0 364	3.64E-10
Krypton	4 10	0 410	4 10E-10
Oxygen	3 01	0 301	3.01E-10
Silver	4 95	0 495	4.95E-10

Atomic Mass	gm	Kg
Helium	6 647E-24	6 648E 27
Neon	3 350E 23	3 358E-26
Argon	6 633E/23	6 630E/26
Krypton	1 394E 22	1.364E-25
Oxygen	5 313E-23	5.218E-26
Silver	1 778E-22	1 778E-25

Pressure (Torr)	Pressure (Pa)
2.50E-02	3 333
0.05	6.666
0 075	9 999
0 1	13.333
0 125	16 665
0.15	19 998
0 175	23 331
0 2	26.664
0.225	29 997
0.25	33.33
0 275	36 663
0.3	39 996
0.325	43 329

0 35	48 662
0 375	49 995
0.4	53 328
0.425	56.661
0.45	59 994
0 475	63 327
0 5	66.66
0.525	69 993
0.55	73 326
0.575	76 659
6.6	79 992
0.625	83.325
0.65	86 658
0.675	89 991
0.7	93 324
0 725	96 657
0 75	99 99
0 775	103 323
6 6	106.656
0.825	109 989
0 85	113 323
0 875	116.655
0 9	119 988
0 925	123 321
0 95	126.654
0.975	129 987
1	133.32
10	1333 2
100	13332
700	101323.2
7600	1013232
76000	10132320

Temperature (K)	Peak Velocity - Helium	Peak Velocity - Neon	Peak Velocity – Argon
300	1 1162E+03	4 9716E+02	3.5335E+02
325	1 1618E+03	5 1746E+02	3 0777E+02
350	1.2057E+03	5.3700E+02	3 0166E+02

375	1.2480E+03	5.5584E+02	3.9505E+02
400	1.2889E+03	5.7407E+02	4.0801E+02
425	1.3286E+03	5.9174E+02	4.2057E+02
450	1.3671E+03	6.0890E+02	4.3276E+02
475	1.4046E+02	6.2558E+02	4.4462E+02
500	1.4411E+03	6.4183E+02	4.5617E+02
525	1.4766E+03	6.5768E+02	4.6743E+02
550	1.5114E+03	6.7316E+02	4.7843E+02
575	1.5454E+02	6.8829E+02	4.8919E+02
600	1.5786E+02	7.0309E+02	4.9971E+02
625	1.6111E+03	7.1759E+02	5.1001E+02
650	1.6431E+03	7.3180E+03	5.2011E+02
675	1.6744E+03	7.4574E+02	5.3002E+02
700	1.7051E+03	7.5943E+02	5.3975E+02
725	1.7353E+03	7.7287E+02	5.4930E+02
750	1.7649E+03	7.8608E+02	5.5869E+02
775	1.7941E+03	7.9908E+02	5.6793E+02
800	1.8228E+03	8.1189E+02	5.7701E+02
825	1.8511E+03	8.2445E+02	5.8598E+02
850	1.8789E+03	8.3685E+02	5.9477E+02
875	1.9063E+03	8.4907E+02	6.0345E+02
900	1.9334E+02	8.6111E+02	6.1201E+02
925	1.9600E+03	8.7299E+02	6.2046E+02
950	1.9864E+03	8.8471E+02	6.2878E+02
975	2.0123E+03	8.9627E+03	6.3700E+02
1000	2.0380E+03	9.0769E+02	6.4512E+02
1025	2.0633E+03	9.1897E+02	6.5313E+02
1050	2.0883E+03	9.3011E+02	6.6105E+02
1075	2.1130E+03	9.4111E+02	6.6887E+02
1100	2.1374E+03	9.5195E+02	6.7661E+02
1125	2.1910E+03	9.6275E+02	6.8425E+02
1150	2.1855E+03	9.7339E+02	6.9181E+02
1175	2.2091E+03	9.8391E+02	6.9928E+02
1200	2.2325E+03	9.9433E+02	7.0669E+02
1225	2.2556E+03	1.0046E+03	7.1402E+02
1250	2.2785E+03	1.0148E+03	7.2127E+02
1275	2.3012E+03	1.0249E+03	7.2844E+02
1300	2.3236E+03	1.0349E+03	7.3555E+02

1325	2.3459E+03	1.0448E+03	7.4259E+02
1350	2.3879E+03	1.0546E+03	7.4956E+02
1375	2.3897E+03	1.0644E+03	7.5647E+02
1400	2.4113E+03	1.0740E+03	7.6332E+02
1425	2.4328E+03	1.0835E+03	7.7010E+02
1450	2.4540E+03	1.0930E+03	7.7683E+02
1475	2.4751E+03	1.1024E+03	7.8350E+02
1500	2.4960E+03	1.1117E+03	7.9011E+02
1525	2.5167E+03	1.1209E+03	7.9668E+02
1550	2.5372E+03	1.1301E+03	8.0317E+02
1575	2.5578E+03	1.1391E+03	8.0962E+02
1600	2.5778E+03	1.1481E+03	8.1602E+02
1625	2.5979E+03	1.1571E+03	8.2237E+02
1650	2.6178E+03	1.1660E+03	8.2867E+02
1675	2.6378E+03	1.1747E+03	8.3491E+02
1700	2.6572E+03	1.1835E+03	8.4113E+02
1725	2.6760E+03	1.1922E+03	8.4730E+02
1750	2.6960E+03	1.2008E+03	8.5341E+02
1775	2.7152E+03	1.2093E+03	8.5946E+02
1800	2.7342E+03	1.2178E+03	8.6552E+02
1825	2.7531E+03	1.2262E+03	8.7151E+02
1850	2.7719E+03	1.2346E+03	8.7748E+02
1875	2.7906E+03	1.2429E+03	8.8337E+02
1900	2.8091E+03	1.2512E+03	8.8924E+02
1925	2.8278E+03	1.2594E+03	8.9507E+02
1950	2.8459E+03	1.2675E+03	9.0085E+02
1975	2.8640E+03	1.2756E+03	9.0662E+02
2000	2.8821E+03	1.2837E+03	9.1234E+02
2025	2.9001E+03	1.2917E+03	9.1802E+02
2050	2.9179E+03	1.2998E+03	9.2367E+02
2075	2.9356E+03	1.3075E+03	9.2929E+02
2100	2.9533E+03	1.3154E+03	9.3487E+02
2125	2.9708E+03	1.3232E+03	9.4042E+02
2150	2.9882E+03	1.3309E+03	9.4593E+02
2175	3.0056E+03	1.3387E+03	9.5141E+02
2200	3.0228E+03	1.3463E+03	9.5687E+02
2225	3.0399E+03	1.3540E+03	9.6229E+02
2250	3.0560E+03	1.3615E+03	9.6768E+02

2275	3 9739E+03	1 3691E+03	9 7304E+02
2300	3 9907E+03	1.3766E+03	9 7837E+02
2325	3 1075E+03	1 3849E+03	9 8369E+02
2350	3 1241E+03	1 3915E+03	9 8895E+02

MFP Helium 200 mTorr	MFP Helium 600 mTorr	MFP Helium 900 mTorr	MFP Neon 266 mTorr
7.3569E-05	2 4523E-05	1 6348E-05	5.2119E-05
7 9699E-05	2 6566E-05	1 7711E-05	5 6463E-05
8 5829E-05	2.8610E-05	1 9073E-05	6.0800E-05
9 1959E-05	3 0653E-05	2.0435E-05	6 5140E-05
9 8090E-05	3.2697E-05	2 1798E-05	6 9493E-05
1.0422E-04	3.4740E-05	2.3160E-05	7.3826E-05
1 1035E-04	3.6784E-05	2 4523E-05	7 8179E-05
1 1648E-04	3.8827E-05	2 5885E-05	8 2522E-05
1.2261E-04	4 0871E-05	2 7247E-05	8.6866E-05
1 2874E-04	4 2914E-05	2 8610E-05	9 1219E-05
1 3487E-04	4 4958E-05	2 9972E-05	9 5552E-05
1 4100E-04	4 7001E-05	3 1334E-05	9 9899E-05
1 4714E-04	4 9045E-05	3.2697E-05	1 0424E-04
1 5327E-04	5 1089E-05	3.4059E-05	1 0858E-04
1 5940E-04	5.3132E-05	3.5421E-05	1 1293E-04
1.6553E-04	5.5176E-05	3.6784E-05	1 1727E-04
1 7166E-04	5 7219E 05	3 8146E-05	1 2161E-04
1 7779E-04	5 9263E-05	3 9509E-05	1.2590E-04
1 8392E-04	9 1386E-05	4.0871E-05	1.3030E-04
1 9005E-04	6.3350E-05	4.2233E-05	1 3464E-04
1.9618E-04	9.5393E-05	4 3596E-05	1 3899E-04
2.0231E 04	6 7437E-05	4.4958E-05	1.4333E-04
2.0844E-04	6 9480E-05	4 9320E-05	1.4767E-04
2 1457E-04	7 1524E-05	4.7683E-05	1 5202E-04
2 2070E-04	7.3568E-05	4.9045E-05	1 5636E-04
2 2683E-04	7.5911E-05	5 0407E-05	1 6070E-04
2.3296E-04	7 7955E-05	5 1770E-05	1 6504E-04
2 3909E-04	7 9698E-05	5 3132E-05	1 6939E-04
2 4523E-04	8 1742E-05	5 4494E-05	1 7373E-04
2 5136E-04	8 3785E-05	5 5857E-05	1 7807E-04
2.5749E-04	8 5829E-05	5 7219E-05	1 8242E-04
2.9362E-04	8 7872E-05	5 9582E-05	1 8676E-04

2.8975E-04	8.0818E-05	5.9944E-05	1.9110E-04
2.7588E-04	9.1050E-05	8.1306E-05	1.9545E-04
2.8201E-04	9.4003E-05	8.2668E-05	1.9979E-04
2.8814E-04	9.6047E-05	8.4031E-05	2.0413E-04
2.9427E-04	9.8090E-05	8.5393E-05	2.0848E-04
3.0040E-04	1.0013E-04	8.6756E-05	2.1282E-04
3.0653E-04	1.0218E-04	8.8118E-05	2.1718E-04
3.1266E-04	1.0422E-04	8.9480E-05	2.2151E-04
3.1879E-04	1.0626E-04	9.0843E-05	2.2585E-04
3.2492E-04	1.0831E-04	9.2205E-05	2.3019E-04
3.3105E-04	1.1035E-04	9.3568E-05	2.3454E-04
3.3718E-04	1.1239E-04	9.4930E-05	2.3888E-04
3.4332E-04	1.1444E-04	9.6292E-05	2.4322E-04
3.4945E-04	1.1648E-04	9.7655E-05	2.4757E-04
3.5558E-04	1.1853E-04	9.9017E-05	2.5191E-04
3.6171E-04	1.2057E-04	1.0038E-04	2.5625E-04
3.6784E-04	1.2261E-04	1.0174E-04	2.6060E-04
3.7397E-04	1.2466E-04	1.0310E-04	2.6494E-04
3.8010E-04	1.2670E-04	1.0446E-04	2.6928E-04
3.8623E-04	1.2874E-04	1.0583E-04	2.7363E-04
3.9236E-04	1.3078E-04	1.0719E-04	2.7797E-04
3.9849E-04	1.3283E-04	1.0855E-04	2.8231E-04
4.0402E-04	1.3487E-04	1.0991E-04	2.8666E-04
4.1075E-04	1.3692E-04	1.1127E-04	2.9100E-04
4.1688E-04	1.3896E-04	1.1264E-04	2.9534E-04
4.2301E-04	1.4100E-04	1.1400E-04	2.9969E-04
4.2914E-04	1.4305E-04	1.1536E-04	3.0403E-04
4.3527E-04	1.4509E-04	1.1672E-04	3.0837E-04
4.4141E-04	1.4714E-04	1.1809E-04	3.1272E-04
4.4754E-04	1.4918E-04	1.1945E-04	3.1706E-04
4.5367E-04	1.5122E-04	1.2081E-04	3.2140E-04
4.5980E-04	1.5327E-04	1.2218E-04	3.2575E-04
4.6593E-04	1.5531E-04	1.2354E-04	3.3009E-04
4.7206E-04	1.5735E-04	1.2490E-04	3.3443E-04
4.7819E-04	1.5940E-04	1.2628E-04	3.3878E-04
4.8432E-04	1.6144E-04	1.2763E-04	3.4312E-04
4.9045E-04	1.6348E-04	1.2899E-04	3.4748E-04
4.0058E-04	1.6553E-04	1.3035E-04	3.5181E-04

5 0271E-04	1.6757E-04	1 1171E-04	3 5615E-04
5 0884E-04	1.6961E-04	1 1308E-04	3 6049E-04
5 1497E-04	1 7166E-04	1 1446E-04	3 6486E-04
5.2110E-04	1 7370E-04	1 1580E-04	3.6918E-04
5 2723E-04	1 7574E-04	1 1716E-04	3 7352E-04
5.3336E-04	1 7779E-04	1 1853E-04	3 7787E-04
5 3950E-04	1 7983E-04	1 1989E-04	3 8221E-04
5 4563E-04	1 8188E-04	1.2125E-04	3 8655E-04
5 5176E 04	1 8392E-04	1.2261E-04	3 9090E-04
5 5789E-04	1 8596E-04	1 2397E-04	3 9524E-04
5 6402E-04	1 8801E-04	1.2534E-04	3 9958E-04
5 7015E-04	1 9005E-04	1 2670E-04	4 0393E-04
5 7628E-04	1 9209E-04	1.2804E-04	4 0827E-04

MFP Neon 608 mTorr	MFP Neon 800 mTorr	MFP Argon 200 mTorr	MFP Argon 600 mTorr
1 7373E-05	1 1582E-05	2.6387E-05	8 7959E-06
1 8821E-05	1.2547E-05	2 8586E 05	9 5288E-06
2.0269E-05	1.3512E-05	3 0785E-05	1 0262E-05
2 1716E-05	1 4478E-05	3 2984E-05	1 0995E-05
2.3164E-05	1 5443E-05	3 5183E-05	1 1728E-05
2 4612E-05	1 6408E-05	3 7382E-05	1.2461E-05
2 6060E-05	1 7373E-05	3 9581E-05	1.3194E-05
2 7507E-05	1 8338E-05	4 1780E 05	1 3927E-05
2 8955E-05	1 9303E-05	4 3979E 05	1 4660E-05
3 0403E-05	2 0269E-05	4 6178E-05	1.5393E-05
3 1851E-05	2.1234E-05	4.8377E-05	1.6126E-05
3.3299E-05	2.2199E-05	5 0576E-05	1.6859E-05
3.4746E-05	2 3164E-05	5.2775E-05	1 7592E-05
3 6194E-05	2 4129E-05	5 4974E-05	1.8325E-05
3 7642E-05	2.5095E-05	5 7173E-05	1 9058E-05
3.9090E-05	2 6060E-05	5 9372E-05	1 9791E-05
4.0537E-05	2 7025E-05	6 1571E-05	2.0524E05
4 1945E-05	2.7990E-05	6 3770E-05	2 1257E-05
4.3433E-05	2.8955E-05	6 5969E-05	2 1989E-05
4.4881E-05	2 9920E-05	6.8167E-05	2.2722E-05
4 6328E-05	3 0886E-05	7 0366E-05	2.3455E-05
4 7776E-05	3 1851E-05	7.2565E-05	2.4188E-05
4 9224E-05	3.2816E-05	7 4764E-05	2 4921E-05

5.0672E-05	3.3781E-05	7.6963E-05	2.5654E-05
5.2119E-05	3.4746E-05	7.9162E-05	2.6387E-05
5.3567E-05	3.5711E-05	8.1361E-05	2.7128E-05
5.5015E-05	3.6677E-05	8.3560E-05	2.7853E-05
5.6463E-05	3.7642E-05	8.5759E-05	2.8586E-05
5.7910E-05	3.8607E-05	8.7958E-05	2.9319E-05
5.9358E-05	3.9572E-05	9.0157E-05	3.0052E-05
6.0806E-05	4.0537E-05	9.2359E-05	3.0785E-05
6.2254E-05	4.1503E-05	9.4555E-05	3.1518E-05
6.3702E-05	4.2468E-05	9.6754E-05	3.2251E-05
6.5149E-05	4.3433E-05	9.8953E-05	3.2984E-05
6.6597E-05	4.4398E-05	1.0115E-04	3.3717E-05
6.8045E-05	4.5363E-05	1.0335E-04	3.4450E-05
6.9493E-05	4.6328E-05	1.0555E-04	3.5183E-05
7.0940E-05	4.7294E-05	1.0775E-04	3.5916E-05
7.2388E-05	4.8259E-05	1.0995E-04	3.6649E-05
7.3836E-05	4.9224E-05	1.1215E-04	3.7382E-05
7.5284E-05	5.0189E-05	1.1435E-04	3.8115E-05
7.6731E-05	5.1154E-05	1.1654E-04	3.8848E-05
7.8179E-05	5.2119E-05	1.1874E-04	3.9581E-05
7.9627E-05	5.3085E-05	1.2094E-04	4.0314E-05
8.1075E-05	5.4050E-05	1.2314E-04	4.1047E-05
8.2522E-05	5.5015E-05	1.2534E-04	4.1780E-05
8.3970E-05	5.5980E-05	1.2754E-04	4.2513E-05
8.5418E-05	5.6945E-05	1.2974E-04	4.3240E-05
8.6866E-05	5.7910E-05	1.3194E-04	4.3970E-05
8.8314E-05	5.8876E-05	1.3414E-04	4.4712E-05
8.9761E-05	5.9841E-05	1.3633E-04	4.5445E-05
9.1209E-05	6.0806E-05	1.3853E-04	4.6178E-05
9.2657E-05	6.1771E-05	1.4073E-04	4.6911E-05
9.4105E-05	6.2736E-05	1.4293E-04	4.7644E-05
9.5552E-05	6.3702E-05	1.4513E-04	4.8377E-05
9.7000E-05	6.4667E-05	1.4733E-04	4.9110E-05
9.8448E-05	6.5632E-05	1.4953E-04	4.9843E-05
9.9896E-05	6.6597E-05	1.5173E-04	5.0576E-05
1.0134E-04	6.7562E-05	1.5393E-04	5.1309E-05
1.0279E-04	6.8527E-05	1.5613E-04	5.2042E-05
1.0424E-04	6.9493E-05	1.5832E-04	5.2775E-05

1.0569E-04	7.0458E-05	1.6052E-04	5.3508E-05
1.8713E-04	7.1423E-05	1.6272E-04	5.4241E-05
1.8858E-04	7.2388E-05	1.6492E-04	5.4974E-05
1.1003E-04	7.3353E-05	1.6712E-04	5.5707E-05
1.1148E-04	7.4318E-05	1.6932E-04	5.6440E-05
1.1293E-04	7.5284E-05	1.7152E-04	5.7173E-05
1.1437E-04	7.6249E-05	1.7372E-04	5.7906E-05
1.1582E-04	7.7214E-05	1.7592E-04	5.8639E-05
1.1727E-04	7.8179E-05	1.7811E-04	5.9372E-05
1.1872E-04	7.9144E-05	1.8031E-04	6.0105E-05
1.2018E-04	8.0110E-05	1.8251E-04	6.0838E-05
1.2161E-04	8.1075E-05	1.8471E-04	6.1571E-05
1.2306E-04	8.2040E-05	1.8691E-04	6.2304E-05
1.2451E-04	8.3005E-05	1.8911E-04	6.3037E-05
1.2596E-04	8.3970E-05	1.9131E-04	6.3770E-05
1.2740E-04	8.4935E-05	1.9351E-04	6.4503E-05
1.2885E-04	8.5901E-05	1.9571E-04	6.5236E-05
1.3030E-04	8.6866E-05	1.9791E-04	6.5969E-05
1.3175E-04	8.7831E-05	2.0010E-04	6.6701E-05
1.3319E-04	8.8796E-05	2.0230E-04	6.7434E-05
1.3464E-04	8.9761E-05	2.0450E-04	6.8167E-05
1.3609E-04	9.0726E-05	2.0670E-04	6.8900E-05

MFP Argon 900 mTorr	MFP Krypton 200 mTorr	MFP Krypton 600 mTorr	MFP Krypton 900 mTorr
5.8039E-06	2.0203E-05	6.7343E-06	4.4885E-06
6.3525E-06	2.1886E-05	7.2955E-06	4.8036E-06
6.8412E-06	2.3570E-05	7.8507E-06	5.2378E-06
7.3298E-06	2.5254E-05	8.4179E-06	5.6118E-06
7.8185E-06	2.6937E-05	8.9790E-06	5.9800E-06
8.3071E-06	2.8621E-05	9.5402E-06	6.3802E-06
8.7958E-06	3.0304E-05	1.0181E-05	6.7343E-06
9.2845E-06	3.1988E-05	1.0663E-05	7.1084E-06
9.7731E-06	3.3671E-05	1.1224E-05	7.4825E-06
1.0262E-05	3.5355E-05	1.1785E-05	7.8587E-06
1.0750E-05	3.7038E-05	1.2346E-05	8.2308E-06
1.1239E-05	3.8722E-05	1.2907E-05	8.6046E-06
1.1728E-05	4.0406E-05	1.3468E-05	8.9790E-06
1.2216E-05	4.2089E-05	1.4030E-05	9.3532E-06

1.2705E-05	4.3773E-05	1.4591E-05	9.7273E-06
1.3194E-05	4.5456E-05	1.5152E-05	1.0101E-05
1.3682E-05	4.7140E-05	1.5713E-05	1.0476E-05
1.4171E-05	4.8824E-05	1.6275E-05	1.0850E-05
1.4660E-05	5.0507E-05	1.6836E-05	1.1224E-05
1.5148E-05	5.2191E-05	1.7397E-05	1.1598E-05
1.5637E-05	5.3874E-05	1.7958E-05	1.1972E-05
1.6126E-05	5.5558E-05	1.8519E-05	1.2346E-05
1.6614E-05	5.7241E-05	1.9080E-05	1.2720E-05
1.7103E-05	5.8925E-05	1.9642E-05	1.3094E-05
1.7592E-05	6.0609E-05	2.0203E-05	1.3469E-05
1.8080E-05	6.2292E-05	2.0764E-05	1.3843E-05
1.8569E-05	6.3976E-05	2.1325E-05	1.4217E-05
1.9058E-05	6.5659E-05	2.1886E-05	1.4591E-05
1.9546E-05	6.7343E-05	2.2448E-05	1.4965E-05
2.0035E-05	6.9026E-05	2.3009E-05	1.5339E-05
2.0524E-05	7.0710E-05	2.3570E-05	1.5713E-05
2.1012E-05	7.2394E-05	2.4131E-05	1.6087E-05
2.1501E-05	7.4077E-05	2.4692E-05	1.6462E-05
2.1989E-05	7.5761E-05	2.5254E-05	1.6836E-05
2.2478E-05	7.7464E-05	2.5815E-05	1.7210E-05
2.2967E-05	7.9128E-05	2.6376E-05	1.7584E-05
2.3455E-05	8.0811E-05	2.6937E-05	1.7958E-05
2.3944E-05	8.2495E-05	2.7498E-05	1.8332E-05
2.4433E-05	8.4179E-05	2.8060E-05	1.8706E-05
2.4921E-05	8.5862E-05	2.8621E-05	1.9080E-05
2.5410E-05	8.7546E-05	2.9182E-05	1.9455E-05
2.5899E-05	8.9229E-05	2.9743E-05	1.9829E-05
2.6387E-05	9.0913E-05	3.0304E-05	2.0203E-05
2.6876E-05	9.2596E-05	3.0865E-05	2.0577E-05
2.7365E-05	9.4280E-05	3.1427E-05	2.0951E-05
2.7853E-05	9.5964E-05	3.1988E-05	2.1325E-05
2.8342E-05	9.7647E-05	3.2549E-05	2.1699E-05
2.8831E-05	9.9331E-05	3.3110E-05	2.2073E-05
2.9319E-05	1.0101E-04	3.3671E-05	2.2448E-05
2.9808E-05	1.0270E-04	3.4233E-05	2.2822E-05
3.0297E-05	1.0438E-04	3.4794E-05	2.3196E-05
3.0785E-05	1.0606E-04	3.5355E-05	2.3570E-05

3 1274E-05	1 0775E-04	3 5916E-05	2 3944E-05
3 1703E-05	1 0943E-04	3 6477E-05	2 4316E-05
3.2251E-05	1 1112E-04	3 7039E-05	2.4692E-05
3.2740E-05	1 1280E-04	3 7600E-05	2.5067E-05
3 3229E-05	1 1448E-04	3 8161E-05	2 5441E-05
3.3717E-05	1 1617E-04	3 8722E-05	2 5815E-05
3.4206E-05	1 1785E-04	3 9283E-05	2.6189E-05
3 4695E-05	1 1953E-04	3 9845E-05	2.6563E-05
3.5163E-05	1.2122E-04	4 0406E-05	2 6937E-05
3 5672E-05	1 2290E-04	4 0967E-05	2 7311E-05
3 6101E-05	1.2458E 04	4 1526E-05	2.7685E-05
3 6649E-05	1.2027E-04	4 2089E-05	2.8060E-05
3 7138E-05	1.2795E-04	4.2650E-05	2 8434E-05
3 7626E-05	1.2963E-04	4 3212E-05	2.8808E-05
3.8115E-05	1.3132E 04	4 3773E-05	2 9182E-05
3 8604E 05	1 3300E-04	4.4334E-05	2 9556E-05
3 9092E-05	1.3469E 04	4 4895E-05	2.9930E-05
3 9581E-05	1.3637E-04	4 5456E-05	3.0304E-05
4 0070E-05	1.3805E-04	4 6018E-05	3.0678E 05
4 0558E-05	1.3974E-04	4 6579E-05	3 1052E-05
4 1047E-05	1 4142E-04	4 7140E-05	3 1427E-05
4 1536E-05	1 4310E-04	4 7701E-05	3 1801E-05
4.2024E-05	1 4479E-04	4 8262E-05	3 2175E-05
4.2513E-05	1 4647E-04	4 8824E-05	3 2549E-05
4 3002E-05	1 4815E-04	4 9385E-05	3.2923E-05
4.3490E-05	1 4984E-04	4.9946E-05	3.3297E-05
4.3979E-05	1 5152E-04	5 0507E-05	3 3671E-05
4 4468E 05	1.5320E-04	5 1068E-05	3 4046E-05
4 4956E-05	1 5489E-04	5 1630E-05	3.4420E-05
4.5445E-05	1 5657E-04	5.2191E-05	3 4794E-05
4.5934E-05	1 5826E-04	5.2752E-05	3 5168E-05

MFP Oxygen 200 mTorr	MFP Oxygen 600 mTorr	MFP Oxygen 900 mTorr
2 9828E-05	6 9420E-06	5 9817E-06
2 9063E-05	9 6876E-06	6.4565E-06
3 1299E-05	1.0433E-05	9 9554E-06
3 3535E-05	1 1178E-05	7.4522E-06
3 5770E-05	1 1923E-05	7 9490E-06

3.8006E-05	1.2669E-05	8.4458E-06
4.0242E-05	1.3414E-05	8.9426E-06
4.2477E-05	1.4159E-05	9.4394E-06
4.4713E-05	1.4904E-05	9.9362E-06
4.6949E-05	1.5650E-05	1.0433E-05
4.9184E-05	1.6395E-05	1.0930E-05
5.1420E-05	1.7140E-05	1.1427E-05
5.3656E-05	1.7885E-05	1.1923E-05
5.5891E-05	1.8630E-05	1.2420E-05
5.8127E-05	1.9376E-05	1.2917E-05
6.0363E-05	2.0121E-05	1.3414E-05
6.2598E-05	2.0866E-05	1.3911E-05
6.4834E-05	2.1611E-05	1.4408E-05
8.7069E-05	2.2356E-05	1.4904E-05
6.9305E-05	2.3102E-05	1.5401E-05
7.1541E-05	2.3847E-05	1.5898E-05
7.3776E-05	2.4592E-05	1.6395E-05
7.6012E-05	2.5337E-05	1.6892E-05
7.8248E-05	2.6083E-05	1.7388E-05
8.0483E-05	2.6828E-05	1.7885E-05
8.2719E-05	2.7573E-05	1.8382E-05
8.4955E-05	2.8318E-05	1.8879E-05
8.7190E-05	2.9063E-05	1.9376E-05
8.9426E-05	2.9809E-05	1.9872E-05
9.1662E-05	3.0554E-05	2.0369E-05
9.3897E-05	3.1299E-05	2.0866E-05
9.6133E-05	3.2044E-05	2.1363E-05
9.8369E-05	3.2790E-05	2.1860E-05
1.0060E-04	3.3535E-05	2.2356E-05
1.0284E-04	3.4280E-05	2.2853E-05
1.0508E-04	3.5025E-05	2.3350E-05
1.0731E-04	3.5770E-05	2.3847E-05
1.0955E-04	3.6516E-05	2.4344E-05
1.1178E-04	3.7261E-05	2.4841E-05
1.1402E-04	3.8006E-05	2.5337E-05
1.1625E-04	3.8751E-05	2.5834E-05
1.1849E-04	3.9496E-05	2.6331E-05
1.2073E-04	4.0242E-05	2.6828E-05

1.2296E-04	4.0987E-05	2.7325E-05
1.2520E-04	4.1732E-05	2.7821E-05
1.2743E-04	4.2477E-05	2.8318E-05
1.2967E-04	4.3223E-05	2.8815E-05
1.3190E-04	4.3968E-05	2.9312E-05
1.3414E-04	4.4713E-05	2.9809E-05
1.3637E-04	4.5458E-05	3.0305E-05
1.3861E-04	4.6203E-05	3.0802E-05
1.4085E-04	4.6949E-05	3.1299E-05
1.4308E-04	4.7694E-05	3.1796E-05
1.4532E-04	4.8439E-05	3.2293E-05
1.4755E-04	4.9184E-05	3.2790E-05
1.4979E-04	4.9930E-05	3.3286E-05
1.5202E-04	5.0675E-05	3.3783E-05
1.5426E-04	5.1420E-05	3.4280E-05
1.5650E-04	5.2165E-05	3.4777E-05
1.5873E-04	5.2910E-05	3.5274E-05
1.6097E-04	5.3656E-05	3.5770E-05
1.6320E-04	5.4401E-05	3.6267E-05
1.6544E-04	5.5146E-05	3.6764E-05
1.6767E-04	5.5891E-05	3.7261E-05
1.6991E-04	5.6636E-05	3.7758E-05
1.7214E-04	5.7382E-05	3.8254E-05
1.7438E-04	5.8127E-05	3.8751E-05
1.7662E-04	5.8872E-05	3.9248E-05
1.7885E-04	5.9617E-05	3.9745E-05
1.8109E-04	6.0363E-05	4.0242E-05
1.8332E-04	6.1108E-05	4.0738E-05
1.8556E-04	6.1853E-05	4.1235E-05
1.8779E-04	6.2598E-05	4.1732E-05
1.9003E-04	6.3343E-05	4.2229E-05
1.9227E-04	6.4089E-05	4.2726E-05
1.9450E-04	6.4834E-05	4.3223E-05
1.9674E-04	6.5579E-05	4.3719E-05
1.9897E-04	6.6324E-05	4.4216E-05
2.0121E-04	6.7069E-05	4.4713E-05
2.0344E-04	6.7815E-05	4.5210E-05
2.0568E-04	6.8560E-05	4.5707E-05

2.8792E-04	6.9305E-05	4.6203E-05
2.1815E-04	7.0058E-05	4.6700E-05

Helium T/M Ratio	Neon T/M Ratio	Argon T/M Ratio	Krypton T/M Ratio	Oxygen T/M Ratio
6.718E+12	2.892E+12	2.127E+12	1.468E+12	2.376E+12
6.992E+12	3.114E+12	2.213E+12	1.528E+12	2.473E+12
7.256E+12	3.232E+12	2.297E+12	1.586E+12	2.567E+12
7.511E+12	3.345E+12	2.378E+12	1.642E+12	2.657E+12
7.757E+12	3.455E+12	2.456E+12	1.695E+12	2.744E+12
7.996E+12	3.561E+12	2.531E+12	1.748E+12	2.828E+12
8.228E+12	3.665E+12	2.665E+12	1.788E+12	2.810E+12
8.453E+12	3.765E+12	2.676E+12	1.848E+12	2.990E+12
8.673E+12	3.863E+12	2.745E+12	1.856E+12	3.068E+12
8.887E+12	3.958E+12	2.613E+12	1.942E+12	3.143E+12
9.096E+12	4.051E+12	2.679E+12	1.988E+12	3.217E+12
9.301E+12	4.142E+12	2.944E+12	2.033E+12	3.290E+12
9.501E+12	4.232E+12	3.007E+12	2.076E+12	3.360E+12
9.697E+12	4.319E+12	3.069E+12	2.119E+12	3.430E+12
9.889E+12	4.404E+12	3.130E+12	2.161E+12	3.498E+12
1.008E+13	4.488E+12	3.190E+12	2.282E+12	3.564E+12
1.026E+13	4.571E+12	3.248E+12	2.243E+12	3.630E+12
1.044E+13	4.651E+12	3.306E+12	2.283E+12	3.694E+12
1.062E+13	4.731E+12	3.362E+12	2.322E+12	3.757E+12
1.080E+13	4.809E+12	3.418E+12	2.360E+12	3.819E+12
1.097E+13	4.886E+12	3.473E+12	2.398E+12	3.880E+12
1.114E+13	4.962E+12	3.527E+12	2.435E+12	3.940E+12
1.131E+13	5.037E+12	3.580E+12	2.471E+12	4.000E+12
1.147E+13	5.110E+12	3.632E+12	2.508E+12	4.058E+12
1.164E+13	5.183E+12	3.683E+12	2.543E+12	4.116E+12
1.180E+13	5.254E+12	3.734E+12	2.578E+12	4.172E+12
1.195E+13	5.325E+12	3.784E+12	2.613E+12	4.228E+12
1.211E+13	5.394E+12	3.834E+12	2.647E+12	4.284E+12
1.227E+13	5.463E+12	3.883E+12	2.681E+12	4.336E+12
1.242E+13	5.531E+12	3.931E+12	2.714E+12	4.392E+12
1.257E+13	5.598E+12	3.978E+12	2.747E+12	4.445E+12
1.272E+13	5.664E+12	4.026E+12	2.779E+12	4.498E+12
1.286E+13	5.730E+12	4.072E+12	2.812E+12	4.550E+12
1.301E+13	5.794E+12	4.118E+12	2.843E+12	4.601E+12

1.315E+13	5.658E+12	4.164E+12	2.675E+12	4.652E+12
1.330E+13	5.922E+12	4.209E+12	2.906E+12	4.702E+12
1.344E+13	5.984E+12	4.253E+12	2.937E+12	4.752E+12
1.358E+13	6.048E+12	4.297E+12	2.967E+12	4.802E+12
1.371E+13	6.106E+12	4.341E+12	2.997E+12	4.850E+12
1.385E+13	6.168E+12	4.384E+12	3.027E+12	4.899E+12
1.398E+13	6.229E+12	4.427E+12	3.056E+12	4.948E+12
1.412E+13	8.288E+12	4.469E+12	3.086E+12	4.994E+12
1.425E+13	6.347E+12	4.511E+12	3.115E+12	5.041E+12
1.436E+13	6.406E+12	4.553E+12	3.143E+12	5.087E+12
1.451E+13	8.464E+12	4.594E+12	3.172E+12	5.133E+12
1.464E+13	6.521E+12	4.635E+12	3.200E+12	5.179E+12
1.477E+13	8.578E+12	4.875E+12	3.228E+12	5.224E+12
1.490E+13	6.635E+12	4.715E+12	3.256E+12	5.269E+12
1.502E+13	8.691E+12	4.755E+12	3.283E+12	5.313E+12
1.515E+13	6.746E+12	4.795E+12	3.310E+12	5.357E+12
1.527E+13	8.801E+12	4.834E+12	3.337E+12	5.401E+12
1.539E+13	6.858E+12	4.873E+12	3.364E+12	5.444E+12
1.551E+13	6.910E+12	4.911E+12	3.391E+12	5.487E+12
1.564E+13	8.966E+12	4.949E+12	3.417E+12	5.536E+12
1.576E+13	7.017E+12	4.987E+12	3.443E+12	5.573E+13
1.587E+13	7.073E+12	5.025E+12	3.469E+12	5.615E+12
1.599E+13	7.123E+12	5.062E+12	3.495E+12	5.656E+12
1.611E+13	7.175E+12	5.099E+12	3.521E+12	5.698E+12
1.623E+13	7.227E+12	5.138E+12	3.548E+12	5.739E+12
1.634E+13	7.276E+12	5.173E+12	3.571E+12	5.780E+12
1.648E+13	7.329E+12	5.209E+12	3.597E+12	5.826E+12
1.637E+13	7.380E+12	5.245E+12	3.621E+12	5.821E+12
1.668E+13	7.430E+12	5.281E+12	3.648E+12	5.901E+12
1.679E+13	7.480E+12	5.318E+12	3.671E+12	5.943E+12
1.691E+13	7.530E+12	5.352E+12	3.695E+12	5.988E+12
1.702E+13	7.579E+12	5.387E+12	3.719E+12	8.019E+12
1.713E+13	7.628E+12	5.422E+12	3.743E+12	6.056E+12
1.724E+13	7.677E+12	5.458E+12	3.767E+12	8.097E+12
1.735E+13	7.725E+12	5.491E+12	3.791E+12	6.135E+12
1.745E+13	7.774E+12	5.525E+12	3.815E+12	6.173E+12
1.756E+13	7.822E+12	5.559E+12	3.836E+12	8.211E+12
1.767E+13	7.869E+12	5.593E+12	3.862E+12	8.249E+12

1 777E+13	7.918E+12	5 629E+12	3.885E+12	6 287E+12
1 788E+13	7 963E+12	5.660E+12	3 908E+12	6 324E+12
1 798E+13	8.010E+12	5.693E+12	3 931E+12	6 361E+12
1 809E+13	8.057E+12	5 726E+12	3.953E+12	6 398E+12
1 819E+13	8 103E+12	5 759E+12	3 976E+12	6 435E+12
1.830E+13	8 149E+12	5 791E+12	3 999E+12	6.471E+12
1.840E+13	8 104E+12	5.824E+12	4.021E+12	6 507E+12
1 850E+13	8.240E+12	5 856E+12	4 043E+12	6 543E+12
1 860E+13	8.285E+12	5 888E+12	4 065E+12	6 579E+12
1.870E+13	8.330E+12	5 920E+12	4 088E+12	6.615E+12
1 880E+13	8.374E+12	5 852E+12	4 109E+12	6.650E+12

collisions/sec He 200	collisions/sec He 800	collisions/sec He 900	collisions/sec Ne 200
1 517E+07	4.552E+07	6.820E+07	2.142E+07
1 458E+07	4 373E+07	6 580E+07	2.058E+07
1 405E+07	4.214E+07	6.321E+07	1 983E+07
1.357E+07	4.071E+07	6 107E+07	1 916E+07
1 314E+07	3 942E+07	5 913E+07	1 855E+07
1 275E+07	3 824E+07	5 737E+07	1 799E+07
1.239E+07	3 717E+07	5.575E+07	1 749E+07
1.206E+07	3 617E+07	5 426E+07	1 702E+07
1 175E+07	3 526E+07	5.289E+07	1 659E+07
1 147E+07	3 441E+07	5 161E+07	1 619E+07
1 121E+07	3 362E+07	5.043E+07	1 582E+07
1 096E+07	3 288E+07	4 932E+07	1.547E+07
1 073E+07	3.219E+07	4.828E+07	1 514E+07
1 051E+07	3 154E+07	4 730E+07	1 484E+07
1 031E+07	3 092E+07	4 639E+07	1 455E+07
1 012E+07	3 035E+07	4 552E+07	1 428E+07
9 933E+06	2 980E+07	4 470E+07	1.402E+07
9 760E+06	2.928E+07	4.392E+07	1.378E+07
9 596E+06	2.879E+07	4.318E+07	1.355E+07
9 440E+06	2.832E+07	4.248E+07	1 332E+07
9 291E+06	2 787E+07	4 181E+07	1.312E+07
9 150E+06	2 745E+07	4 117E+07	1.291E+07
9 014E+06	2 704E+07	4.058E+07	1.272E+07
8 884E+06	2 665E+07	3 998E+07	1.254E+07
8 760E+06	2.628E+07	3 942E+07	1.237E+07

8.641E+06	2.502E+07	3.858E+07	1.220E+07
8.526E+06	2.558E+07	3.837E+07	1.284E+07
8.416E+06	2.525E+07	3.787E+07	1.188E+07
8.311E+06	2.403E+07	3.740E+07	1.173E+07
8.200E+06	2.463E+07	3.694E+07	1.159E+07
8.110E+06	2.433E+07	3.653E+07	1.145E+07
8.015E+06	2.405E+07	3.607E+07	1.131E+07
7.924E+06	2.377E+07	3.566E+07	1.118E+07
7.835E+06	2.351E+07	3.526E+07	1.106E+07
7.750E+06	2.325E+07	3.487E+07	1.094E+07
7.667E+06	2.300E+07	3.450E+07	1.082E+07
7.586E+06	2.276E+07	3.414E+07	1.071E+07
7.509E+06	2.253E+07	3.378E+07	1.060E+07
7.433E+06	2.230E+07	3.345E+07	1.049E+07
7.360E+06	2.208E+07	3.312E+07	1.039E+07
7.289E+06	2.187E+07	3.280E+07	1.029E+07
7.220E+06	2.166E+07	3.249E+07	1.019E+07
7.153E+06	2.146E+07	3.218E+07	1.010E+07
7.087E+06	2.126E+07	3.189E+07	1.000E+07
7.024E+06	2.107E+07	3.161E+07	9.914E+06
6.962E+06	2.089E+07	3.133E+07	9.827E+06
6.902E+06	2.070E+07	3.106E+07	9.742E+06
6.843E+06	2.053E+07	3.079E+07	9.659E+06
6.786E+06	2.036E+07	3.053E+07	9.578E+06
6.730E+06	2.019E+07	3.028E+07	9.499E+06
6.675E+06	2.003E+07	3.004E+07	9.422E+06
6.622E+06	1.987E+07	2.980E+07	9.347E+06
6.570E+06	1.971E+07	2.957E+07	9.274E+06
6.519E+06	1.956E+07	2.934E+07	9.202E+06
6.470E+06	1.941E+07	2.911E+07	9.132E+06
6.421E+06	1.926E+07	2.889E+07	9.064E+06
6.374E+06	1.912E+07	2.868E+07	8.997E+06
6.328E+06	1.898E+07	2.847E+07	8.931E+06
6.283E+06	1.885E+07	2.827E+07	8.867E+06
6.238E+06	1.871E+07	2.807E+07	8.805E+06
6.194E+06	1.858E+07	2.787E+07	8.743E+06
6.152E+06	1.845E+07	2.768E+07	8.683E+06
6.110E+06	1.833E+07	2.750E+07	8.624E+06

8.069E+06	1.821E+07	2.731E+07	8.567E+06
6.029E+06	1.809E+07	2.713E+07	8.510E+06
5.990E+06	1.797E+07	2.695E+07	8.455E+06
5.951E+06	1.785E+07	2.678E+07	8.400E+06
5.914E+06	1.774E+07	2.661E+07	8.347E+06
5.876E+06	1.763E+07	2.644E+07	8.295E+06
5.840E+06	1.752E+07	2.628E+07	8.243E+06
5.804E+06	1.741E+07	2.612E+07	8.193E+06
5.769E+06	1.731E+07	2.596E+07	8.143E+06
5.735E+06	1.720E+07	2.581E+07	8.095E+06
5.701E+06	1.710E+07	2.565E+07	8.047E+06
5.669E+06	1.700E+07	2.550E+07	8.000E+06
5.635E+06	1.691E+07	2.536E+07	7.954E+06
5.603E+06	1.681E+07	2.521E+07	7.909E+06
5.571E+06	1.671E+07	2.507E+07	7.864E+06
5.540E+06	1.662E+07	2.493E+07	7.820E+06
5.510E+06	1.653E+07	2.479E+07	7.777E+06
5.480E+06	1.644E+07	2.466E+07	7.735E+06
5.450E+06	1.635E+07	2.453E+07	7.693E+06
5.421E+06	1.626E+07	2.440E+07	7.652E+06

collisions/sec Ne 600	collisions/sec Ne 900	collisions/sec Ar 200	collisions/sec Ar 600
8.425E+07	9.638E+07	4.230E+07	1.269E+08
6.173E+07	9.259E+07	4.064E+07	1.219E+08
5.948E+07	8.923E+07	3.918E+07	1.175E+08
5.747E+07	8.623E+07	3.784E+07	1.135E+08
5.564E+07	8.346E+07	3.663E+07	1.099E+08
5.398E+07	8.097E+07	3.554E+07	1.066E+08
5.248E+07	7.869E+07	3.454E+07	1.036E+08
5.108E+07	7.659E+07	3.362E+07	1.009E+08
4.977E+07	7.465E+07	3.277E+07	9.830E+07
4.857E+07	7.285E+07	3.198E+07	9.593E+07
4.745E+07	7.118E+07	3.124E+07	9.373E+07
4.641E+07	6.961E+07	3.056E+07	9.167E+07
4.543E+07	8.815E+07	2.991E+07	8.974E+07
4.451E+07	6.877E+07	2.931E+07	8.792E+07
4.365E+07	6.547E+07	2.874E+07	8.622E+07
4.283E+07	6.425E+07	2.820E+07	8.460E+07

4.286E+07	6.309E+07	2.789E+07	8.308E+07
4.133E+07	6.200E+07	2.721E+07	8.163E+07
4.064E+07	6.095E+07	2.675E+07	8.028E+07
3.997E+07	5.995E+07	2.632E+07	7.896E+07
3.935E+07	5.902E+07	2.590E+07	7.771E+07
3.874E+07	5.812E+07	2.551E+07	7.653E+07
3.817E+07	5.726E+07	2.513E+07	7.539E+07
3.762E+07	5.643E+07	2.477E+07	7.431E+07
3.710E+07	5.564E+07	2.442E+07	7.327E+07
3.659E+07	5.489E+07	2.409E+07	7.227E+07
3.611E+07	5.418E+07	2.377E+07	7.131E+07
3.564E+07	5.348E+07	2.346E+07	7.039E+07
3.519E+07	5.279E+07	2.317E+07	6.951E+07
3.478E+07	5.214E+07	2.289E+07	6.866E+07
3.434E+07	5.152E+07	2.261E+07	6.783E+07
3.394E+07	5.091E+07	2.235E+07	6.704E+07
3.355E+07	5.033E+07	2.209E+07	6.627E+07
3.318E+07	4.977E+07	2.184E+07	6.553E+07
3.282E+07	4.922E+07	2.161E+07	6.482E+07
3.247E+07	4.870E+07	2.137E+07	6.412E+07
3.213E+07	4.819E+07	2.115E+07	6.345E+07
3.180E+07	4.769E+07	2.093E+07	6.280E+07
3.148E+07	4.721E+07	2.072E+07	6.217E+07
3.117E+07	4.675E+07	2.052E+07	6.156E+07
3.086E+07	4.630E+07	2.032E+07	6.096E+07
3.057E+07	4.586E+07	2.013E+07	6.039E+07
3.029E+07	4.543E+07	1.994E+07	5.982E+07
3.001E+07	4.502E+07	1.978E+07	5.928E+07
2.974E+07	4.461E+07	1.958E+07	5.875E+07
2.948E+07	4.422E+07	1.941E+07	5.823E+07
2.922E+07	4.384E+07	1.924E+07	5.772E+07
2.898E+07	4.348E+07	1.908E+07	5.723E+07
2.873E+07	4.310E+07	1.892E+07	5.675E+07
2.850E+07	4.275E+07	1.876E+07	5.629E+07
2.827E+07	4.240E+07	1.861E+07	5.583E+07
2.804E+07	4.206E+07	1.846E+07	5.539E+07
2.782E+07	4.173E+07	1.832E+07	5.495E+07
2.761E+07	4.141E+07	1.818E+07	5.453E+07

2.748E+07	4.109E+07	1.804E+07	5.411E+07
2.719E+07	4.079E+07	1.790E+07	5.371E+07
2.699E+07	4.049E+07	1.777E+07	5.331E+07
2.679E+07	4.019E+07	1.764E+07	5.292E+07
2.660E+07	3.990E+07	1.751E+07	5.254E+07
2.641E+07	3.962E+07	1.739E+07	5.217E+07
2.623E+07	3.935E+07	1.727E+07	5.181E+07
2.605E+07	3.907E+07	1.715E+07	5.145E+07
2.587E+07	3.881E+07	1.703E+07	5.110E+07
2.570E+07	3.855E+07	1.692E+07	5.076E+07
2.553E+07	3.830E+07	1.681E+07	5.043E+07
2.536E+07	3.805E+07	1.670E+07	5.010E+07
2.520E+07	3.780E+07	1.659E+07	4.976E+07
2.504E+07	3.756E+07	1.649E+07	4.948E+07
2.488E+07	3.733E+07	1.638E+07	4.915E+07
2.473E+07	3.710E+07	1.628E+07	4.885E+07
2.458E+07	3.687E+07	1.618E+07	4.855E+07
2.443E+07	3.665E+07	1.608E+07	4.825E+07
2.428E+07	3.643E+07	1.599E+07	4.797E+07
2.414E+07	3.621E+07	1.589E+07	4.766E+07
2.400E+07	3.600E+07	1.580E+07	4.740E+07
2.386E+07	3.579E+07	1.571E+07	4.713E+07
2.373E+07	3.559E+07	1.562E+07	4.686E+07
2.359E+07	3.539E+07	1.553E+07	4.660E+07
2.346E+07	3.519E+07	1.545E+07	4.634E+07
2.333E+07	3.500E+07	1.536E+07	4.608E+07
2.320E+07	3.481E+07	1.528E+07	4.583E+07
2.306E+07	3.462E+07	1.520E+07	4.559E+07
2.298E+07	3.443E+07	1.511E+07	4.534E+07

collisions/sec Ar 900	collisions/sec Kr 200	collisions/sec Kr 600	collisions/sec Kr 900
1.904E+08	5.525E+07	1.658E+08	2.486E+08
1.829E+08	5.308E+07	1.593E+08	2.389E+08
1.762E+08	5.115E+07	1.535E+08	2.302E+08
1.703E+08	4.942E+07	1.483E+08	2.224E+08
1.649E+08	4.785E+07	1.435E+08	2.153E+08
1.599E+08	4.642E+07	1.393E+08	2.089E+08
1.554E+08	4.511E+07	1.353E+08	2.030E+08

1.513E+08	4.301E+07	1.317E+08	1.976E+08
1.475E+08	4.280E+07	1.284E+08	1.926E+08
1.439E+08	4.177E+07	1.253E+08	1.879E+08
1.406E+08	4.081E+07	1.224E+08	1.836E+08
1.375E+08	3.991E+07	1.197E+08	1.795E+08
1.346E+08	3.907E+07	1.172E+08	1.758E+08
1.319E+08	3.828E+07	1.148E+08	1.723E+08
1.293E+08	3.754E+07	1.126E+08	1.689E+08
1.269E+08	3.683E+07	1.105E+08	1.658E+08
1.246E+08	3.617E+07	1.085E+08	1.628E+08
1.225E+08	3.554E+07	1.066E+08	1.599E+08
1.204E+08	3.494E+07	1.048E+08	1.572E+08
1.184E+08	3.438E+07	1.031E+08	1.547E+08
1.166E+08	3.383E+07	1.015E+08	1.523E+08
1.148E+08	3.332E+07	9.995E+07	1.499E+08
1.131E+08	3.282E+07	9.847E+07	1.477E+08
1.115E+08	3.235E+07	9.706E+07	1.456E+08
1.099E+08	3.190E+07	9.573E+07	1.435E+08
1.084E+08	3.147E+07	9.448E+07	1.416E+08
1.070E+08	3.105E+07	9.315E+07	1.397E+08
1.056E+08	3.065E+07	9.194E+07	1.379E+08
1.043E+08	3.026E+07	9.079E+07	1.362E+08
1.030E+08	2.989E+07	8.967E+07	1.345E+08
1.018E+08	2.953E+07	8.860E+07	1.329E+08
1.006E+08	2.919E+07	8.756E+07	1.313E+08
9.941E+07	2.885E+07	8.656E+07	1.298E+08
9.830E+07	2.853E+07	8.560E+07	1.284E+08
9.723E+07	2.822E+07	8.466E+07	1.270E+08
9.619E+07	2.792E+07	8.375E+07	1.256E+08
9.518E+07	2.763E+07	8.288E+07	1.243E+08
9.420E+07	2.734E+07	8.203E+07	1.230E+08
9.326E+07	2.707E+07	8.120E+07	1.218E+08
9.234E+07	2.680E+07	8.040E+07	1.206E+08
9.145E+07	2.654E+07	7.963E+07	1.194E+08
9.058E+07	2.629E+07	7.887E+07	1.183E+08
8.974E+07	2.605E+07	7.814E+07	1.172E+08
8.892E+07	2.581E+07	7.742E+07	1.161E+08
8.812E+07	2.558E+07	7.673E+07	1.151E+08

8 734E+07	2.535E+07	7 605E+07	1 141E+08
8 659E+07	2.513E+07	7 539E+07	1 131E+08
8 585E+07	2 492E+07	7 475E+07	1 121E+08
8.513E+07	2.471E+07	7 413E+07	1 112E+08
8.443E+07	2.451E+07	7.352E+07	1 103E+08
8.375E+07	2.431E+07	7.292E+07	1 094E+08
8.308E+07	2 411E+07	7.234E+07	1 085E+08
8.243E+07	2.392E+07	7 177E+07	1 077E+08
8 179E+07	2.374E+07	7 122E+07	1 068E+08
8 117E+07	2 356E+07	7 068E+07	1 060E+08
8 056E+07	2 338E+07	7 015E+07	1 052E+08
7 997E+07	2.321E+07	6 963E+07	1 044E+08
7 938E+07	2.304E+07	6.912E+07	1 037E+08
7 882E+07	2.288E+07	6 863E+07	1 029E+08
7.826E+07	2.271E+07	6 814E+07	1 022E+08
7 771E+07	2.256E+07	6 767E+07	1 015E+08
7 718E+07	2.240E+07	6 720E+07	1 008E+08
7 666E+07	2.225E+07	6 675E+07	1 001E+08
7.614E+07	2.210E+07	6.630E+07	9 945E+07
7 564E+07	2 195E+07	6 586E+07	9 880E+07
7.515E+07	2 181E+07	6 543E+07	9 815E+07
7.468E+07	2.167E+07	6.501E+07	9 752E+07
7 419E+07	2.153E+07	6.460E+07	9.690E+07
7.373E+07	2 140E+07	6.420E+07	9.629E+07
7.327E+07	2 127E+07	6 380E+07	9 570E+07
7.282E+07	2 114E+07	6.341E+07	9.511E+07
7 238E+07	2.101E+07	6.303E+07	9 454E+07
7 195E+07	2 088E+07	6.265E+07	9 397E+07
7 152E+07	2 076E+07	6.228E+07	9 342E+07
7 111E+07	2 064E+07	6 192E+07	9 287E+07
7 070E+07	2 052E+07	6 156E+07	9 234E+07
7 028E+07	2 040E+07	6 121E+07	9 181E+07
6 990E+07	2.028E+07	6 086E+07	9 130E+07
6 951E+07	2.017E+07	6 052E+07	9 079E+07
6 913E+07	2 006E+07	6 018E+07	9.029E+07
6 875E+07	1 995E+07	5 986E+07	9 980E+07
6.838E+07	1 985E+07	5 954E+07	9 931E+07
6 801E+07	1 974E+07	5 922E+07	9 883E+07

collisions/sec Ox 200	collisions/sec Ox 600	collisions/sec Ox 900
4 161E+07	1.240E+08	1 872E+08
3 998E+07	1 199E+08	1 799E+08
3.852E+07	1 158E+08	1 733E+08
3 721E+07	1 116E+08	1 675E+08
3.603E+07	1 081E+08	1 621E+08
3.496E+07	1 049E+08	1.573E+08
3.397E+07	1 018E+08	1 528E+08
3.307E+07	9 920E+07	1.488E+08
3.223E+07	9 669E+07	1 450E+08
3 145E+07	9.436E+07	1 415E+08
3.073E+07	9.219E+07	1.383E+08
3 005E+07	8 818E+07	1.352E+08
2 942E+07	8 826E+07	1 324E+08
2 883E+07	8.648E+07	1 297E+08
2 827E+07	8 480E+07	1 272E+08
2 774E+07	8.321E+07	1.248E+08
2 724E+07	8 172E+07	1 226E+08
2 678E+07	8.029E+07	1 204E+08
2 631E+07	7 894E+07	1 184E+08
2.589E+07	7 766E+07	1 165E+08
2.548E+07	7 644E+07	1 147E+08
2 509E+07	7 527E+07	1 128E+08
2 472E+07	7.416E+07	1 112E+08
2.438E+07	7 309E+07	1 096E+08
2.402E+07	7.207E+07	1 081E+08
2.370E+07	7 109E+07	1 066E+08
2 338E+07	7 014E+07	1.052E+08
2 308E+07	6 924E+07	1.039E+08
2 279E+07	6 837E+07	1 026E+08
2 251E+07	8 753E+07	1.013E+08
2.224E+07	8.672E+07	1.001E+08
2 198E+07	6 594E+07	9 891E+07
2.173E+07	8 518E+07	9 778E+07
2.149E+07	8 446E+07	8.668E+07
2 125E+07	8 375E+07	9 563E+07
2.102E+07	6 307E+07	8 461E+07

2.080E+07	6.241E+07	9.362E+07
2.059E+07	8.177E+07	9.266E+07
2.038E+07	6.115E+07	9.173E+07
2.018E+07	8.055E+07	9.082E+07
1.999E+07	5.996E+07	8.994E+07
1.980E+07	5.939E+07	8.909E+07
1.961E+07	5.884E+07	8.826E+07
1.943E+07	5.830E+07	8.746E+07
1.926E+07	5.778E+07	8.667E+07
1.909E+07	5.727E+07	8.591E+07
1.893E+07	5.678E+07	8.518E+07
1.876E+07	5.629E+07	8.444E+07
1.861E+07	5.582E+07	8.373E+07
1.845E+07	5.536E+07	8.304E+07
1.830E+07	5.491E+07	8.237E+07
1.816E+07	5.448E+07	8.172E+07
1.802E+07	5.405E+07	8.107E+07
1.788E+07	5.363E+07	8.045E+07
1.774E+07	5.322E+07	7.984E+07
1.761E+07	5.283E+07	7.924E+07
1.748E+07	5.244E+07	7.865E+07
1.735E+07	5.205E+07	7.808E+07
1.723E+07	5.168E+07	7.752E+07
1.711E+07	5.132E+07	7.697E+07
1.699E+07	5.096E+07	7.644E+07
1.687E+07	5.061E+07	7.591E+07
1.676E+07	5.027E+07	7.540E+07
1.664E+07	4.993E+07	7.489E+07
1.653E+07	4.960E+07	7.440E+07
1.643E+07	4.928E+07	7.391E+07
1.632E+07	4.896E+07	7.344E+07
1.622E+07	4.865E+07	7.297E+07
1.611E+07	4.834E+07	7.252E+07
1.601E+07	4.804E+07	7.207E+07
1.592E+07	4.775E+07	7.163E+07
1.582E+07	4.746E+07	7.119E+07
1.573E+07	4.718E+07	7.077E+07
1.563E+07	4.690E+07	7.035E+07

1.554E+07	4.663E+07	6.994E+07
1.545E+07	4.636E+07	6.954E+07
1.536E+07	4.609E+07	6.914E+07
1.528E+07	4.583E+07	6.875E+07
1.519E+07	4.558E+07	6.837E+07
1.511E+07	4.533E+07	6.799E+07
1.503E+07	4.508E+07	6.762E+07
1.495E+07	4.484E+07	6.726E+07
1.487E+07	4.460E+07	6.690E+07

MFP Helium 100 Torr	MFP Helium 760 Torr	MFP Helium 76000 Torr	MFP Neon 100 Torr
1.4714E-07	1.9360E-08	1.9360E-10	1.0424E-07
1.5940E-07	2.0973E-08	2.0973E-10	1.1293E-07
1.7166E-07	2.2587E-08	2.2587E-10	1.2161E-07
1.8392E-07	2.4200E-08	2.4200E-10	1.3030E-07
1.9618E-07	2.5813E-08	2.5813E-10	1.3899E-07
2.0844E-07	2.7427E-08	2.7427E-10	1.4767E-07
2.2070E-07	2.9040E-08	2.9040E-10	1.5636E-07
2.3296E-07	3.0653E-08	3.0653E-10	1.6504E-07
2.4523E-07	3.2266E-08	3.2266E-10	1.7373E-07
2.5749E-07	3.3880E-08	3.3880E-10	1.8242E-07
2.6975E-07	3.5493E-08	3.5493E-10	1.9110E-07
2.8201E-07	3.7106E-08	3.7106E-10	1.9979E-07
2.9427E-07	3.8720E-08	3.8720E-10	2.0848E-07
3.0653E-07	4.0333E-08	4.0333E-10	2.1716E-07
3.1879E-07	4.1946E-08	4.1946E-10	2.2585E-07
3.3105E-07	4.3560E-08	4.3560E-10	2.3454E-07
3.4332E-07	4.5173E-08	4.5173E-10	2.4322E-07
3.5558E-07	4.6786E-08	4.6786E-10	2.5191E-07
3.6784E-07	4.8400E-08	4.8400E-10	2.6060E-07
3.8010E-07	5.0013E-08	5.0013E-10	2.6928E-07
3.9236E-07	5.1626E-08	5.1626E-10	2.7797E-07
4.0462E-07	5.3240E-08	5.3240E-10	2.8666E-07
4.1688E-07	5.4853E-08	5.4853E-10	2.9534E-07
4.2914E-07	5.6466E-08	5.6466E-10	3.0403E-07
4.4141E-07	5.8080E-08	5.8080E-10	3.1272E-07
4.5367E-07	5.9693E-08	5.9693E-10	3.2140E-07
4.6593E-07	6.1306E-08	6.1306E-10	3.3009E-07

4.7819E-07	6.2920E-08	6.2920E-10	3.3870E-07
4.9045E-07	6.4533E-08	6.4533E-10	3.4746E-07
5.0271E-07	6.6146E-08	6.6146E-10	3.5615E-07
5.1497E-07	6.7760E-08	6.7760E-10	3.6484E-07
5.2723E-07	6.9373E-08	6.9373E-10	3.7352E-07
5.3950E-07	7.0986E-08	7.0986E-10	3.8221E-07
5.5176E-07	7.2600E-08	7.2600E-10	3.9090E-07
5.6402E-07	7.4213E-08	7.4213E-10	3.9958E-07
5.7628E-07	7.5826E-08	7.5826E-10	4.0827E-07
5.8854E-07	7.7440E-08	7.7440E-10	4.1696E-07
6.0080E-07	7.9053E-08	7.9053E-10	4.2564E-07
6.1306E-07	8.0666E-08	8.0666E-10	4.3433E-07
6.2532E-07	8.2280E-08	8.2280E-10	4.4302E-07
6.3759E-07	8.3893E-08	8.3893E-10	4.5170E-07
6.4985E-07	8.5506E-08	8.5506E-10	4.6039E-07
6.6211E-07	8.7119E-08	8.7119E-10	4.6908E-07
6.7437E-07	8.8733E-08	8.8733E-10	4.7776E-07
6.8663E-07	9.0346E-08	9.0346E-10	4.8645E-07
6.9889E-07	9.1959E-08	9.1959E-10	4.9513E-07
7.1115E-07	9.3573E-08	9.3573E-10	5.0382E-07
7.2341E-07	9.5186E-08	9.5186E-10	5.1251E-07
7.3568E-07	9.6799E-08	9.6799E-10	5.2119E-07
7.4794E-07	9.8413E-08	9.8413E-10	5.2988E-07
7.6020E-07	1.0003E-07	1.0003E-09	5.3857E-07
7.7246E-07	1.0164E-07	1.0164E-09	5.4725E-07
7.8472E-07	1.0325E-07	1.0325E-09	5.5594E-07
7.9698E-07	1.0487E-07	1.0487E-09	5.6463E-07
8.0924E-07	1.0648E-07	1.0648E-09	5.7331E-07
8.2150E-07	1.0809E-07	1.0809E-09	5.8200E-07
8.3377E-07	1.0971E-07	1.0971E-09	5.9069E-07
8.4603E-07	1.1132E-07	1.1132E-09	5.9937E-07
8.5829E-07	1.1293E-07	1.1293E-09	6.0806E-07
8.7055E-07	1.1455E-07	1.1455E-09	6.1675E-07
8.8281E-07	1.1616E-07	1.1616E-09	6.2543E-07
8.9507E-07	1.1777E-07	1.1777E-09	6.3412E-07
9.0733E-07	1.1939E-07	1.1939E-09	6.4281E-07
9.1959E-07	1.2100E-07	1.2100E-09	6.5149E-07
9.3186E-07	1.2261E-07	1.2261E-09	6.6018E-07

9 4412E-07	1 2423E-07	1.2423E-09	6.6887E-07
9 5038E-07	1 2584E-07	1.2584E-09	6 7755E-07
9 6864E-07	1 2745E-07	1.2745E-09	6 8624E-07
9 8090E-07	1 2907E-07	1.2907E-09	6 9493E-07
9 9316E-07	1 3068E-07	1 3068E-09	7 0361E-07
1 0054E-08	1.3229E-07	1 3229E-09	7.1230E-07
1 0177E-06	1 3391E-07	1 3391E-09	7.2099E-07
1 0299E-06	1 3552E-07	1 3552E-09	7.2967E-07
1 0422E-08	1 3713E-07	1 3713E-09	7.3836E-07
1 0545E-06	1 3875E-07	1 3875E-09	7 4705E-07
1 0667E-06	1 4038E-07	1.4038E-09	7.5573E-07
1 0790E-06	1 4197E-07	1 4197E-09	7.6442E-07
1 0913E-06	1 4359E-07	1 4359E-09	7 7311E-07
1 1035E-06	1 4520E-07	1 4520E-09	7 8179E-07
1 1158E-06	1 4681E-07	1 4681E-09	7 9048E-07
1.1280E-06	1 4843E-07	1.4843E-09	7.9916E-07
1 1403E-06	1 5004E-07	1 5004E-09	8 0785E-07
1 1526E-06	1 5165E-07	1 5165E-09	8 1654E-07

MFP Neon 760 Torr	MFP Neon 76000 Torr	MFP Argon 100 Torr	MFP Argon 760 Torr
1.3710E-08	1 3716E-10	5.2775E-09	6 9441E-09
1 4859E-08	1 4859E-10	5 7173E-08	7 5227E-09
1 6002E-08	1 6002E 10	6.1571E-08	8 1014E-09
1 7145E-08	1 7145E-10	6 5968E-08	8 6801E-09
1 8288E-08	1 8288E-10	7 0360E-09	9.2587E-09
1 9430E-08	1 9430E-10	7 4764E-08	9 8374E-09
2 0573E-08	2.0573E 10	7 9162E-06	1 0416E-08
2 1716E-08	2 1716E-10	8 3560E-08	1 0995E-08
2.2859E-08	2.2859E-10	8 7958E-09	1 1573E-08
2.4002E-08	2.4002E-10	9.2356E-08	1.2152E-09
2 5145E-08	2.5145E 10	9 6754E-08	1.2731E-08
2.6288E-08	2 6288E-10	1.0115E-07	1 3309E-08
2 7431E-08	2.7431E-10	1 0555E-07	1 3888E-06
2.8574E-08	2.8574E 10	1.0995E-07	1 4467E-08
2.9717E-08	2.9717E-10	1 1435E-07	1.5045E-06
3 0860E-08	3 0860E-10	1 1874E-07	1 5624E-08
3 2003E-08	3 2003E 10	1.2314E-07	1 6203E-08
3 3146E-08	3 3146E 10	1.2754E-07	1 6781E-08

3 4289E-08	3 4289E-10	1 3194E-07	1 7360E-08
3 5432E-08	3 5432E-10	1 3633E-07	1 7939E-08
3 6575E-08	3 6575E-10	1 4073E-07	1 8517E-08
3 7718E-08	3 7718E-10	1 4513E-07	1 9096E-08
3 8861E-08	3 8861E-10	1 4953E-07	1 9675E-08
4.0004E-08	4.0004E-10	1 5393E-07	2.0253E-08
4 1147E-08	4 1147E-10	1 5832E-07	2.0832E-08
4.2290E-08	4.2290E-10	1 6272E-07	2 1411E-08
4.3433E-08	4 3433E-10	1 6712E-07	2 1989E 08
4.4576E-08	4 4576E-10	1 7152E-07	2.2568E-08
4 5719E-08	4 5719E 10	1 7592E-07	2.3147E-08
4 6862E-08	4 6862E-10	1 8031E-07	2 3726E-08
4 8005E-08	4.8005E 10	1 8471E-07	2.4304E 08
4 9148E-08	4 9148E-10	1 8911E-07	2 4883E-08
5 0291E-08	5.0291E-10	1 9351E-07	2.5462E-08
5 1434E-08	5 1434E-10	1 9791E-07	2.6040E-08
5 2577E-08	5.2577E 10	2 0230E-07	2 6619E-08
5.3720E-08	5 3720E-10	2 0670E-07	2 7198E-08
5 4863E-08	5 4863E-10	2.1110E-07	2 7776E-08
5.6006E-08	5.6006E-10	2.1550E-07	2.8355E-08
5 7149E-08	5 7149 E 10	2 1989E-07	2 8934E-08
5 8291E-08	5.8291E 10	2 2429E-07	2 9512E-08
5 9434E-08	5 9434E-10	2 2869E-07	3 0091E-08
6.0577E-08	6 0577E-10	2.3309E-07	3 0670E-08
6 1720E-08	6 1720E 10	2 3749E-07	3 1248E-08
6.2863E 08	6.2863E 10	2 4188E-07	3 1827E-08
6 4006E-08	6 4006E 10	2 4628E-07	3 2406E-08
6 5149E-08	6 5149E-10	2 5068E-07	3 2984E-08
6.6292E-08	6 6292E-10	2.5508E-07	3.3563E-08
6 7435E-08	6 7435E-10	2 5948E-07	3.4142E-08
6.8578E 08	6 8578E-10	2 6387E-07	3.4720E-08
6 9721E-08	6 9721E-10	2.6827E-07	3 5299E-08
7.0864E-08	7 0864E-10	2 7267E-07	3 5878E-08
7.2007E-08	7 2007E 10	2 7707E-07	3 6456E-08
7 3150E-08	7 3150E-10	2 8147E-07	3 7035E-08
7 4293E-08	7 4293E-10	2.8586E-07	3 7614E-08
7 5436E-08	7 5436E-10	2 9026E-07	3 8192E-08
7 6579E-08	7 6579E 10	2 9466E-07	3 8771E-08

7.7722E-08	7.7722E-10	2.9906E-07	3.9350E-08
7.8865E-08	7.8885E-10	3.0346E-07	3.9928E-08
8.0008E-08	8.0008E-10	3.0785E-07	4.0507E-08
8.1151E-08	8.1151E-10	3.1225E-07	4.1086E-08
8.2294E-08	8.2294E-10	3.1665E-07	4.1664E-08
8.3437E-08	8.3437E-10	3.2105E-07	4.2243E-08
8.4580E-08	8.4580E-10	3.2544E-07	4.2822E-08
8.5723E-08	8.5723E-10	3.2984E-07	4.3400E-08
8.6866E-08	8.6866E-10	3.3424E-07	4.3979E-08
8.8009E-08	8.8009E-10	3.3864E-07	4.4558E-08
8.9152E-08	8.9152E-10	3.4304E-07	4.5138E-08
9.0295E-08	9.0295E-10	3.4743E-07	4.5715E-08
9.1438E-08	9.1438E-10	3.5183E-07	4.6294E-08
9.2581E-08	9.2581E-10	3.5623E-07	4.6872E-08
9.3724E-08	9.3724E-10	3.6063E-07	4.7451E-08
9.4867E-08	9.4867E-10	3.6503E-07	4.8030E-08
9.6010E-08	9.6010E-10	3.6942E-07	4.8608E-08
9.7152E-08	9.7152E-10	3.7382E-07	4.9187E-08
9.8295E-08	9.8295E-10	3.7822E-07	4.9766E-08
9.9438E-08	9.9438E-10	3.8262E-07	5.0344E-08
1.0058E-07	1.0058E-09	3.8702E-07	5.0923E-08
1.0172E-07	1.0172E-09	3.9141E-07	5.1502E-08
1.0287E-07	1.0287E-09	3.9581E-07	5.2080E-08
1.0401E-07	1.0401E-09	4.0021E-07	5.2659E-08
1.0515E-07	1.0515E-09	4.0461E-07	5.3238E-08
1.0630E-07	1.0630E-09	4.0900E-07	5.3816E-08
1.0744E-07	1.0744E-09	4.1340E-07	5.4395E-08

MFP Argon 76000 Torr	MFP Krypton 100 Torr	MFP Krypton 760 Torr	MFP Krypton 76000 Torr
8.9441E-11	4.0408E-08	5.3165E-09	5.3165E-11
7.5227E-11	4.3773E-08	5.7596E-06	5.7598E-11
8.1014E-11	4.7140E-08	6.2028E-09	6.2028E-11
8.6801E-11	5.0507E-08	6.6457E-09	6.6457E-11
9.2587E-11	5.3874E-08	7.0887E-09	7.0887E-11
9.8374E-11	5.7241E-08	7.5318E-09	7.5318E-11
1.0416E-10	6.0609E-08	7.9748E-06	7.9748E-11
1.0995E-10	6.3978E-08	8.4179E-09	8.4179E-11
1.1573E-10	6.7345E-08	8.8609E-09	8.8609E-11

1.2152E-10	7.0710E-08	9.3039E-09	8.3038E-11
1.2731E-10	7.4077E-08	9.7470E-09	8.7470E-11
1.3309E-10	7.7444E-08	1.0190E-08	1.0190E-10
1.3888E-10	8.0811E-08	1.0633E-08	1.0633E-10
1.4467E-10	8.4179E-08	1.1076E-08	1.1076E-10
1.5045E-10	8.7546E-08	1.1519E-08	1.1519E-10
1.5624E-10	9.0913E-08	1.1962E-08	1.1962E-10
1.6203E-10	9.4280E-08	1.2405E-08	1.2405E-10
1.6781E-10	9.7647E-08	1.2848E-08	1.2848E-10
1.7360E-10	1.0101E-07	1.3291E-08	1.3281E-10
1.7939E-10	1.0438E-07	1.3734E-08	1.3734E-10
1.8517E-10	1.0775E-07	1.4177E-08	1.4177E-10
1.9096E-10	1.1112E-07	1.4620E-08	1.4820E-10
1.9675E-10	1.1448E-07	1.5064E-08	1.5064E-10
2.0253E-10	1.1785E-07	1.5507E-08	1.5507E-10
2.0832E-10	1.2122E-07	1.5950E-08	1.5950E-10
2.1411E-10	1.2458E-07	1.6393E-08	1.6383E-10
2.1989E-10	1.2795E-07	1.6836E-08	1.6836E-10
2.2568E-10	1.3132E-07	1.7279E-08	1.7279E-10
2.3147E-10	1.3469E-07	1.7722E-08	1.7722E-10
2.3726E-10	1.3805E-07	1.8165E-08	1.8165E-10
2.4304E-10	1.4142E-07	1.8608E-08	1.8608E-10
2.4883E-10	1.4479E-07	1.9051E-08	1.9051E-10
2.5462E-10	1.4815E-07	1.9494E-08	1.9494E-10
2.6040E-10	1.5152E-07	1.9937E-08	1.9937E-10
2.6619E-10	1.5489E-07	2.0380E-08	2.0380E-10
2.7198E-10	1.5826E-07	2.0823E-08	2.0823E-10
2.7776E-10	1.6162E-07	2.1266E-08	2.1266E-10
2.8355E-10	1.6499E-07	2.1709E-08	2.1709E-10
2.8934E-10	1.6836E-07	2.2152E-08	2.2152E-10
2.9512E-10	1.7172E-07	2.2595E-08	2.2595E-10
3.0091E-10	1.7509E-07	2.3038E-08	2.3038E-10
3.0670E-10	1.7846E-07	2.3481E-08	2.3481E-10
3.1248E-10	1.8183E-07	2.3924E-08	2.3924E-10
3.1827E-10	1.8519E-07	2.4367E-08	2.4367E-10
3.2406E-10	1.8856E-07	2.4811E-08	2.4811E-10
3.2984E-10	1.9193E-07	2.5254E-08	2.5254E-10
3.3563E-10	1.9529E-07	2.5697E-08	2.5697E-10

3.4142E-10	1.9866E-07	2.6140E-08	2.6140E-10
3.4720E-10	2.0203E-07	2.6583E-08	2.6583E-10
3.5299E-10	2.0540E-07	2.7026E-08	2.7026E-10
3.5878E-10	2.0876E-07	2.7469E-08	2.7469E-10
3.6456E-10	2.1213E-07	2.7912E-08	2.7912E-10
3.7035E-10	2.1550E-07	2.8355E-08	2.8355E-10
3.7614E-10	2.1886E-07	2.8798E-08	2.8798E-10
3.8192E-10	2.2223E-07	2.9241E-08	2.9241E-10
3.8771E-10	2.2560E-07	2.9684E-08	2.9684E-10
3.9350E-10	2.2897E-07	3.0127E-08	3.0127E-10
3.9928E-10	2.3233E-07	3.0570E-08	3.0570E-10
4.0507E-10	2.3570E-07	3.1013E-08	3.1013E-10
4.1086E-10	2.3907E-07	3.1456E-08	3.1456E-10
4.1664E-10	2.4243E-07	3.1899E-08	3.1899E-10
4.2243E-10	2.4580E-07	3.2342E-08	3.2342E-10
4.2822E-10	2.4917E-07	3.2785E-08	3.2785E-10
4.3400E-10	2.5254E-07	3.3228E-08	3.3228E-10
4.3979E-10	2.5590E-07	3.3671E-08	3.3671E-10
4.4558E-10	2.5927E-07	3.4114E-08	3.4114E-10
4.5136E-10	2.6264E-07	3.4558E-08	3.4558E-10
4.5715E-10	2.6600E-07	3.5001E-08	3.5001E-10
4.6294E-10	2.6937E-07	3.5444E-08	3.5444E-10
4.6872E-10	2.7274E-07	3.5887E-08	3.5887E-10
4.7451E-10	2.7611E-07	3.6330E-08	3.6330E-10
4.8030E-10	2.7947E-07	3.6773E-08	3.6773E-10
4.8608E-10	2.8284E-07	3.7216E-08	3.7216E-10
4.9187E-10	2.8621E-07	3.7659E-08	3.7659E-10
4.9766E-10	2.8957E-07	3.8102E-08	3.8102E-10
5.0344E-10	2.9294E-07	3.8545E-08	3.8545E-10
5.0923E-10	2.9631E-07	3.8988E-08	3.8988E-10
5.1502E-10	2.9968E-07	3.9431E-08	3.9431E-10
5.2080E-10	3.0304E-07	3.9874E-08	3.9874E-10
5.2659E-10	3.0641E-07	4.0317E-08	4.0317E-10
5.3238E-10	3.0978E-07	4.0760E-08	4.0760E-10
5.3816E-10	3.1314E-07	4.1203E-08	4.1203E-10
5.4395E-10	3.1651E-07	4.1646E-08	4.1646E-10

MFP Oxygen 100 Torr	MFP Oxygen 760 Torr	MFP Oxygen 76000 Torr
5.3656E-08	7.0599E-09	7.0599E-11
5.8127E-08	7.6403E-09	7.6403E-11
6.2598E-08	8.2366E-09	8.2366E-11
6.7069E-08	8.8249E-09	8.8249E-11
7.1541E-08	9.4133E-09	9.4133E-11
7.6012E-08	1.0002E-08	1.0002E-10
8.0483E-08	1.0590E-08	1.0590E-10
8.4955E-08	1.1178E-08	1.1178E-10
8.9426E-08	1.1767E-08	1.1767E-10
9.3897E-08	1.2355E-08	1.2355E-10
9.8369E-08	1.2943E-08	1.2943E-10
1.0284E-07	1.3532E-08	1.3532E-10
1.0731E-07	1.4120E-08	1.4120E-10
1.1178E-07	1.4708E-08	1.4708E-10
1.1625E-07	1.5297E-08	1.5297E-10
1.2073E-07	1.5885E-08	1.5885E-10
1.2520E-07	1.6473E-08	1.6473E-10
1.2967E-07	1.7062E-08	1.7062E-10
1.3414E-07	1.7650E-08	1.7650E-10
1.3861E-07	1.8238E-08	1.8238E-10
1.4308E-07	1.8827E-08	1.8827E-10
1.4755E-07	1.9415E-08	1.9415E-10
1.5202E-07	2.0003E-08	2.0003E-10
1.5650E-07	2.0592E-08	2.0592E-10
1.6097E-07	2.1180E-08	2.1180E-10
1.6544E-07	2.1768E-08	2.1768E-10
1.6991E-07	2.2356E-08	2.2356E-10
1.7438E-07	2.2945E-08	2.2945E-10
1.7885E-07	2.3533E-08	2.3533E-10
1.8332E-07	2.4121E-08	2.4121E-10
1.8779E-07	2.4710E-08	2.4710E-10
1.9227E-07	2.5298E-08	2.5298E-10
1.9674E-07	2.5886E-08	2.5886E-10
2.0121E-07	2.6475E-08	2.6475E-10
2.0568E-07	2.7063E-08	2.7063E-10
2.1015E-07	2.7651E-08	2.7651E-10
2.1462E-07	2.8240E-08	2.8240E-10

2.1909E-07	2.8828E-08	2.8828E-10
2.2356E-07	2.9416E-08	2.9416E-10
2.2804E-07	3.0005E-08	3.0005E-10
2.3251E-07	3.0593E-08	3.0593E-10
2.3698E-07	3.1181E-08	3.1181E-10
2.4145E-07	3.1770E-08	3.1770E-10
2.4592E-07	3.2358E-08	3.2358E-10
2.5039E-07	3.2946E-08	3.2946E-10
2.5486E-07	3.3535E-08	3.3535E-10
2.5934E-07	3.4123E-08	3.4123E-10
2.6381E-07	3.4711E-08	3.4711E-10
2.6828E-07	3.5300E-08	3.5300E-10
2.7275E-07	3.5888E-08	3.5888E-10
2.7722E-07	3.6476E-08	3.6476E-10
2.8169E-07	3.7065E-08	3.7065E-10
2.8616E-07	3.7653E-08	3.7653E-10
2.9063E-07	3.8241E-08	3.8241E-10
2.9511E-07	3.8830E-08	3.8830E-10
2.9958E-07	3.9418E-08	3.9418E-10
3.0405E-07	4.0006E-08	4.0006E-10
3.0852E-07	4.0595E-08	4.0595E-10
3.1299E-07	4.1183E-08	4.1183E-10
3.1746E-07	4.1771E-08	4.1771E-10
3.2193E-07	4.2360E-08	4.2360E-10
3.2640E-07	4.2948E-08	4.2948E-10
3.3088E-07	4.3536E-08	4.3536E-10
3.3535E-07	4.4125E-08	4.4125E-10
3.3982E-07	4.4713E-08	4.4713E-10
3.4429E-07	4.5301E-08	4.5301E-10
3.4876E-07	4.5890E-08	4.5890E-10
3.5323E-07	4.6478E-08	4.6478E-10
3.5770E-07	4.7066E-08	4.7066E-10
3.6218E-07	4.7655E-08	4.7655E-10
3.6665E-07	4.8243E-08	4.8243E-10
3.7112E-07	4.8831E-08	4.8831E-10
3.7559E-07	4.9420E-08	4.9420E-10
3.8006E-07	5.0008E-08	5.0008E-10
3.8453E-07	5.0596E-08	5.0596E-10

3.8900E-07	5.1185E-08	5.1185E-10
3.9347E-07	5.1773E-08	5.1773E-10
3.9795E-07	5.2361E-08	5.2361E-10
4.0242E-07	5.2950E-08	5.2950E-10
4.0689E-07	5.3538E-08	5.3538E-10
4.1136E-07	5.4126E-08	5.4126E-10
4.1583E-07	5.4715E-08	5.4715E-10
4.2030E-07	5.5303E-08	5.5303E-10

APPENDIX D
Laser Interactions with Materials Calculations

Properties of Experimental Materials

Target Material	Host Particle Material	Host Particle Size Range
Ag	Al_2O_3	1 $R_\mu m$

Optical Material	Energy	N	K	R(0=0)	Abs.Coeff(cm^{-1})	Depth (cm)
Ag	5eV	1 55	1.36	0.257	6 89x10^5	1 451x10^{-6}
Al	5eV	0 190	2 94	0 924	1 49x10^6	6 71x10^{-7}
Au	5eV	1 22	1 49	0.319	7 55x10^5	1 32x10^{-6}
Cu	5eV	1 47	1 78	0.366	9 02x10^5	1 11x10^{-6}
Ta	5eV	2 58	2.20	0 416	1 11x10^6	9 01x10^{-7}
Ti	5eV	1.24	1.21	0.236	6 13x10^5	1 63x10^{-6}
W	5eV	3 40	2.85	0 505	1 44x10^6	6 94x10^{-7}

At T=57. Area = 0 08 cm^2
At 450 mJ = 2 8 J/cm^2

Structural Material	Formula	At. Wt. (g/mol)	Atomic # (Z)	Structure	Density g/cm^3	M.Point°C °C
Aluminum	Al	26 98	13	FCC	2 70	660 37
Alumina	Al_2O_3	101 96		Hex.	3.96	2072
Europium	Eu	151 96	63	BCC	5.25	822
Silica	SiO_2	60 08		Cub tetra	2 32	1723
Silver	Ag	107 86	47	FCC	10 50	961 93
Silver oxide	Ag_2O	231 74		Cubic	7 14	d230
Tantalum	Ta	180 947	73	BCC	16 6	2996
Tantalum ox	Ta_2O_5	441 89		Rhomb	8 20	1872
Yttrium	Y	88 90	39	HEX	4 47	1523
Yttrium oxide	Y_2O_3	225.81		Cubic	5 01	2410

Gases						
Helium	He	4.002	2	Hex	0.17(L)	272
Oxygen	O	15.99	8	Cubic	1.429(L)	218.4
Neon	Ne	20.17	10	FCC	0.90(L)	248.6
Argon	Ar	39.948	18	FCC	1.78(L)	189.3
Krypton	Kr	83.80	36	FCC	3.70(L)	157.2

```
SLIM Calculation Results
SLIM: Simulation of Laser Interactions with Materials
written by Rajiv Singh and John Viatella

Maximum evaporation depth: 19595 Å
Time for maximum evaporation depth: 24 ns
Maximum surface temperature: 3613 K
Time for maximum surface temperature: 5.68 ns
Laser Pulse Duration: 25 ns
Laser Pulse Density  3.8 J/cm²
```

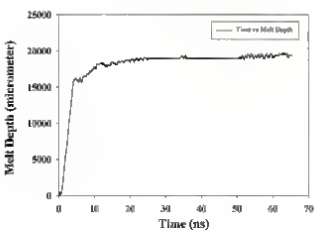

Name: Silver Symbol: Ag Group: Trans. Met. Crystal Structure: Cubic face centered
Atomic number: 47 Atomic weight: 107.868 g/mol Shells: 2,8,18,18,1 Filling orbital: 4d10
Refr. Index: 0.54
Specific Heat Capacity: C_p = 27.00 J/mol-K at 600 K or 0.235 J/g-K = 2.66 J/cm³-K
Latent Heat of Melt: 11.3 KJ/mol or 104.8 J/g = 1.115 KJ/cm³ = 2.66 J/cm³-K
Latent Heat of Vaporization: 200, 250, 300 (KJ/mol) = 19.734, 24.66, 29.600 KJ/cm³
Melt: 961.93°C = 1234 K Boil: 2162°C = 2435 K Electronegativity: 1.93 a0 = 4.077 Å
Covalent radius: 1.34 Å Atomic radius: 1.75 Å Atomic volume: 10.3 cm³/mol
First ionization potential: 7.576 V 2nd ionization potential: 21.49 V
3rd ionization potential: 34.83 V Oxidation states: 1 Density @ 293 K: 10.5 g/cm³
Specific heat: 0.235 J/gK Heat of vaporization: 250.580 kJ/mol Heat of fusion: 11.30 kJ/mol
Electrical conductivity: 0.639 10^6/cm ohm Thermal conductivity: 4.29 W/cmK
X-ray emission energy/wavelength.

	KA	KB	LA	LB	MA	MB
eV	22.105.9	24943.2	2984.41	3151.05	0	0
Å	0.56087	0.497071	4.15444	3.93473	0	0

X-ray absorption energy/wavelength

	K	L-I	L-II	L-III	M-I	M-II	M-III	M-IV	M-V
eV	25514	3806	3524	3352	0	0	0	402.2	398.1
Å	0.48595	3.25763	3.51831	3.69885	0	0	0	30.8268	31.1443

X-ray fluorescent yield

	KA	KB	LA	LB	MA	MB
	.83%	0%	.063%	0%	0%	0%

Name: Helium Symbol: He Group: Noble Gas Crystal Structure: Hexagonal Atomic number: 2
Atomic weight: 4.00260 Shells: 2 Filling orbital: 1s2 Melt: 272°C @ 26 atmos Boil: -268.6°C
Electronegativity: -- Covalent radius: 0.93 Å Atomic radius: 0.49 Å Atomic volume: ?
First ionization potential: 24.587 V 2nd ionization potential: 54.416 V
3rd ionization potential: -- Oxidation states: -- Density @ 293 K: 0.000178.7 g/cm³
Specific heat: 5.193 J/gK Heat of vaporization: 0.0845 kJ/mol Heat of fusion: ?
Electrical conductivity: -- Thermal conductivity: 0.00152 W/cmK

Name: Neon Symbol: Ne Group: Noble Gas Crystal Structure: Cubic face centered
Atomic number: 10 Atomic weight: 20.17 Shells: 2,8 Filling orbital: 2p6 Melt: -248.6°C
Boil: -246.1°C Electronegativity: -- Covalent radius: 0.71 Å Atomic radius: 0.51 Å
Atomic volume: 16.7 cm³/mol First ionization potential: 21.564 V
2nd ionization potential: 40.962 V 3rd ionization potential: 63.45 V
Oxidation states: -- Density @ 293 K: 0.0009 g/cm³ Specific heat: 0.904 J/gK
Heat of vaporization: 1.7326 kJ/mol Heat of fusion: 0.3317 kJ/mol
Electrical conductivity: -- Thermal conductivity: 0.000493 W/cmK

Name: Argon Symbol: Ar Group: Noble Gas Crystal Structure: fcc Atomic number: 18
Atomic weight: 39.948 Shells: 2, 8, 8 Filling orbital: 3p6 Melt: -189.3°C Boil: -186°C
Electronegativity: -- Covalent radius: 0.98 Å Atomic radius: 0.88 Å
Atomic volume: 28.5 cm³/mol First ionization potential: 15.759 V
2nd ionization potential: 27.629 V 3rd ionization potential: 40.74 V
Oxidation states: -- Density @ 293 K: 0.0017824 g/cm³ Specific heat: 0.528 J/gK
Heat of vaporization: 6.447 kJ/mol Heat of fusion: 1.188 kJ/mol Electrical conductivity: --
Thermal conductivity: 0.0001772 W/cmK

Name: Krypton Symbol: Kr Group: Noble Gas Crystal Structure: Cubic fcc Atomic number: 36
Atomic weight: 83.80 Shells: 2, 8, 18, 8 Filling orbital: 4p6 Melt: -157.2°C Boil: -153.4°C
Electronegativity: -- Covalent radius: 1.12 Å Atomic radius: 1.03 Å
Atomic volume: 38.9 cm³/mol First ionization potential: 13.999 V
2nd ionization potential: 24.359 V 3rd ionization potential: 36.95 V Oxidation states: --
Density @ 293 K: 0.003708 g/cm³ Specific heat: 0.248 J/gK Heat of vaporization: 9.029 kJ/mol
Heat of fusion: 1.638 kJ/mol Electrical conductivity: -- Thermal conductivity: 0.0000949 W/cmK

Name: Aluminum Symbol: Al Group: Metal Crystal Structure: Cubic face-centered
Atomic number: 13 Atomic weight: 26.98154 Shells: 2, 8, 3 Filling orbital: 3p1 Melt: 660.37°C
Boil: 2467°C Electronegativity: 1.61 Covalent radius: 1.18 Å Atomic radius: 1.82 Å
Atomic volume: 10.0 cm³/mol First ionization potential: 5.986 V
2nd ionization potential: 18.828 V 3rd ionization potential: 28.447 V Oxidation states: 3
Density @ 293 K: 2.702 g/cm³ Specific heat: 0.90 J/gK
Heat of vaporization: 293.40 kJ/mol Heat of fusion: 10.790 kJ/mol
Electrical conductivity: 0.377 10^6/cm ohm Thermal conductivity: 2.37 W/cmK

Name: Oxygen Symbol: O Group: Non-Metal Crystal Structure: Cubic Atomic number: 8
Atomic weight: 15.9994 Shells: 2, 6 Filling orbital: 2p4 Melt: -218.4°C Boil: -183.0°C
Electronegativity: 3.44 Covalent radius: 0.73 Å Atomic radius: 0.65 Å
Atomic volume: 14.0 cm³/mol First ionization potential: 13.618 V
2nd ionization potential: 35.117 V 3rd ionization potential: 54.934 V Oxidation states: -2
Density @ 293 K: 0.001429 g/cm³ Specific heat: 0.92 J/gK Heat of vaporization: 3.4099 kJ/mol
Heat of fusion: 0.22259 kJ/mol Thermal conductivity: 0.0002674 W/cmK

Name: Silicon Symbol: Si Group: Non-Metal Crystal Structure: Cubic fcc Atomic number: 14
Atomic weight: 28.0855 Shells: 2, 8, 4 Filling orbital: 3p2 Melt: 1410°C Boil: 2355°C
Electronegativity: 1.90 Covalent radius: 1.11 Å Atomic radius: 1.46 Å
Atomic volume: 12.1 cm³/mol First ionization potential: 8.151 V
2nd ionization potential: 16.345 V 3rd ionization potential: 33.492 V Oxidation states: 4
Density @ 293 K: 2.33 g/cm³ Specific heat: 0.71 J/gK Heat of vaporization: 384.220 kJ/mol
Heat of fusion: 50.550 kJ/mol Electrical conductivity: 2.52e-12 10^6/cm ohm
Thermal conductivity: 1.48 W/cmK

Silver Thermal Conductivity

T(K)	K (W/cm-K)
1	39
2	78
3	115
4	147
5	172
6	187
7	193
8	190
9	181
10	168
15	96
20	51
30	19
40	10 5
50	7
60	5 5
70	4 97
80	4 71
90	4 60
100	4 50
150	4 32
200	4 30
250	4 29
300	4.29
350	4 27
400	4 25
500	4 19
600	4 12
800	3 96
1000	3 79
1200	3 61

REFERENCE LIST

Arc64 E Archbold, D W Harper, T F Hughes Brit. J. Appl. Phys. 15, pp 1321 (1964)

Ata98 A Ata, J M Fitz-Gerald, R K Singh Mat. Res. Soc. Symp. Proc. 501, pp 381-385 (1998)

Bre91 F D Brewer, J J Zinck, G L Oleon, Mat. Res. Soc. Symp. Proc. 201 pp 543-556 (1991)

Cha93 C Champeaux, D Damiani, J Aubreton, A Catherinot, Appl. Surf. Sci. 69, pp 169-173 (1993)

Chr94 D B Chrisey, G K Hubler, Pulsed Laser Deposition of Thin Films, pp 115-355 (John Wiley & Sons, 1994) v 1

Dah71 B Dahneke, J. of Colloid and Interface Sci. 37, pp 342-353 (1971)

Dye88 P E Dyer, J Sidhu, J. Appl. Phys. 64, pp 4657-4663 (1988)

Dye93 P E Dyer D M Karnakis, Appl. Phys. Lett. 64, pp 1344 1346 (1993)

Fit98a J Fitz -Gerald, T Trottier, R K Singh, P H Holloway, Appl. Phys. Lett. 72, pp 1838-1839 (1998)

Fit98b J M Fitz-Gerald, R K Singh, Mat. Res. Soc. Proc. 501, pp 363-368 (1998)

Fur81 N Furstenau, F Hillenkamp, Int. J. Mass Spectr. Ion Phys. 37, pp 135 (1981)

Geo91 D B Geohegan, Mat. Res. Soc. Symp. Proc. 201, pp 557-562 (1991)

Geo92 D B Geohegan Thin Solid Films 220, pp 138 145 (1992)

Geo93 D B Geohegan, Appl. Phys. Lett. 62 pp 1463-1465 (1993)

Gao98 D B Geohegan A A Puretzky G Duscher S J Pennycook Appl. Phys. Lett., (in press) (1998)

Gur66 A V Gurevich, L V Pariiskaya, L P Pitaevskii, Sov. Phys. JETP 22, pp 499 (1966)

Joh71 K L Johnson, K Kendall, A D. Roberts, Proc. R. Soc. 324, pp 301-313 (1971)

Joh89 A W Johnson, T W Sigmon, G L Loper, Mat. Res. Soc. Symp. Proc. 128, pp 234 (1989)

Kaa89a A Kaauya, Y Niahina Physik D 12, pp 493 (1989)

Kaa89b A Kaauya, Y Niahina, Mat. Res. Soc. Symp. Proc. 128 pp 134 (1989)

Kaa90 A Kaauya, Y. Niahina, High Temperature Science 27 pp 473-482 (1990)

Kea95 B H aar, P N Strutt, Kona 13, pp 46-55 (1995)

Koy92 T Koyama, S Ohtsuka, H Nagata, S Tanaka, J. of Cryst. Growth 117, pp 156-160 (1992)

Kru67 H Krupp, J. of Advan. Colloid Interface Sci. 1, pp 111-239 (1967)

Kum98 D Kumar, J Fitz-Gerald, R K Singh, Appl.Phys. Lett. 72, pp 1451-1453 (1998)

Ler91 L Lerot, F Legrand, P D Bruycker, J. of Mat. Sci. 26, pp 2353-2358 (1991)

Lid95 D R Lide, Handbook of Chemistry and Physics 76 F R Frederikse Eds., pp 1155-1260 (Chemical Rubber Publishing Company) (1995)

Low96 D H Lowndes, D B Geohegan, A A Puretzky, D P Norton, C M Rouleau, Science 273, pp 898-902 (1996)

Mai60 T H Maiman, Nature 187, pp 493-494 (1960)

Mul95 E Muller, C Oesterreich, U Popp, G Michel, G Staupendahl, K Henneberg, Kona 13, pp 79-88 (1995)

Oka93 A Okano, A Y Matsuura, K Mattori N Itoh, J Singh, J. Appl. Phys. 73, pp 3158-3162 (1993)

Oti89 C E Otis, Appl. Phys. B 48, pp 455-461 (1989)

Pat64 C K N Patel, R A McFarland, W L Faust, Physiol Rev. ABCD 13, pp 617-619 (1964)

Poa82 J M Poate, J W Mayer, Eds , Laser Annealing of Semiconductors pp 1-185 (Academic, New York, 1982)

Raj98 K Rajan, P Sajgalik, R K Singh, D Kumar, J Fitz-Gerald, Mat. Res. Soc. Symp. Proc. 501, pp 313-319 (1998)

Rot84 J E Rothenberg, R Kelly, Nuclear Instruments and Methods in Physics Research B1, pp 291-300 (1984)

Sam88 M W Saamatt, in Industrial CO2 Laser, pp 1-7 (1988)

Sch90 P K Schenck, D W Bonnel, J W Hastie, High Temperature Science 27, pp 483-501 (1990)

Sch95 J P Schaffer, A Saxena, S D Antolovich, T H Sanders, S B Warner, The Science and Engineering of Materials, pp 301-364 (Irwin 1995)

Ser94 A A Seraphin, R Werwa, L A Chiu, K D Kolenbrander, Mat. Res. Soc. Symp. Proc. 318, pp 433-438 (1994)

Sin88 R K Singh J Narayan, Materials Science and Engineering B3, pp 217-230 (1988)

Sin91a R K Singh, D Bhattacharya, J Narayan, Mat. Res. Soc. Symp. 201, pp 427-432 (1991)

Sin91b R K Singh, R Neifeld, J Narayan, Mat. Res. Soc. Symp. Proc. 201, pp 501 506 (1991)

Sin94 R K Singh, J. of Non-Cryst. Solids 3, pp 1-11 (1994)

Wan95 C M Wang, K L ZHE, J. of Mat. Sci. Lett. 14, pp 129-131 (1995)

Yos96 T Yoshida, S Takeyama, Y Yamada, K Mutoh Appl. Phys. Lett. 68, pp 1772-1774 (1996)

Zhe92 A Zherikhin, V Bagratashvili, V Burimov, E Sobol, G Shubnii, A Sviridov, Physica C 198, pp 341-348 (1992)

BIOGRAPHICAL SKETCH

James Michael Fitz-Gerald was born on April 9, 1970, in Needham, Massachusetts. He spent most of his childhood years growing up in the small town of Middleborough, Massachusetts. He graduated from Bristol Plymouth Regional Technical Vocational High School in 1988. In fall of 1990 he enrolled at the University of Massachusetts at Lowell and completed his Bachelor of Science in mechanical engineering in the spring of 1993. In the fall of 1994 he entered the graduate program at the University of Florida and completed his Master of Science degree in materials science and engineering in the spring of 1995. He then continued on at the University of Florida for the degree of Doctor of Philosophy in materials science and engineering with specializations in electronic materials and particle science.

I certify that I have read this study and that in my opinion it conforms to acceptable standards of scholarly presentation and is fully adequate, in scope and quality, as a dissertation for the degree of Doctor of Philosophy

Rajiv K Singh, Chair
Professor of Materials
Science and Engineering

I certify that I have read this study and that in my opinion it conforms to acceptable standards of scholarly presentation and is fully adequate, in scope and quality, as a dissertation for the degree of Doctor of Philosophy

Robert T. DeHoff
Professor of Materials
Science and Engineering

I certify that I have read this study and that in my opinion it conforms to acceptable standards of scholarly presentation and is fully adequate, in scope and quality, as a dissertation for the degree of Doctor of Philosophy

Brij M Moudgil
Professor of Materials
Science and Engineering

I certify that I have read this study and that in my opinion it conforms to acceptable standards of scholarly presentation and is fully adequate, in scope and quality, as a dissertation for the degree of Doctor of Philosophy

Joseph H Simmons
Professor of Materials
Science and Engineering

I certify that I have read this study and that in my opinion it conforms to acceptable standards of scholarly presentation and is fully adequate, in scope and quality, as a dissertation for the degree of Doctor of Philosophy

Fred Sharifi
Assistant Professor of Physics

This dissertation was submitted to the Graduate Faculty of the College of Engineering and to the Graduate School and was accepted as partial fulfillment of the requirements for the degree of Doctor of Philosophy

August 1998

Winfred M Phillips
Dean, College of Engineering

Karen A Holbrook
Dean, Graduate School